UNIVERSITY OF OKLAHOMA

GRADUATE COLLEGE

A NEW RESEARCH METHOD TO EVALUATE THE IMPACT OF WET RADOMES ON DUAL-POLARIZED WEATHER RADARS AND COMMUNICATION SYSTEMS

A DISSERTATION

SUBMITTED TO THE GRADUATE FACULTY

in partial fulfillment of the requirements for the

Degree of

DOCTOR OF PHILOSOPHY

By

ALESSIO MANCINI
Norman, Oklahoma
2018

A NEW RESEARCH METHOD TO EVALUATE THE IMPACT OF WET RADOMES ON DUAL-POLARIZED WEATHER RADARS AND COMMUNICATION SYSTEMS

A DISSERTATION APPROVED FOR THE
SCHOOL OF ELECTRICAL AND COMPUTER ENGINEERING

BY

Dr. Jorge L. Salazar-Cerrenõ, Chair

Dr. Tian-You Yu

Dr. Hjalti Sigmarsson

Dr. Yan Zhang

Dr. Yang Hong

Acknowledgments

I would like to thank my advisor, Dr. Jorge Salazar-Cerreño for his excellent mentoring, guidance and constant support. I appreciate the time and effort he dedicated to ensure my academic, professional, and personal success. Special thanks to Dr. Robert Palmer for being an amazing director of the Advanced Radar Research Center. Thanks to Dr. Boon-Leng Cheong with whom I partially worked during this project, for providing insightful comments on my research. I would also like to thank Dr. Tian-You Yu, Dr. Hjalti Sigmarsson, Dr. Yan Zhang, and Dr. Yang Hong for making their time and effort available to become a member of the Ph.D. committee. Thanks to Dr. Nafati Aboserwal and Dr. Zeeshan Qamar for technical consulting. A special thank to Dr. Guifu Zhang for lending the disdrometer and to Dr. Petar Bukovcic for providing me the rain rate measurements. Additional thanks to my fellows José Díaz, Javier Ortiz, Rodrigo Lebrón, Arturo Umeyama, and Alex Stringer. And last but not least, I am forever grateful to my family, especially my parents, for always encouraging me to take the next step, and for enabling me to continue my graduate education abroad.

This work was supported by Dr. Salazar's fundings and partially by the Spectrum Efficient Surveillance Radar (SENSR).

Table of Contents

List Of Tables

List Of Figures

Abstract

The purpose of this dissertation is to provide a detailed study of the effect of water accumulated on wet radomes. To accomplish this goal, a novel method to evaluate the impact of wet radomes on dual-polarized weather radar systems in real-time is developed at the Advanced Radar Research Center (ARRC) of the University of Oklahoma. This technique consists of measuring in real-time, in the same direction as the radar is scanning, the level of attenuation introduced by the water accumulated on the radome. The proposed method is based on the measurement of the reflectance at the air-radome interface, and through post-processing the attenuation can be estimated. This technique can be used as a potential solution for future radar calibration methods.

A second approach to characterize radomes, consists of measuring the radiation pattern of an 8 x 2 phased array radar antenna considering various water formations positioned on the internal radome of the antenna. This method allows to account for sidelobe level and cross-polarization increase, and also to estimate the attenuation occurring on the mean beam.

Chapter 1

Introduction

1.1 Motivation

The radome is an essential component to protect the radar hardware from hydrometeors. In fact, it minimizes the wind load, reduces the need for a heavy and expensive pedestal, provides consistent nominal temperatures that facilitate the operation and maintenance, and improves the life cycle of the system (Walton 1970). To avoid degradation of the radar signal, the radome must be electromagnetically transparent. Electromagnetic transparency consists of generating low reflections, low transmission loss, and minimum distortion of polarization-dependent antenna patterns of the radio signal. One adverse effect of the radome, is the unavoidable degradation of the electromagnetic performance when the storm reaches the radar location. When it rains at the radar location, water accumulated on the radome surface can significantly affect the radar signal. Mitigation of the adverse effect of the wet radome can be accomplished by introducing a hydrophobic or superhydrophobic material to the external radome skin. This allows to minimize the impact of a continuous water film on the surface, and therefore, significantly improve the radar performance. However, agents such as pollution and time degradation both deteriorate the hydrophobic property of the radome skin, and can decrease

the radome performance in the presence of water. It is important to account for different water formations when characterizing a radome. In fact, water does not always distribute as a film (Blevis 1965), but also as droplets and rivulets. Depending on the frequency of operation of the radar, rain intensity, wind condition, shape of the radome, and composing material of the raincoat, a wet radome can significantly attenuate, reflect, and depolarize the signal. Reflections generated by the wet radome can significantly increase the cross-polarization and sidelobe level (SLL) introducing errors in the radar measurements. For frequencies below S-band, the impact of wet radomes is relatively small and is not critical for radar operations. However, for higher frequencies, water formation on the radome surface can significantly deteriorate the transmitted and received signals that can lead to a large bias in weather radar measurements. With the introduction of dual-polarized systems in operational weather radar networks, target accuracy of 0.1 dB for the differential reflectivity (Z_{DR}) is required (Zrnic and Doviak 2005; Wang and Chandrasekar 2006; Golbon-Haghighi et al. 2016; Golbon-Haghighi, Saeidi-Manesh, Zhang and Xhang 2018; Golbon-Haghighi, Zhang and Doviak 2018). To achieve this goal, all sources of bias must be taken into account, with one of the most important sources of bias being the radome. The problem of polarimetric calibration was discussed in Mirkovic and Zrnic (2018*a*); Fulton et al. (2018); Mirkovic and Zrnic (2018*b*).

1.2 Literature Review

Despite the numerous publications available for wet radome characterization at frequencies higher than S-band, the literature related to this topic for S-band is limited. Some quantitative analysis in S-band is presented in Wilson (1978); Effenberg et al. (1986); Joy and Wilson (1986); Merceret and Ward (2002). Effenberg et al. (1986) and Joy and Wilson (1986) showed experimentally that when water distributes as a laminar flow, attenuation up to 3 dB can be obtained for rain rate of 50 mm h^{-1}. Merceret and Ward (2002) demonstrated that when the rain rate reaches 200 mm h^{-1}, the attenuation can reach up to 5.6 dB and 2 dB for film and droplet formations, respectively. No other study about the radome impact on the radar performance is available in S-band. Therefore, the importance of this dissertation is that it provides additional knowledge on the impact of an S-band wet radome on the radar performance.

The effect of wet radomes in C-band was investigated by Kurri and Huuskonen (2008); Frech (2009); Frech et al. (2013); Manz et al. (1999). Kurri and Huuskonen (2008) measured a 3-dB two-way attenuation when water on the radome forms as a continuous film on a dirty radome for a rain rate of 15.1 mm h^{-1}. In contrast to film formation, a 1.5-dB two-way loss was measured when the radome was waxed (droplets formation), for a 22.1 mm h^{-1}-rain rate. Frech et al. (2013) performed experiments showing that a wet radome can produce a bias above +0.8 dB for the Z_{DR} for 9 mm h^{-1} of rain. Experiments conducted by Manz et al. (1999) on a dirty radome (film formation), measured an attenuation of 2 dB for 40 mm h^{-1}-rain

rate. Additional experiments were performed by Manz et al. (1999) at 300 mm h^{-1} and 350 mm h^{-1} rain rates. Manz et al. (1999) found that attenuation of 4.9 dB and 5.4 dB was measured at 300 mm h^{-1} and 350 mm h^{-1} rain rates, respectively. However, an important result achieved by Manz et al. (1999) was that at heavy rain rates the water repellent effect fails to avoid a closed film formation. Thompson and Illingworth (2012) presented a technique to measure the total attenuation from the radome, showing that old radomes can produce 2 - 3 dB of transmission loss when the rain rate is only 2 - 3 mm h^{-1}.

Extensive literature is available about radome attenuation in X-band. Bechini et al. (2010) proposed a technique to measure the attenuation under wet conditions for weather radars. Bechini's method is based on the disdrometer measurements, and it assumes that water is a film, and did not account for rivulet effects that could produce various levels of attenuation in the H- and V-polarizations. Gorgucci et al. (2012) developed two methods for Z_{DR} calibration, sun and weather target calibrations. Both of the techniques proposed by Gorgucci were validated through experiments. Another study on the effect of wet X-band radomes on radar performance was done by Schneebeli et al. (2012). Schneebeli employed a self-consistent algorithm to estimate the reflectivity offset introduced by the presence of the radome. Using the extended Kalman filter (EKF) algorithm and a standard rain attenuation correction scheme (ZPHI), Schneebeli corrected the radar measurement for both attenuation and differential attenuation. An alternative method was implemented by Frasier et al. (2013) which used two radars to look at the same volume target. By noticing an increase of reflectivity occurring in only one of the radars, the attenuation due

to the wetting of the related radome is deduced. The technique proposed by Frasier allows to achieve absolute calibration of the radar. A possible limitation of using two radars is that the different scan patterns produce a temporal mismatch that results in additional scatter. Furthermore, two radars are not always available to look at the same volume target. An analytical model to estimate the performance of the wet radome, for dual-polarized radars operating in X-band, was proposed by Salazar et al. (2014). Salazar's approach found good agreement with experimental data from the Weather Surveillance Radar-1988 (WSR-88D) and the Collaborative Adaptive Sensing of the Atmosphere (CASA) radar. Díaz et al. (2014) investigated the attenuation of wet X-band radomes for various hydrophobic surfaces as function of the rain rate. The model created by Díaz was validated through experimental results.

The attenuation of radio signals on satellite systems due to water accumulation on the radome is extensively analyzed in the literature. Anderson (Anderson 1975) studied the effect of rain on the transmission through large radomes at 20 GHz. Results in Anderson (1975) stated that 12 dB-attenuation was produced at a rain rate of 140 mm h^{-1} for water film formation. A theoretical approach was considered by Chang (1985). Chang's model employed the ray-tracing technique to characterize the wet radome attenuation in the frequency range from 12 to 16 GHz. The model found good agreement with the measurements performed using two different types of radomes: ESSCOLAM 6 (hydrophilic) and ESSCOLAM 8 (hydrophobic). ESSCOLAM 8 provided better performance than ESSCOLAM 6, because in the

first case water accumulated as droplets, while in the second scenario water distributed as a continuous film. The measured attenuation for the hydrophobic and hydrophilic radomes were 2 dB and 7 dB at 14 GHz. Therefore, the study presented in Chang (1985) highlighted how important it is to take into account the water formation when the radome performance is tested. Hendrix et al. (1989) evaluated the effect of transmission loss for wet radomes at 20 GHz, at various angles of incidence. Hendrix noticed that the radar signal can be attenuated up to 2 dB. Fenn (1997) performed measurements of the attenuation of radomes at 20 GHz. First, Fenn found that a dry radome at such a frequency can generate an attenuation up to 0.7 dB. The experiments performed with artificial rain in Fenn (1997) measured attenuation of 1 dB, 1.1 dB, and 1.3 dB for rain rates equal to 5 mm h^{-1}, 10 mm h^{-1}, and 50 mm h^{-1}, respectively. Cohen and Smolski (1966) and Crane (2002) analyzed the effects of water on the electromagnetic signal at 20 GHz. Crane (2002) found 4-dB attenuation at the rain rate of 40 mm h^{-1}.

All the above studies highlight how important it is to account for the radome impact when characterizing the radar performance. The influence of water on the radome can then be classified by the frequency of operation of the radar, the type of water formation on the raincoat, and the radome geometry. Effects generated by frost and ice storms should be also investigated. A layer of ice formed on the radome surface would produce additional attenuation to the radar signal. However, the ice effect was not analyzed in this dissertation for lack of weather events, but it still remains an important factor to investigate. If the attenuation of a wet radome can be measured or at least estimated, it would be possible then to calibrate this effect

Table 1.1: A summary of the most relevant literature including, when available, the frequency of the radar operation, type of approach chosen, the observed water formation, rain rate (R), and transmission loss (TL).

Reference	**Freq. (GHz)**	**Approach**	**Water**	R **(mm h^{-1})**	TL **(dB)**
Wilson (1978)	S-band	Exp.	N/A	< 90	< 1
Effenberg et al. (1986)	S-band	Exp.	Droplets	15	0.5
			Film	10-50	1.5-3
Merceret (2002)	S-band	Empirical	Droplets	1-200	0.01-1.95
			Film		0.03-5.6
Kurri (2008)	5.65	Analytical	Film	5	1.25
Manz et al. (1999)	C-band	Exp.	Droplets	40	2
			Film	300-350	4.9-5.4
Trabal (2010)	9.375	Exp.	N/A	5	0.6
Bechini et al. (2010)	9.375	Empirical	Film	4	2.3
				5	2.5
				6.6	2.8
Frasier et al. (2013)	9.4	Exp.	N/A	4	1.8
				5	2
				6.6	2.2
Salazar et al. (2014)	10	Analytical	Droplets	5	0.15
				10	0.2
			Film	1	0.8
				10	1.8
Ruze (1965)	15.5	Analytical	Film	2.8	3.2
Blevis (1965)	3.65	Analytical	Film	N/A	5.6
	16				12.3
Fenn (1997)	19.5	Exp.	N/A	6	1
Anderson (1975)	20	Exp.	Film	140	12
Hendrix et al. (1989)	20	Exp.	Droplets	N/A	1.8
			Rivulets	N/A	2
			Film	N/A	5.8

and therefore, improve the radar measurement quality. A summary of the literature previously discussed is listed in Table 1.1.

1.3 Statement of Work

As discussed in the previous section, the radome problem is not new. However, the literature cited in this work performed studies in laboratory conditions and none of them presents a potential solution for real-time assessment of the radome accounting for the various water formations occurring on the radome. This dissertation presents a novel research method for the radio-frequency (RF) characterization of radomes in both wet and dry conditions in real-time. Specifically, this work includes an algorithm to estimate the amount of water accumulated on the radome as a function of the rain rate, taking into account the geometry and dimensions of the radome, as well as the hydrophobic properties of the radome outer skin.

In addition, a numerical study in S-band to evaluate the effect of the radome placed at various distances from a 3 x 3 microstrip antenna array is performed. This analysis suggests that there can be a optimum distance that minimizes the impact of a wet radome on the antenna performance.

As last study, a second novel approach is presented and discussed. This method is based on the near-field measurements of the radiation pattern of a microstrip phase array antenna considering different water formations on the internal radome of the array. This investigation is important because it allows to quantify the effect of

various water formations on the SLL, cross-polarization component, and attenuation of the main beam.

The work discussed in this dissertation is focused on characterizing the performance of wet radomes providing theoretical and numerical analysis that are compared to experimental results. Because weather radars typically operate at S-, C-, and X-band, this dissertation is focused on the radome effects at those frequency bands.

1.3.1 Dissertation Overview

The work performed in this dissertation is divided as follow. Chapter 2 provides the theoretical background about radomes. This includes some design choices of radomes such as wall configurations, types and geometries, as well as electromagnetic characteristics. Environmental considerations about the radome operation are also presented. In addition, Chapter 2 discusses the problem of how close the radome should be placed to the antenna. Numerical simulations show how important is the location of the radome with respect to the antenna when water is accumulated on the radome. Chapter 3 presents the design and modeling of radomes operating in S-, C-, and X-bands. Chapter 4 performs analysis of wet radomes. This includes complete models to characterize the dielectric properties of water as a function of frequency and temperature, to compute amount of water accumulated on the radome based on the geometry and shape of the radome. In Chapter 5, the proposed radome characterization techniques are introduced and discussed in detail. First, the classic two-probe method is presented, then the proposed one-probe technique is explained.

Chapter 6 discusses the results obtained by employing the one-probe technique and by measurements performed using a near-field chamber to characterize the effect of various water formations accumulated on a 8 x 2 phase array antenna. Finally, Chapter 7 summarizes the work proposed in this dissertation and highlights the most important results found, and it also discusses the future works.

Chapter 2

Theoretical Background

This chapter discusses the basic information about radomes. This includes the criteria to design the radome, the stackup, geometry, and the electromagnetic performance of a radome in dry conditions. The radome performance is characterized in dry condition by first using an analytical approach (transmission line model), and using numerical analysis with ANSYS High Frequency Structure Simulator (HFSS 2017) software. It will be shown that the two methods are in good agreement.

2.1 Radome Fundamentals

The radome is an enclosure that protects the radar hardware from environmental agents such as rain, hail, frost, dust, etc. A radome is designed to be electromagnetically transparent to the radar signal. Ideally, the performance of the radar antenna should not be affected by the presence of the radome. However, this is not physically possible, because reflection and attenuation occur at the air-radome interface. It is important, to design the radome in order to minimize its impact on the radar performance. As it will be shown, a radome in dry conditions does not critically affect the radar operations, but when rain reaches the radar location, the presence of water accumulated on the outer surface of the radome negatively affects the performance of the radar signal. The effect of water will be shown in Chapter 4. The research

presented in this dissertation is focused on ground-based radars, but its validity can be extended to other types of radars.

2.1.1 Radome Wall Configurations

The types of wall configurations described in this section are categorized based on the materials that compose the radome. The structure composing the radome walls is made in order to address the design requirements (Burks 2007), such as mechanical and electrical. Based on the dimensions of the radome, electrical requirements, and frequency of operation of the radar, various radome stackups are available. Each of them has advantages and limitations. In short, the radome is composed by either a single material or a combination of various materials (multilayer). The single material radome is also called monolithic wall, while the multilayer radome is normally known as a sandwich configuration. The two types of wall configurations are described below and they are schematically shown in Fig. 2.1.

2.1.1.1 Single Material

The monolithic wall consists of a single material with a homogeneous dielectric constant. The thickness of this radome configuration can vary from being electrically very thin to an integer multiple of a half-wavelength. The electrical thickness also provides adequate strength and rigidity. The disadvantage of this type of radome is that since the thickness also provides the necessary mechanical strength for the radome, it is not suitable for large radomes. More information about the monolithic wall configuration can be found in Burks (2007).

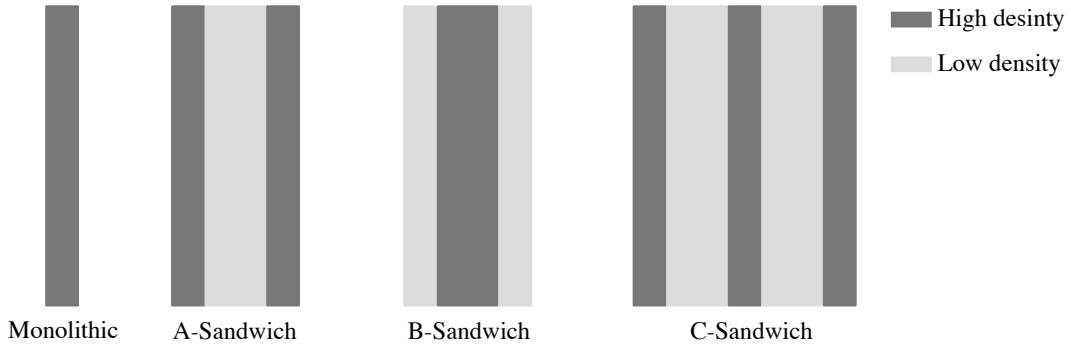

Figure 2.1: Radome wall configurations.

2.1.1.2 Multilayer

Multilayer or sandwich radomes, are necessary for applications where a single layer radome does not meet the design requirements. Multilayer radomes provide higher structural strength and larger bandwidth. The multilayer topology is divided in A-sandwich, B-sandwich, and C-sandwich (Fig. 2.1).

The A-sandwich type of radome (Fig. 2.1) consists of three layers: two outer layers named skin, and a inner layer called core. The skin has the purpose to provide mechanical strength to the radome and it is characterized by high dielectric constant. The skin layers are chosen to be very thin in order to minimize the losses and the reflections in the radar signal. The core has a low dielectric constant and it is normally made of foam or honeycomb. For the A-sandwich, the thickness of the core is chosen so that the wave reflected from the outer skin cancels out with the wave reflected from the inner layer of skin at the desired frequency of operation and incidence angle (Burks 2007).

The B-sandwich configuration (Fig. 2.1) is a reversed version of the A-type. It has a high-density core and two low density skins. This type of radome provides

wide bandwidth at high incidence angles, but it has low structural strength because the low-density skins employed (Burks 2007).

The C-sandwich type of radome (Fig. 2.1) is made of five layers and it can be pictured as two A-sandwich radomes merged together. The extra layers are used to provide additional mechanical strength and also give more degrees of freedom in the electrical design (Burks 2007).

In general, multilayer radomes can contain as many number of dielectric layers as needed to match the mechanical rigidity and the environmental conditions, as well as obtain larger bandwidth or multibands.

2.1.1.3 Core Configurations

This section provides information about the core selection for a radome. The existing configurations for the core materials are either solid or honeycomb.

The solid configuration for the core is normally accomplished by using foam. It is more expensive than honeycomb and it does not allow the design with particular shapes, such as conical. The sharp transition at the peak of the cone cannot be realized with this configuration. The advantage of using a solid core includes uniform attenuation on both H- and V-polarizations. Therefore, the level of depolarization is low. Solid core configuration is employed to realize radomes for the WSR-88D radars, which is shown in Fig. 2.2. Fig. 2.2a presents a schematic representation of the multilayer radome using a solid core. Fig. 2.2b shows a photograph taken to a sample of the WSR-88D radome stackup.

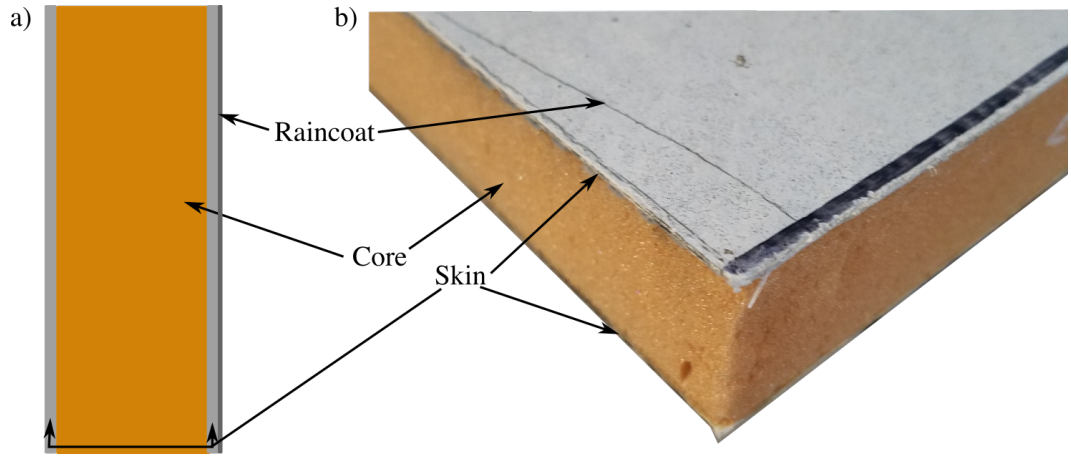

Figure 2.2: An example of solid core (foam). The radome shown is employed for the WSR-88D Table 3.1. a) A draw of the radome cross-section. b) A photograph of a sample panel.

The honeycomb configuration is a lower cost solution that can replace the solid core whereas conformal shapes of radomes are required, such as conical. Honeycomb allows easier manufacturing because their microcells composition and air filling. This makes honeycomb easy to bend. The relevant drawback of using honeycomb is that it is not isotropic. Fields coming from incidence angles, different than the normal, are subject to various attenuation. This happens because the geometry of the honeycomb is different at various projection angles. It does not occur when the foam is employed, because the core is solid and geometrically uniform. As a consequence, honeycomb is likely to suffer higher levels of depolarization than the solid core. A draw of the cross-section and a photograph of the radome using honeycomb, is shown in Fig. 2.3.

A comparison between two A-sandwich radomes that use different types of core concludes the discussion of this section. One of them employs honeycomb, and it is named H-radome for convenience, while the other radome has the core made of

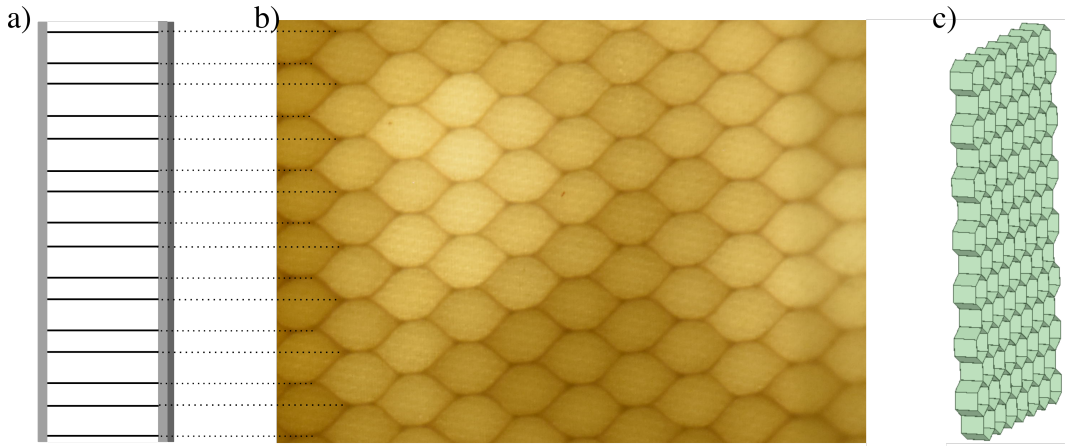

Figure 2.3: An example of honeycomb structure. a) A schematic representation of the A-sandwich. b) A close look of the radome taken from the inside. The radome shown is employed for the PX-1000 weather radar Table 3.3. c) A graphical representation of the honeycomb in a trimetric view.

foam, and is called F-radome. The stackup of the H-radome is listed in Table 2.1, while the materials used for F-radome are included in Table 2.2. Both radomes are designed to operate in X-band (9.6 GHz) and they have the same materials and thicknesses for the raincoat and skin layers. The H-radome uses honeycomb with a dielectric constant of 4.4, such a value is not the equivalent dielectric constant of the core, but it corresponds to the material employed to realize the honeycomb structure. This type of core is filled with air, and since the fraction of volume occupied by the honeycomb is small, the equivalent dielectric constant of the core is lower than 4.4. To realize the F-radome, honeycomb was replaced with Nomex material (foam), which has a dielectric constant of only 1.1. Nomex completely fills the core layer without leaving any air gaps. To note that the tangent loss of Nomex is higher than the configuration using honeycomb. Therefore, higher absorption is expected for the F-radome. To obtain resonance at 9.6 GHz, the core thickness of the F-radome was optimized (Table 2.2).

Table 2.1: H-radome stackup.

Material	**Thickness (mm)**	ϵ_r	**tan** δ
Raincoat	0.0762	3.65	0.0365
GlassEpoxy	0.56	4.25	0.017
Honeycomb	6.35	4.4	0.001
GlassEpoxy	0.56	4.25	0.017

Table 2.2: F-radome stackup.

Material	**Thickness (mm)**	ϵ_r	**tan** δ
Raincoat	0.0762	3.65	0.0365
GlassEpoxy	0.56	4.25	0.017
Nomex	6.6	1.1	0.003
GlassEpoxy	0.56	4.25	0.017

The comparison between the RF performance of the H- and F-radomes are shown in Fig. 2.4. As presented in Fig. 2.4a, the reflectances of both radomes show a peak at 9.6 GHz and their behavior is very similar across the defined frequency range. However, the F-radome, presents a resonance peak that is slightly lower at 9.6 GHz, therefore, it is reasonable to think that the transmittance at that frequency will be higher (lower attenuation) than for the H-radome. It is shown in Fig. 2.4b, that it is not like that. This unexpected result is due to the absorption component that can be estimated by looking to the tangent loss of the two materials used to realize the core (Tables 2.1 and 2.2). To note that the lossy part of the core used to make the H-radome, is even lower than the one shown in Table 2.1 because that core is filled with air making the effective tangent loss even lower. Additionally, scattering due to the geometrical shape of the honeycomb can contribute to higher losses.

The reflectance and the transmittance computed as a function of steering angle are shown for H- and V-polarizations in Fig. 2.4c and 2.4d. From the figure, it can be noted that there is no difference between the reflectance computed for the

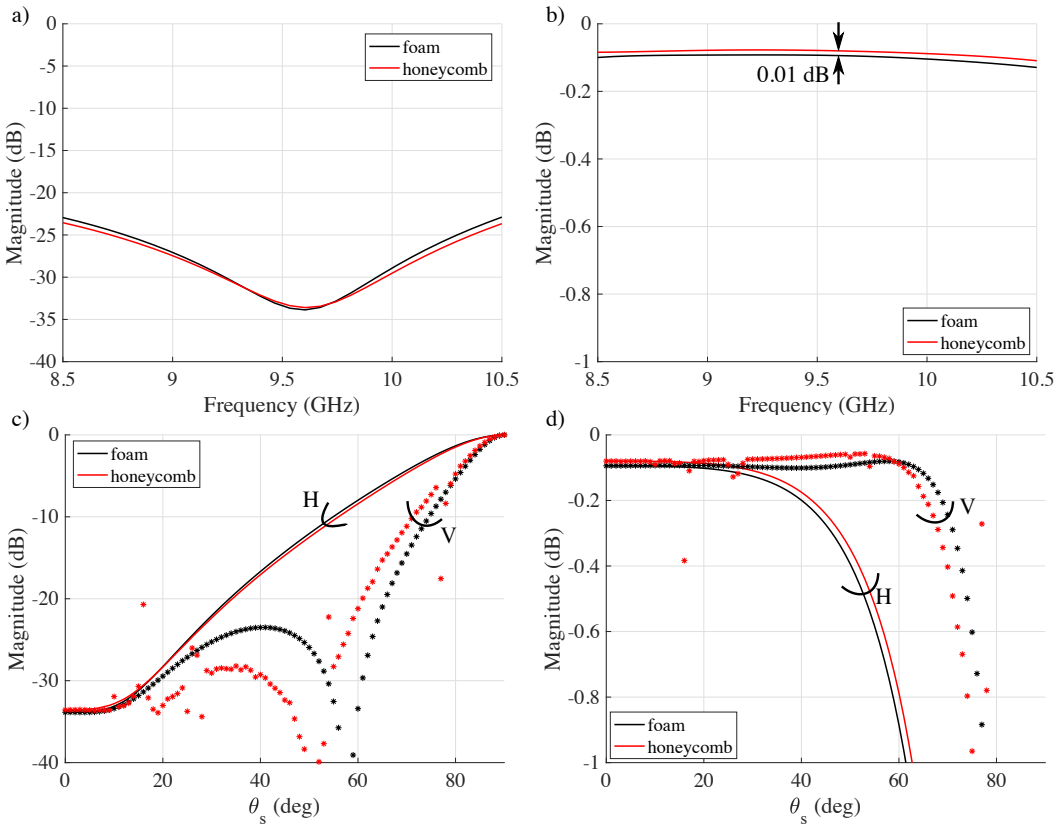

Figure 2.4: A comparison between the performance of the F- and H-radomes that have foam and honeycomb as a core, respectively. a) Reflectance as a function of the frequency. b) The transmittance as a function of the frequency. c) The reflectance as a function of the scanning angle. d) The transmittance as a function of the scanning angle.

F- and H-radomes in the H-polarization, but substantial difference occurs in the V-polarization. The vertically polarized component of the signal is more affected by the presence of the honeycomb showing oscillating peaks around 20°, 30° and 78°, while the curve generated for the foam scenario shows a more gradual behavior. In addition, the reflectance generated by the H-radome is higher at larger steering angles than the one produced by the F-radome.

Table 2.3: Ceramic radome materials. Electrical properties measured at 8.5 GHz at room temperature (Burks 2007).

Material	**Density (g cm^{-3})**	ϵ_r	**tan** δ
ALON, $9Al_2O_35AlN$	3.69	9.28	0.0003
Aluminum oxide	3.32	7.85	0.0005
Alumina, hot pressed	3.84	10.0	0.0005
Beryllium oxide	2.875	6.62	0.001
Boron nitride, hot-pressed	2.13	4.87	0.0005
Boron nitride, pyrolytic	2.14	5.12	0.0005
IRBAS	3.25	7.75	0.0012
Magnesium aluminate (spinel)	3.57	8.26	0.0005
Magnesium aluminum silicate (cordierite)	2.44	4.75	0.002
Magnesium oxide	3.30	9.72	0.0005
Pyroceram 9606	2.60	5.58	0.0008
Silicon dioxide	2.20	3.82	0.0005
Silica-fiber composite (AS-3DX)	1.63	2.90	0.004
Slip-cast fused silica	1.93	3.33	0.001
silicon nitride	2.45	5.50	0.003

2.1.1.4 Radome Materials

The list in Table 2.3, includes materials that can be employed either for monolithic radomes or for skins. Two main categories of materials exists: the first one is ceramics, and the second one is organic and composites. The choice of the materials depends on the electrical, structural, and thermal performance that the radome must achieve (Burks 2007).

1. **Ceramics**

   Ceramics materials are normally employed for applications where high temperatures occurs, such as missiles. A list of the most used ceramic materials is summarized in Table 2.3 (Burks 2007).

2. **Organic and Composites**

Table 2.4: Thermoplastic radome materials. Electrical properties measured at 8.5 GHz at room temperature (Burks 2007).

Material	ϵ_r	**tan** δ
Lexan	2.86	0.006
Teflon	2.10	0.0005
Noryl	2.58	0.005
Kydox	3.44	0.008

Table 2.5: Composite radome materials. Electrical properties measured at 8.5 GHz at room temperature (Burks 2007).

Material	ϵ_r	**tan** δ
Expoxy-E glass cloth	4.40	0.016
Polyester-E glass cloth	4.10	0.015
Polyester-quartz cloth	3.70	0.007
Polybutadiene	3.83	0.015
Fiberglass-polybenzimidazole	4.90	0.008
Quartz-reinforced bismaleimide	3.30	0.004
Quartz-reinforced cyanate-ester	3.30	0.005
Quartz-reinforced polyimide	3.20	0.008
Duroid 5650 (loaded Teflon)	2.65	0.003

Many thermoplastic and thermoset materials are suitable for radome use. Structural properties of resin systems can be enhanced by combination with a reinforcement material to create a composite. Thermoplastic materials are limited to applications involving modest temperatures (Burks 2007). Polyimide resins can withstand temperatures near 750° F. Thermoplastic materials are listed in Table 2.4, while composites materials are summarized in Table 2.5.

2.1.2 Types of Radomes

The radome subdivisions described in this section are based on the rigidity, which depends on the dimensions of the radome to design. Two types of radomes exist: air supported, which consists of an airtight fabric envelope supported entirely by

Figure 2.5: The S-band OU-PRIME space-frame radome. The radome stackup is A-sandwich type. Photo source: https://en.wikipedia.org/wiki/OU-PRIME.

a small amount of internal air pressure, and rigid, which are shell structures that maintain their shape because of the strength of the materials employed (Vitale 1985). Because the experiments discussed in Chapter 5 were performed on rigid radomes, the following discussion is focused on rigid radomes.

Various types of rigid radomes (Vitale 1985) are available. The choice of which one of these to employ depends on various requirements, such as: electrical characteristics, environment considerations, and cost. The discussion of rigid radomes starts with the definition of the space-frame type.

The space-frame radome is suitable when physical strength is required. It is composed of a framework that guarantees the structural integrity with dielectric windows assembled on it. Because the rigidity of the radome is provided by the framework, the windows are not required to carry any load and hence they can be really thin. The framework is usually made of metal and therefore, it is necessary to account for losses during the design. Normally, the losses due to blockage are accounted by considering the percentage of the overlapping area between the framework and the radiating aperture. The overlapping area is usually very small and it can be neglected. By randomizing the scattering points due to the metallic framework, minimization of the losses for blockage is achieved. The space-frame radome is normally fabricated as a sphere subdivision. This makes it easy to fabricate, transport, and assemble. Therefore, it is cheaper than other rigid radomes. In Fig. 2.5, an example of space-frame radome is presented.

The second type of rigid radome is thin skin laminate. It does no employ any framework, therefore, the loads and stresses are carried in the shell membrane. For transportation, it is subdivided into segments with light flanges for attachment and provide continuity to the membrane loads. This type of radome is the most efficient structurally. The reflectivity of the thin skin radome is very low and attenuation is negligible. The electrical requirements do not permit a skin thickness that is also structurally satisfactory. Therefore, such a type of radome with very large diameters are not possible. In Fig. 2.6, an example of a thin skin laminate radome is shown.

A third type of rigid radome is made of foam shells. The structural strength is provided by a uniformly thick shell of foam material which allows to overcome

Figure 2.6: The X-band partial radome of the RaXPol (Pazmany et al. 2013). This radome is designed with the monolithic-wall topology which belongs to the category of thin skin. Photo source https://arrc.ou.edu/radars.html.

the size-performance limitation of the thin skin laminate technique. Because the reflectance depends uniquely on the dielectric constant of the material, the wall thickness does not affect the performance. Therefore, radomes with large diameter can be constructed.

The last type of radome discussed, is the window or partial radome. In this scenario, the radome houses only the front part of the antenna which is fixed to it. Various shapes of radome can be made with this method: partial sphere, conformal, and flat. An example of partial radome is presented in Fig. 2.6.

2.1.3 Radome Shapes

There are various radome shapes. The geometry selection is necessary in order to minimize the reflections and losses of the signal by keeping the radome orthogonal to the main beam of the radar antenna. The most common radome shapes are: flat, spherical, conical, bullet, and cylindrical.

Flat radomes are normally employed for microstrip antenna arrays because both antenna and radome have a planar geometry. Flat radomes are rigid and they can be made either with the monolithic or multilayer techniques. This choice is left to the designer in order to meet the electrical and mechanical requirements.

Spherical configuration can be either realized by air support (not rigid) or using one of the rigid techniques earlier described. An example of the spherical rigid radome with the space frame to provide the mechanical support, is shown in Figs. 2.5 and 3.1.

The conical shape belongs to the category of partial radomes and it is realized with the single layer technique. Normally the material that composes the radome is plastic. This configuration is presented in Fig. 2.6.

The bullet-shape radome is shown in Fig. 2.7. It can be either realized with a multilayer or a single material. The bottom part of the sphere is replaced with a cylinder, thus to form the geometry of a bullet. This procedure saves space in the horizontal plane and makes the radome more compact. It is commonly employed where space limitations occur. The bullet shape radome finds application for mobile radars, making the radar suitable for relocation by using common vehicles of transportation.

The cylindrical radome is employed for antennas with configurations such as dipoles or cylindrical microstrip antenna arrays. This geometry is very similar to the bullet shape radome with the only difference that the top does not terminate with a hemispherical part. A photograph of the cylindrical radome is presented in Fig. 2.8.

Figure 2.7: The X-band bullet shape radome of the X-band PX-1000 (Cheong et al. 2013). The radome stackup is A-sandwich type with honeycomb as a core. Photo source: https://onenet.net/onenets-high-speed-capabilities-support-advanced-radar-research-in-oklahoma/.

2.1.4 Electromagnetic Characteristics

The electrical design of a radome must account for the reflections of the signal generated at the wall-air interface, absorption of the signal energy occurring inside the radome, and diffraction of the signal due to discontinuities or joints present in the radome structure. Each of these factors have a relative importance based on the type of radome considered for the design.

Reflections at the radome-air interface are quantified by the reflection coefficient (or reflectance, in terms of power) and they affect the antenna radiation pattern by increasing the secondary sidelobes and the cross-polarization of the radiation pattern. The absorption contributes to increase losses (attenuation) of the radar signal. Diffraction of the signal introduces distortion in the radiation pattern of the

Figure 2.8: A photograph of the S-band cylindrical radome of the CPPAR (Fulton et al. 2017).

radar antenna by changing the phase front and shifting the main beam from its electrical axis. This shift is called "boresight error".

The transmission loss introduced by a radome, is normally quantified by measuring the antenna gain with and without the radome. For a sandwich radome, having multiple boundaries, any departure from the optimum skin spacing, core density, and adhesive thickness, will increase the level of reflections. The minimum possible thickness of the radome is normally desired to ensure low reflections and attenuation. However, increasing the radome thickness is often desired to enhance the mechanical strength of the radome. Therefore, a tradeoff is necessary. An example is reported in the following analysis. The minimum thickness is selected to be $\lambda/4$ to obtain a cancellation effect between the reflected waves at the inner and outer skin layers.

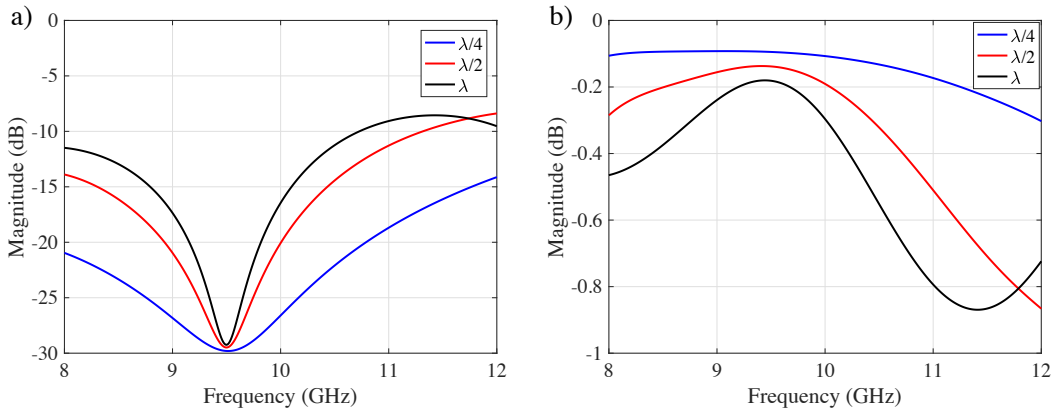

Figure 2.9: The frequency response of the reflectance (a) and transmittance (b) for various thicknesses of the core.

Table 2.6: The tradeoff between RF performance and structural strength of a radome based on the core thickness.

Thickness	**RF Performance**	**Structural Strength**
$\lambda/4$	Best	Poor
$\lambda/2$	Good	Poor
λ	Poor	Best

Multiples of $\lambda/4$ produce resonances at the same frequency. A core with thickness equal to a multiple of $\lambda/4$, can be selected to increase the structural strength of the radome, but at the expenses of the attenuation and bandwidth. A numerical analysis of an A-sandwich is presented in Fig. 2.9. In Fig. 2.9a, the resonance is shown. It can be noticed that the resonance occurs at the same frequency for all the thicknesses considered. However, for thicker cores the bandwidth is narrower and attenuation increases (Fig. 2.9b) because the attenuation increases and also because by placing the radome at $\lambda/4$ the cancellation effect discussed above does not happen anymore.

In Table 2.6, a comparison between the RF performance and the structural strength of the radome based on the core thickness is presented.

Perturbation of the phase front of the transmitted signal caused by the radome, may introduce a shift in the position of the main beam. Energy scattered asymmetrically can generate a shift of the main beam. Therefore, it is important to minimize the boresight shift by minimizing the phase disturbances to the phase front. The sharper the discontinuities or the asymmetry, the greater the rate of boresight shift.

2.1.5 Environmental Considerations

The conditions of the environment where the radar operates play an important role in the radome design. Freezing precipitation and ice, normally do not have a critical aspect during the radome design. However, wind and snow accumulation both are important for structural considerations. In particular, wind loading is the most important to account for when designing a radome. The wind loading can be controlled by choosing the proper shape of the radome, which determines the pressure distribution on the structure.

The type of precipitations also affects the radome design Vitale (1985). The precipitations discussed are: rime ice, freezing rain, and snow. Rime ice is generated when supercooled cloud or fog drops strike an object and freeze on contact, without forming a liquid film. This phenomena is typical in the Arctic regions. The intensity of rime ice depends on the drop size, liquid-water content of the clouds, wind speed, and the aerodynamic characteristics of the object. Large droplets and high amount of water in the cloud increase the severity of rime icing. An example of sculpture created by rime ice is shown in Fig. 2.10. Freezing rain is a type of precipitation maintained at temperatures below freezing by the ambient air mass that causes

Figure 2.10: An example of a rime ice sculpture peering down (website source: https://lovettneil.wordpress.com/2013/01/12/rime-ice/).

freezing on contact with surfaces. As the droplet diameter increases, so does the collection efficiency. Freezing rain with a volume-median droplet size of 0.95 mm in a rainfall rate of 0.25 mm h^{-1}, has a collection efficiency that approaches 100 %. Therefore, it is necessary to determine if this phenomena is frequent based on the geographical area of operation of the radar, and then decide if to account for it or not. Dry snow is not a problem generally, since it does not stick to cold surfaces. However, wet snow normally sticks to surfaces and because its high liquid-water content is necessary to account for its presence.

More information about environmental considerations and structural design of the radome can be found in Vitale (1985).

2.2 Distance Radome-Antenna

A radome is normally designed to enclose the radar antenna to minimize wind load and cost of fabrication. If, for example, we consider a dish reflector antenna, the corresponding spherical radome will be designed to have the smallest diameter possible. The distance between the closest part of the radar feed to the radome is only a few centimeters. The drawback of this choice is that the radome is located in the reactive near-field region of the antenna. The reactive near-field region of the radome is calculated as

$$d_{near\text{-}field} \leq 0.62\sqrt{\frac{D^3}{\lambda}} \tag{2.1}$$

where D is the maximum dimension of the antenna aperture and λ is the wavelength. D is equal to the diameter of the reflector in this case. For example, the PX-1000 has a dish reflector with a diameter of 1.22 m. The wavelength at the operating frequency of 9.55 GHz is 3.14 cm. The calculated reactive near-field distance is 4.7 m. In this scenario, the radome is located inside the reactive field of the antenna. This means that, when water accumulates on the radome, it is within the reactive near-field region of the antenna. This region increases with the dimension of the antenna (D) and hence in practical cases the radome is always located within this distance. In case of a flat radome, if it is located outside the reactive near-field region of the antenna, then its surface must be increased to contain all the incident field and to avoid diffraction from the borders. This choice would consequently increase the cost of fabrication and the size of the radome as well as the wind load. It is

reasonable to ask, if there is an optimum gap between the antenna and the radome ($d_{a\text{-}r}$) that minimizes the degradation of the radiation pattern.

A numerical study in HFSS was conducted to evaluate the effect of both a dry and wet flat radome on the radar signal as function of the radome distance from the antenna. For this purpose, the performance of a 3 x 3 array operating in S-band was analyzed under various conditions. The first case considers the presence of the radome placed at a distance radome-antenna $d_{a\text{-}r}$ from the array. The d_{a-r} was subsequently changed by moving the radome away from the antenna. To avoid diffraction generated at the border of the radome, the radome was designed to be larger than the array. This way all the incident field was confined inside the radome surface. The perfect matched layer (PML) as a boundary condition was used to perform the analysis, because it minimizes the reflections coming from the airbox. For the second case, a thin film of water of 200 μm was added on top of the radome. This water thickness corresponds to a 163 mm h^{-1}-rain rate accumulated on a square radome of dimension equal to 1 m, inclined to 60° with respect to the horizontal axis. In the last investigation, both water and radome were removed. For all the studies performed, the dimensions of the airbox were maintained the same. The distance between the airbox and the radome (d_{PML}) is equal to λ (λ = 10 cm at 3 GHz). The scenario discussed is shown in Fig. 2.11. In the second case analyzed for the wet radome, $d_{a\text{-}r}$ was changed from $\lambda/4$ to λ with step $\lambda/4$.

For the S-band 3 x 3 array, D is taken as the diagonal dimension of the array and it is equal to 21.8 cm. The calculated $d_{near\text{-}field}$ is 19.96 cm. Therefore, in all cases analyzed, $d_{a\text{-}r}$ is less than $d_{near\text{-}field}$, which means that the radome is always located

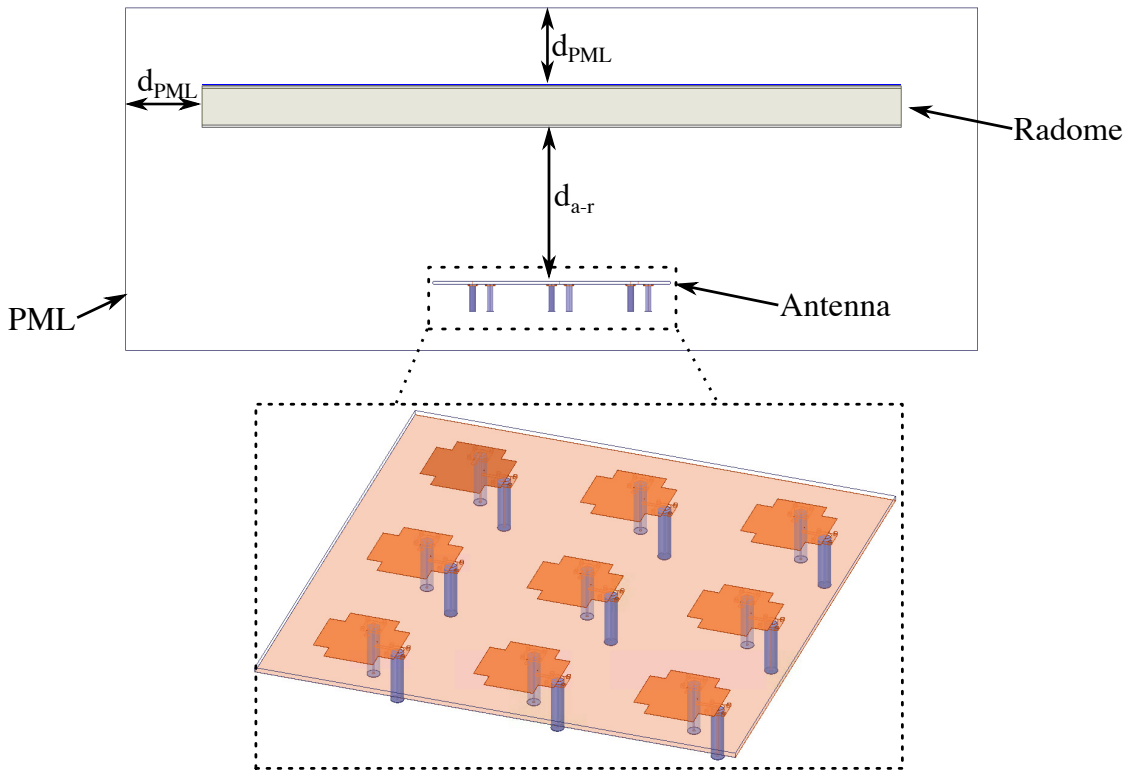

Figure 2.11: A draw of the S-band 3 x 3 antenna array with the radome placed at a distance $d_{a\text{-}r}$ from the antenna. In the figure it is also shown the perfect matching layer (PML) placed at a distance d_{PML} from the radome and the water film of thickness 200 μm.

in the reactive near-field region of the array. The radiation patterns obtained for various $d_{a\text{-}r}$, are shown in Fig. 2.12. In Fig. 2.12a and 2.12b, the radiation patterns calculated at $\phi = 0°$ and $\phi = 90°$ are presented for the scenario of a dry radome. There is no remarkable difference in the co-polarization component between the curve representing the case where no radome was employed (ideal case), with the scenarios including a radome located at various distances from the antenna. The attenuation introduced by the dry radome is 0.2 dB for the worst case scenario analyzed, which corresponds to $d_{a\text{-}r} = \lambda/4$. The cross-polarization component shows some small increase from the ideal case. In Fig. 2.12c and 2.12d, the results considering a wet radome are presented at $\phi = 0°$ and $\phi = 90°$, respectively. For this

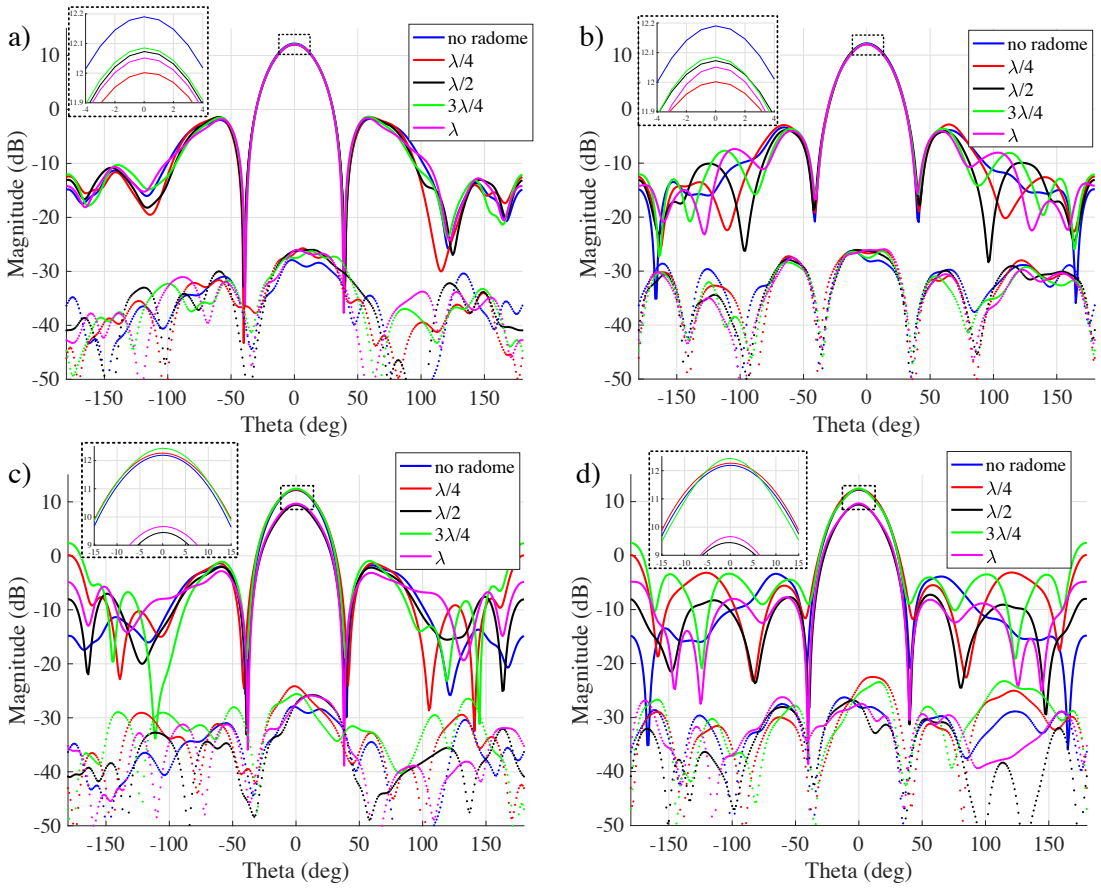

Figure 2.12: The radiation patterns of the S-band 3 x 3 antenna array simulated for various spacing between radome and antenna. Results showed at 3 GHz. a) and b) The radiation patterns obtained by considering a dry radome, for $\phi = 0°$ and 90°, respectively. c) and d) The radiation patterns obtained by considering a wet radome, for $\phi = 0°$ and 90°, respectively. The wet radome was considered by adding a 200 μm-film of water.

scenario, a remarkable difference is noticed for both the co- and cross-polarization components. The variation is observed only at specific distances between the antenna and the radome, suggesting that there is actually a preferred location for the radome. The radiation patterns that show the smallest difference from the ideal case are the ones obtained by placing the radome at $\lambda/4$ and $3\lambda/4$. If the radome is placed at $d_{a\text{-}r} = \lambda/2$ or λ, then an attenuation of 2.8 dB is produced. These results can be explained by thinking of the water layer as a metal plate. Although

water does not properly exhibit electromagnetic properties of a metal plate, its high dielectric constant compared to the radome layers, makes the water film act like a mirror. Therefore, high reflections are generated. By placing the water film at $\lambda/4$, a sort of cancellation effect occurs with the incident fields. Therefore, the reflections and attenuation are minimized. This also occurs at $3\lambda/4$, but $\lambda/4$ represents the best choice because it keeps the distance minimum and therefore, wind load and cost are maintained low.

The results obtained from the last study suggest that there is an optimum distance between the antenna and the radome. Also, the radome stackup and the distance from the antenna should be taken into account when designing the antenna in order to optimize the radiation pattern. It should be also stated that the optimum distance between the antenna and the radome might change based on the type of radiating element selected and its dimensions. Additional studies, as well as experiments, should be performed to provide a conclusive answer.

2.3 Electromagnetic Analysis

This section discusses the methods employed in this dissertation to characterize the RF performance of a radome, either in dry or wet conditions. Various approaches are available in the literature. These approaches can be classified into analytical and numerical analysis. Analytical analysis consists of using formulations, while numerical methods employ simulators. Examples of algorithms used in numerical simulators are the finite element method (FEM), method of moments (MoM), and

geometric optics (GO). In this dissertation, the numerical analysis was performed by using the FEM method.

First, the theoretical study based on transmission line theory (Pozar 2012) will be presented and applied to the study of a dry radome. Then, the validation of the theoretical approach is achieved by performing numerical simulations in High Frequency Structure Simulator (HFSS 2017) software. This section only discusses the methods of analysis, while the related results will be shown in the following chapters.

2.3.1 Transmission Line Model

Transmission line theory connects field analysis to basic circuit theory. Therefore, it has significant importance in electromagnetic analysis. The transmission line model assumes a plane wave propagating, therefore, the study is performed in the far-field region. Although radomes are located in the near-field region of the antenna, in practical cases its performance are tested in far-field (two-probe method later discussed in Chapter 6). Perform radome studies in near-field in very complicated and it is common practice to analyze them in far-field.

In this dissertation, the transmission line model is studied for a multilayer radome. Each layer is characterized by a different thickness and electrical parameters (dielectric constant ϵ and magnetic permeability μ). The materials composing a radome are dielectrics, and therefore, they are fully characterized by ϵ and $\tan\delta$. The magnetic permeability, μ, is assumed to be equal to the free space one (μ_0), and omitted for simplicity. An application of the transmission line model, for a generic

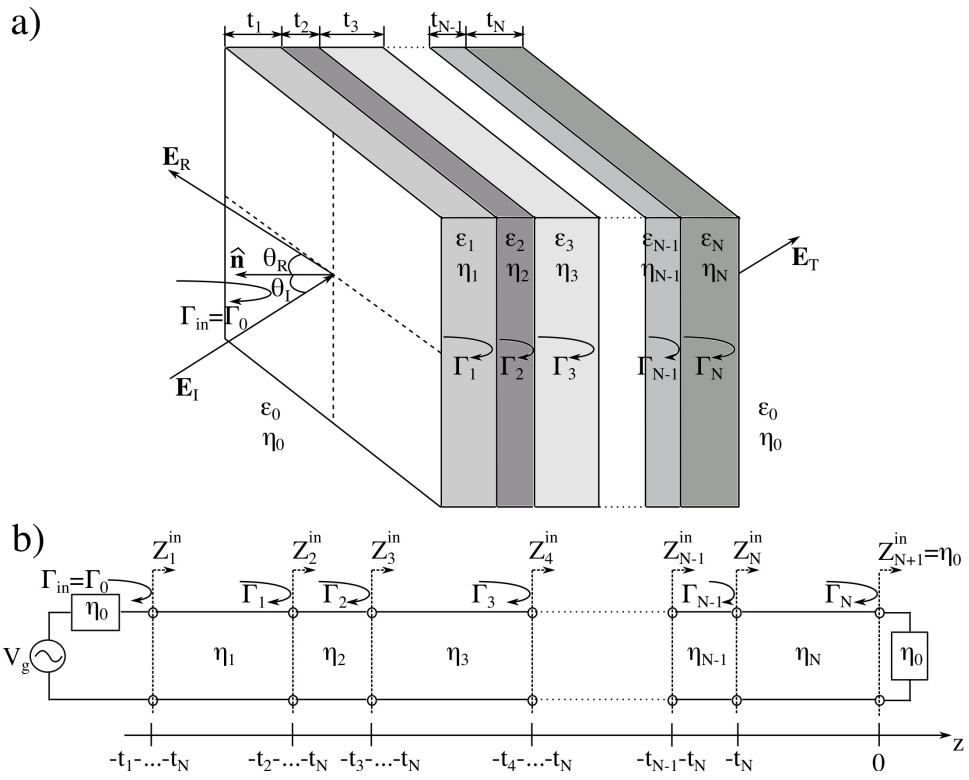

Figure 2.13: Plane wave with oblique incidence to an N-layer sandwich material. a) Field analysis representation. b) Equivalent circuital representation.

N-layer sandwich material, is shown in Fig. 2.13. In Fig. 2.13a, the field analysis is presented. It shows the electric field incident to the surface ($\mathbf{E}_I$) with an angle θ_I, the reflected field ($\mathbf{E}_R$), and the transmitted field ($\mathbf{E}_T$) through the last layer of the compost material. In Fig. 2.13b, the equivalent circuital representation is presented.

The impedance (η) of each layer can be calculated from the relative dielectric constant (ϵ_r), as:

$$\eta = \sqrt{\frac{\mu_0}{\epsilon_0 \epsilon_r}} = \frac{\eta_0}{\sqrt{\epsilon_r}} \tag{2.2}$$

where η_0 is the free-space impedance and it is equal to 377 Ω. From the first stage, layer 0 (air), located at z = -t_1-...-t_N, the reflectance (Γ_{in}^0) is computed for H- and V-polarizations as:

$$\begin{aligned}\Gamma_0^H &= \frac{\eta_0 \cos\theta_1^T - \eta_1 \cos\theta_1^I}{\eta_0 \cos\theta_1^T + \eta_1 \cos\theta_1^I} \\ \Gamma_0^V &= \frac{\eta_0 \cos\theta_1^I - \eta_1 \cos\theta_1^T}{\eta_0 \cos\theta_1^I + \eta_1 \cos\theta_1^T}\end{aligned} \tag{2.3}$$

where θ_1^T is the transmitted angle through layer 1. It is computed as:

$$\theta_1^T = \arccos\left(\sqrt{1 - \frac{\epsilon_0^r}{\epsilon_1^r}\sin\theta_1^I}\right) \tag{2.4}$$

The impedance seen from stage 1 to stage N is calculated as:

$$\begin{aligned}Z_1^{in,H} &= \eta_1\left(\frac{1+\Gamma_0^H e^{-2j\beta_1 r_1}}{1-\Gamma_0^H e^{-2j\beta_1 r_1}}\right) \\ Z_1^{in,V} &= \eta_1\left(\frac{1+\Gamma_0^V e^{-2j\beta_1 r_1}}{1-\Gamma_0^V e^{-2j\beta_1 r_1}}\right)\end{aligned} \tag{2.5}$$

where r_1 is the thickness of layer 1 projected in the direction of the oblique propagation:

$$r_1 = t_1 \cos\theta_1^T \tag{2.6}$$

At the second stage of the circuit (Fig. 2.13b), the reflection coefficient is:

$$\begin{aligned}\Gamma_1^H &= \frac{Z_1^{in,H}\cos\theta_2^T - \eta_2\cos\theta_2^I}{Z_1^{in,H}\cos\theta_2^T + \eta_2\cos\theta_2^I} \\ \Gamma_1^V &= \frac{Z_1^{in,V}\cos\theta_2^I - \eta_2\cos\theta_2^T}{Z_1^{in,V}\cos\theta_2^I + \eta_2\cos\theta_2^T}\end{aligned} \tag{2.7}$$

and the input impedance:

$$Z_2^{in,H} = \eta_2 \left(\frac{1 + \Gamma_1^H e^{-2j\beta_2 r_2}}{1 - \Gamma_1^H e^{-2j\beta_2 r_2}} \right)$$
$$Z_2^{in,V} = \eta_2 \left(\frac{1 + \Gamma_1^V e^{-2j\beta_2 r_2}}{1 - \Gamma_1^V e^{-2j\beta_2 r_2}} \right) \tag{2.8}$$

This procedure is repeated until the last stage of the multi-layer material. The power transmission coefficient (transmittance) computed at the last stage (N+1) of the lossless sandwich material is given by:

$$T_{N+1}^H = 1 - |\Gamma_{N+1}^H|^2$$
$$T_{N+1}^V = 1 - |\Gamma_{N+1}^V|^2 \tag{2.9}$$

The transmission line theory will be applied in Chapter 3 to S- and X-band radomes to calculate the reflectance and attenuation for the dry scenario. Numerical simulations will be performed to study the effect of wet radomes (Chapter 3).

2.3.2 Numerical Analysis

To validate the analytical approach shown in the previous section, a numerical simulation in HFSS was performed. The numerical analysis executed in this dissertation to evaluate the radome performance, uses the infinite array approach. The infinite array approach consists of designing a unit cell of the multi-layer radome of finite dimensions along x- and y-coordinates. Then, by using two coupled master and slave boundary conditions, with one pair set along the x-axis and the other one along the y-axis, the unit cell is replicated infinite times in those directions. By

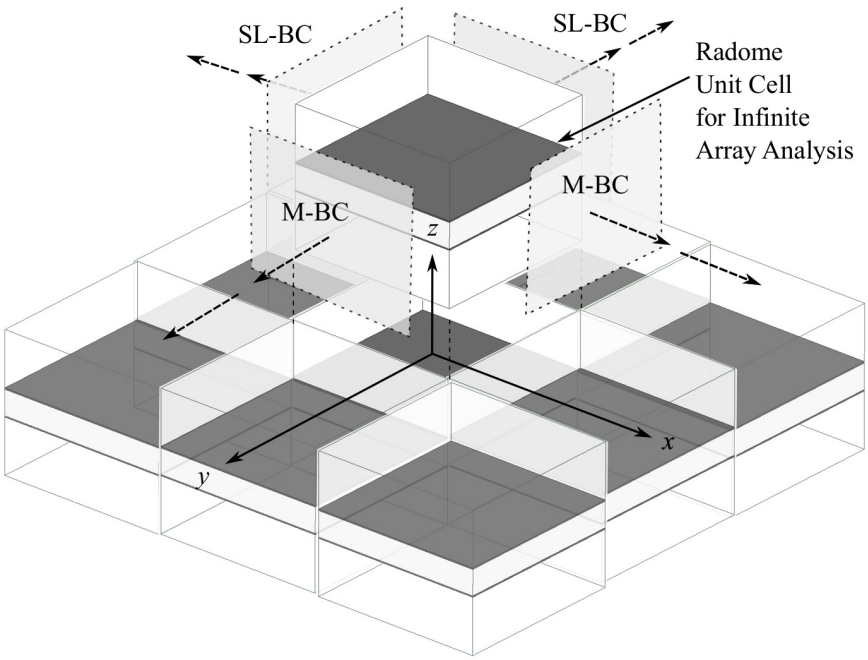

Figure 2.14: A diagram representing the infinite array approach. It is shown the unit cell with master (M) and slave (SL) boundary conditions (BC) and the infinite replication of the unit cell along x- and y-directions.

replicating the unit cell infinite times, border effects are not present and therefore, the reflectance and transmittance computed through the multi-layer radome is only due to the materials composing the radome stackup. To compute the reflectance and transmittance, two floquet ports are defined in the z-direction: one to transmit and the other to receive. A sketch of the infinite array approach is shown in Fig. 2.14.

2.4 Summary

In this chapter the fundamental concepts to design a radome, and the selection of the geometries and the materials, were introduced and discussed. A study was

performed to compare the performance of foam and honeycomb as cores. The results showed that although honeycomb is lower cost than foam and allows bending to realized sharp shapes, it has an anisotropic behavior. Anisotropy is undesired for radomes because various attenuation and reflections are generated at different angles of incidence and therefore, bias in the dual-polarized radar products is introduced. Another important parameter discussed in the chapter, is the distance between the radome and the antenna. Although for a dry radome the distance between the antenna and radome is not relevant, the same analysis repeated for a wet radome showed that $\lambda/4$ minimizes the negative impact of the radome. It was shown that placing the radome at a distance of $\lambda/2$ or λ from the antenna generates an attenuation of 2.8 dB and increases the SLL with respect to a distance of $\lambda/4$. Then, the study suggests that there is an optimum distance to place the radome with respect to the antenna.

To conclude the chapter, an analytical model (transmission line model) was used to analyze the performance of a multi-layer dry radome. The reflectance and transmittance of the H- and V-polarizations present different responses for various steering angles. This result is relevant for dual-polarized weather radars because the radome biases the dual-polarized products. Therefore, it is necessary to account for this effect. Numerical results validated the analytical approach and showed good agreement with the theoretical curves.

Chapter 3

Radome Design and Modeling for Dual-Polarized Weather Radars

This chapter presents the design trade off and modeling for dual-polarized weather radars. Usually, numerical analyses are more accurate than theoretical studies, but the time need for simulation is long. The transmission line model provides a fast and accurate way to study the radome in dry condition. Therefore, it is preferable to employ the transmission line model when possible. However, this technique does not account for absorption, and therefore, the results provided are less accurate than numerical analysis. It is up to the designer to select which method is more convenient based on the scenario considered.

The radomes used for the analysis discussed in this chapter are employed in the Weather Surveillance Radar, 1988, Doppler (WSR-88D), operating in S-band, a purposely made C-band radome (non-operative), and in the PX-1000 that operates in X-band.

3.1 Radome for S-band Weather Radars

The frequency band of the WSR-88D radar is 2.7 - 3 GHz and the operative frequency is 2.85 GHz. A photograph of WSR-88D's spherical radome is presented in

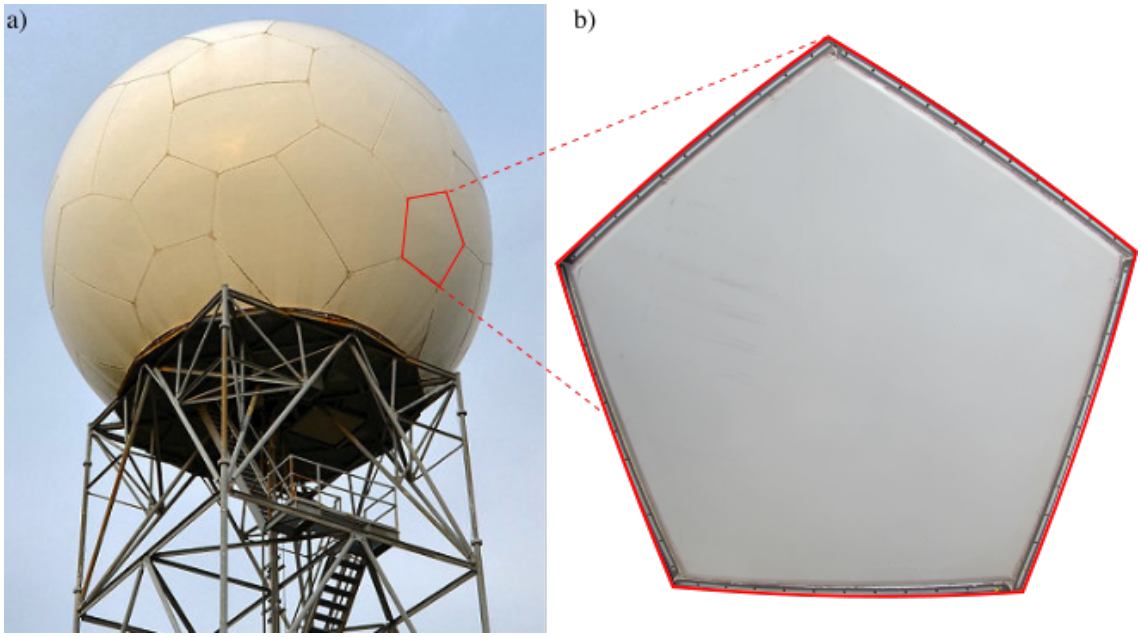

Figure 3.1: a) A photograph of the S-band WSR-88D radome. In the figure, the panelization of the dome is visible. b) A photo of the radome panel employed to perform the experiments discussed in Chapter 6. Photo source: http://research.atmos.ucla.edu/weather.

Table 3.1: The S-band WSR-88D radome stackup employed to evaluate the RF performance. The radome is designed to operate at 2.85 GHz.

Material	**Thickness (mm)**	ϵ_r	**tanδ**
Raincoat	0.28	3.75	0.06
Fiber-glass (outer skin)	1.3	4.2	0.012
Foam (core)	24.73	1.09	0.0017
Fiber-glass (inner skin)	1.3	4.2	0.012

Fig. 3.1a. In Fig. 3.1b, a photo of the radome panel to perform the experiments discussed in Chapter 6 is shown. This is a space frame type of radome (Fig. 2.5). The stackup of the WSR-88D radome is listed in Table 3.1.

The transmission line model is now applied to the dry multilayer sandwich radome of the WSR-88D (Table 3.1). For this scenario $N = 4$. To provide additional validation to the theoretical model, a numerical simulation was performed. Numerical and analytical results are overlapped in Fig. 3.2. In Fig. 3.2a and 3.2b,

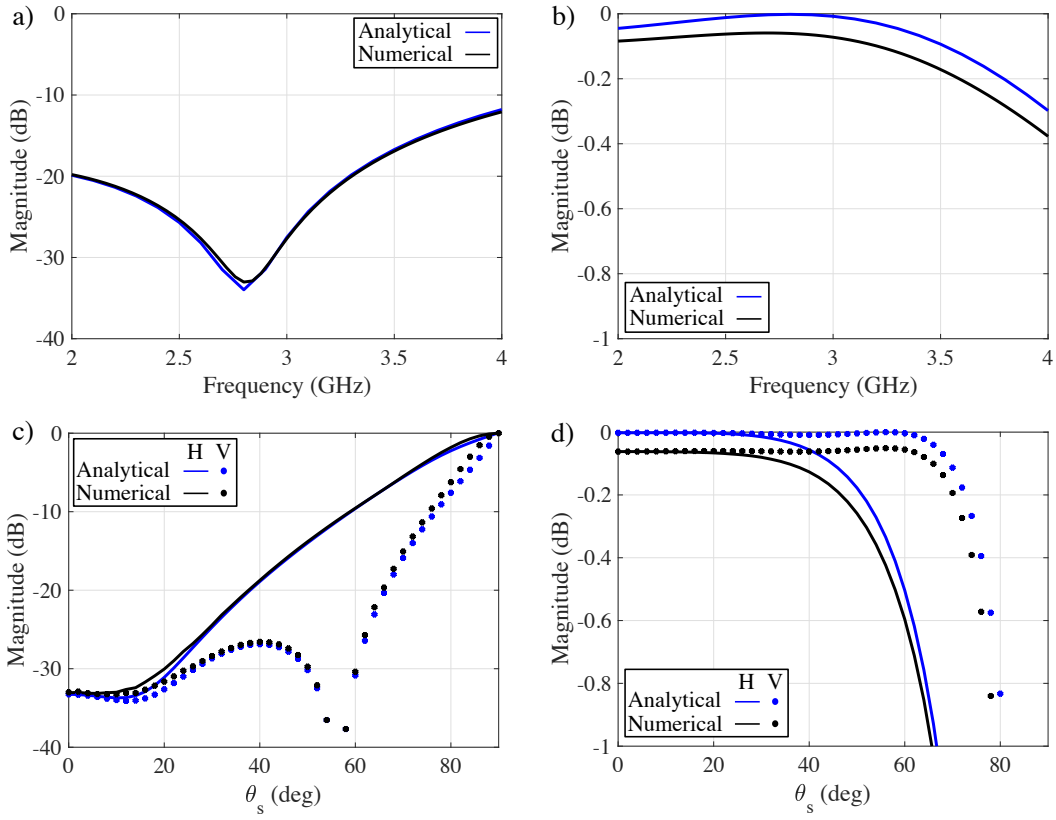

Figure 3.2: A comparison of the reflectance and transmittance between the analytical and numerical studies for the WSR-88D radome (Table 3.1) in dry conditions. The frequency response of the (a) reflectance and (b) transmittance calculated at normal incidence of the plane wave. c) The reflectance and (d) transmittance computed at various steering angles, at 2.85 GHz, for H- and V-polarizations.

the reflectance and transmittance are computed at normal incidence as a function of the frequency. At normal incidence, there is no distinction between the H- and V-polarization of the reflected and transmitted electric fields in case of a flat radome. The difference between the analytical and numerical computed transmittance values is 0.08 dB, which is not critical. In Figs. 3.2c and 3.2d, the transmittance and reflectance are presented as function of the incident angle and computed at 2.85 GHz. For oblique incidence, the H- and V-polarizations present different responses. This is an important result, because it shows that the two components of the signal

are differently affected by the presence of the medium (radome). Therefore, it is expected that dual-polarized radar products will be subjected to various attenuations in the horizontal and vertical polarizations. This difference will increase when water is accumulated on the outer layer of the radome as it will be shown in Chapter 4. Figs. 3.2c and 3.2d also explain why SLL increases with the presence of the radome. It can be noted that the reflectance at normal incidence is below -30 dB, therefore, the main beam is subject to a low level of reflectance. This is not true for the far sidelobes at 50°, which is subject to a reflection coefficient of only -15 dB for the H-polarization.

As noticed, the theoretical and numerical curves show a sufficient agreement and therefore, it shows that the transmission line model is reliable to perform analysis of a dry radome. The theoretical model is faster and the computation requires less memory effort. To save time it is preferable to perform analysis with the theoretical model when possible. When the radome analysis includes water, absorption occurs in the water layer. The transmission line model does not account for absorption, while numerical simulations do. Dry radomes can be analyzed with the transmission line model, while wet radomes require numerical simulations for accurate analysis.

3.2 Radome for C-band Weather Radars

To understand the performance of a radome at a higher frequency, a C-band radome was also analyzed. Because the stackup of a real C-band radome was not available, a scaling of the radome discussed in the previous section is done. The C-band radome

Table 3.2: The radome stackup operating at C-band. The radome is designed to operate at 5.4 GHz.

Material	**Thickness (mm)**	ϵ_r	**tanδ**
Raincoat	0.13	3.75	0.06
Fiber-glass (outer skin)	0.98	4.2	0.012
Foam (core)	11.7	1.09	0.0017
Fiber-glass (inner skin)	0.98	4.2	0.012

is designed to operate at 5.4 GHz. Mainly the thickness of the core was reduced to change the frequency of operation of the radome. However, the thicknesses of the raincoat and skin layers were slightly decreased to reduce the losses. The stackup of the C-band radome is presented Table 3.2.

Analytical and numerical results for the C-band radome are compared in Fig. 3.3. In Fig. 3.3a the reflectance calculated at various frequency points is presented. The theoretical curve approximates well the numerical result. A small difference is noted at the resonant frequency (5.4 GHz). The transmittance computed as a function of the frequency is shown in Fig. 3.3b. A mismatch of 0.06 dB at 5.4 GHz is noticeable between the numerical and theoretical values. This difference is not particularly critical and it is due to the absorption occurring mainly in the raincoat and skin layers, because the corresponding materials are considerably lossy. The reflectance and transmittance are calculated as a function of the steering angle in Fig. 3.3c and 3.3d showing both H- and V-polarizations. Again, in this case the H- and V-polarizations present different responses at various steering angles. The mismatch between the numerical and theoretical results decrease with the steering angle and they find very good approximation at large angles.

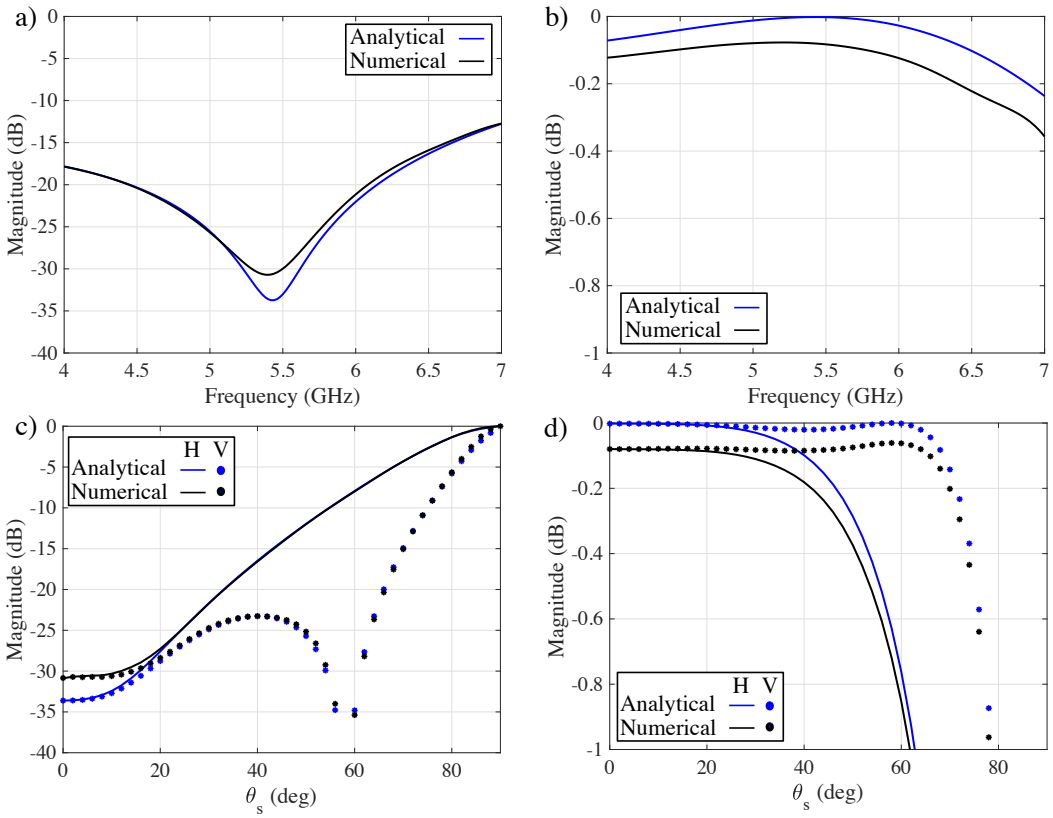

Figure 3.3: A comparison of the reflectance and transmittance between the analytical and numerical studies for the C-band radome (Table 3.2) in dry conditions. The frequency response of the (a) reflectance and (b) transmittance calculated at normal incidence of the plane wave. c) The reflectance and (d) transmittance computed at various steering angles, at 5.4 GHz, for H- and V-polarizations.

3.3 Radome for X-band Weather Radars

For the X-band radome analysis, the radome stackup of the PX-1000 radar is used (Fig. 2.7). The radome stackup is presented in Table 3.3.

As for the case of the C- and S-band radomes previously analyzed, the transmission line model is used to analytically characterize the radome performance and then numerical simulations will be considered to provide a more accurate analysis.

Results obtained applying the transmission line model are overlapped with the numerical analysis in Fig. 3.4. In Fig. 3.4a, the reflectance plotted as a function of

Table 3.3: The PX-1000 radome stackup employed for the X-band analysis to estimate the reflectance and attenuation. The radome is designed to operate at 9.55 GHz.

Material	**Thickness (mm)**	ϵ_r	**tan**δ
Raincoat	0.127	3.65	0.035
E-glass Expoy (outer skin)	0.508	4.2	0.017
Nomex (core)	6.8	1.1	0.003
E-glass Expoy (inner skin)	0.508	4.2	0.017

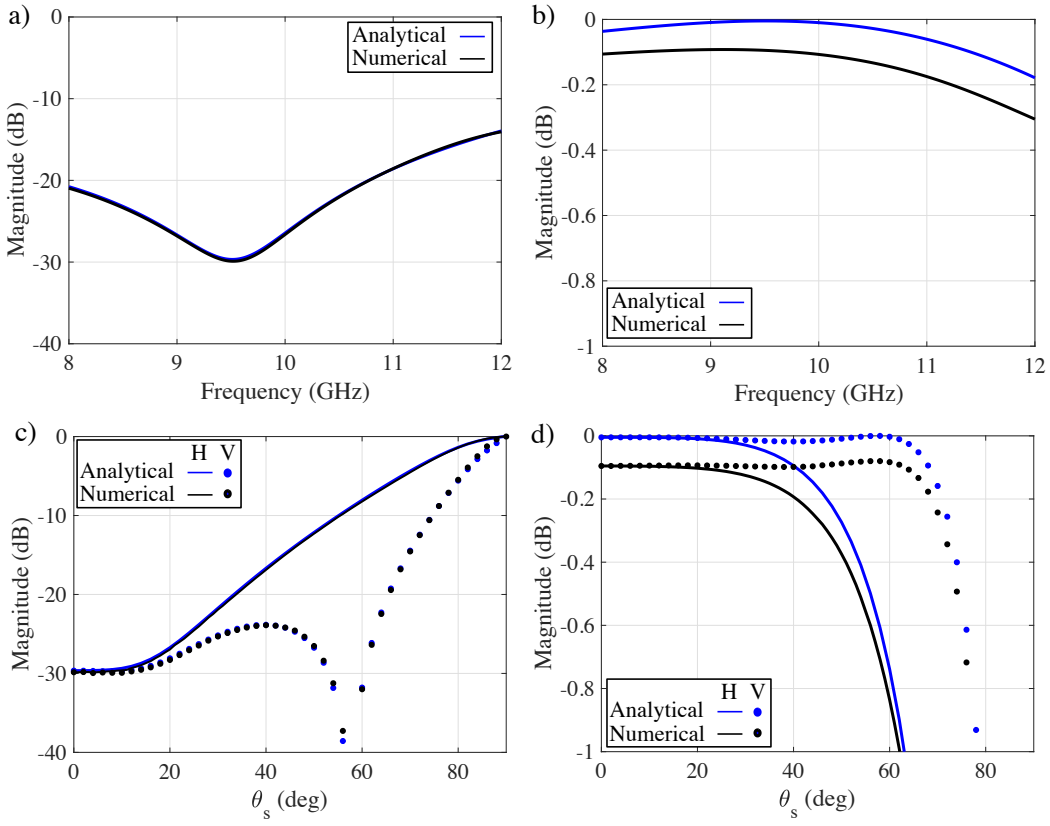

Figure 3.4: A comparison of the reflectance and transmittance between the analytical and numerical studies for the PX-1000 radome (Table 3.3) in dry conditions. The frequency response of the (a) reflectance and (b) transmittance obtained at normal incidence of the plane wave. c) The reflectance and (d) transmittance calculated at various steering angles, at 9.55 GHz, for H- and V-polarizations.

the frequency is shown. Good agreement between the two studies is demonstrated. The resonance peak is located at 9.55 GHz as expected. Discrepancy between the two methods can be observed in Fig. 3.4b for the transmittance calculated as a function of the frequency. The difference between the two curves is about 0.08 dB and it is attributed to the limitation of the transmission line model. The reflectance and transmittance are calculated for various steering angles in Fig. 3.4c and 3.4d. The difference between the numerical and analytical curves decreases with the angle of incidence. As for the radome studies performed at C- and S-bands, the H- and V-polarizations present different attenuation.

3.4 Summary

In this chapter the transmission line model and numerical analysis performed in HFSS were used to evaluate the performance of a dry radome. Radomes operating at S-, C-, and X-bands were analyzed. Results show acceptable agreement between the two methods demonstrating the validity of the theoretical approach. While good agreement was found in S- and X-bands for the reflectances computed with the analytical and numerical models, a 4-dB difference was noted at C-band between the two techniques. For all the frequency bands analyzed, there is a mismatch between the transmittances computed with the two models. In particular this difference increases with the frequency band analyzed: 0.03 dB at S-band, 0.06 at C-band, and 0.08 dB at X-band. This is attributed to the limitation of the transmission line model.

Now that the analysis of a dry radome is completed, the investigation will be moved to the scenario where water occurs. The next chapter will provide the theoretical model to characterize the dielectric constant of water and estimate the thickness of the water formation under various rain rates.

Chapter 4

Wet Radome Analysis

In this chapter, the electromagnetic properties of water and the possible formations occurring on the radome surface are presented and discussed. First of all, it is necessary to have a model that calculates the electromagnetic properties of water. Afterwards, the calculation of the reflectance, absorptance, and attenuation occurring in the water layer is performed. The attenuation is calculated by combining the part of the signal that is reflected and absorbed by the water layer. Depending on the hydrophobic property of the radome outer skin, water distributes either as droplets and rivulets, or as a continuous film. The first scenario occurs in cases where the raincoat of the radome presents hydrophobic properties, while the second one happens when the raincoat is not water-repellent (hydrophilic). Examples of different water formations are shown in Fig. 4.1.

An analytical model to estimate the amount of water collected by a radome sample considering various water formations (continuous film or droplets), was developed to compute the attenuation introduced by the wet radome (Salazar et al. 2014). This model takes into account the radome shape and the rain intensity. To quantify the level of signal absorbed by the water, a mathematical model was created and validated through simulation using HFSS (version 2017).

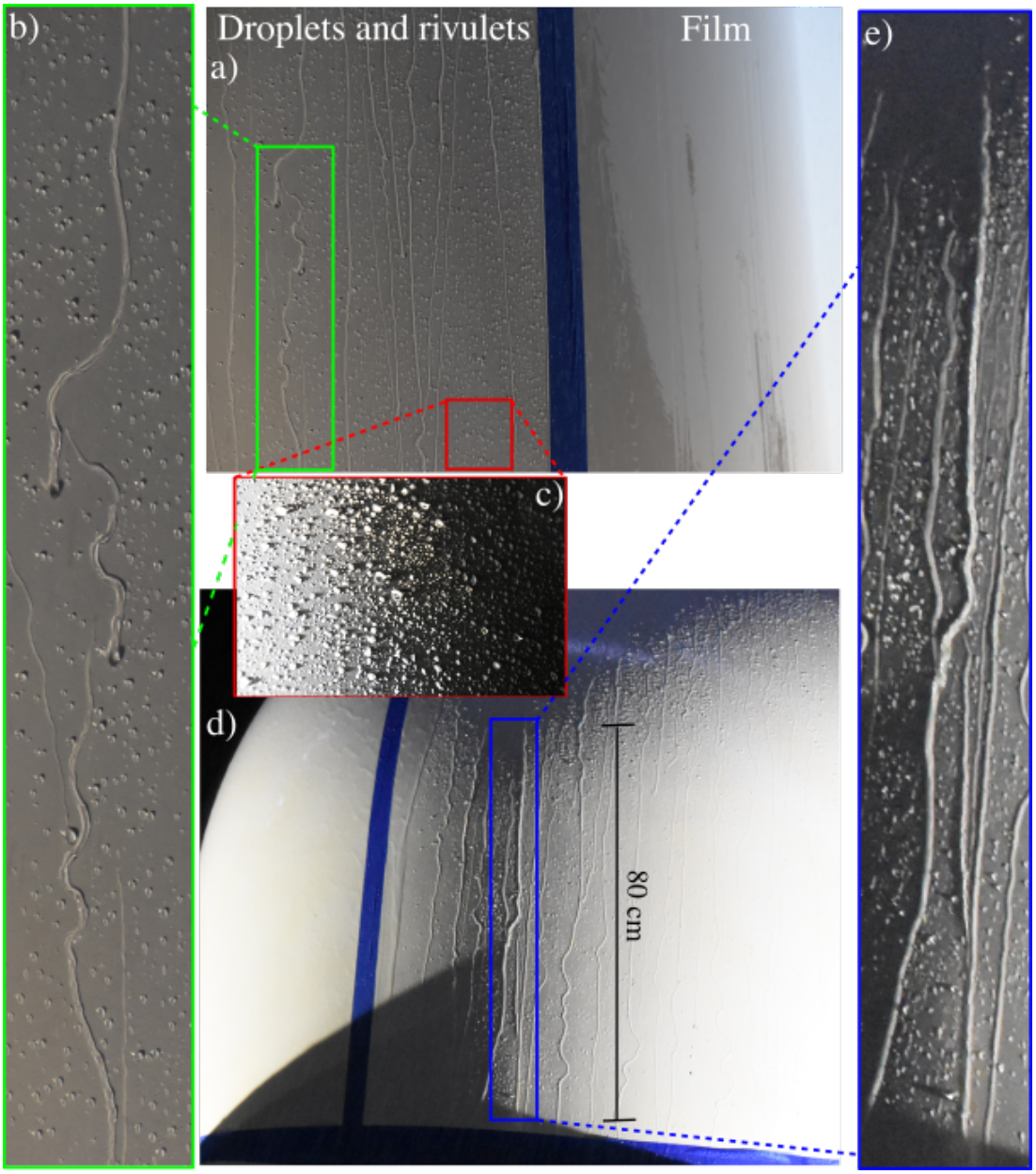

Figure 4.1: The possible water formations occurring on the radome surface of the X-band PX-1000 radar. Photographs taken during the experiment published in Mancini, Salazar, Lebrón and Cheong (2018*b*). a) The radome showing droplet and rivulets on a side and continuous film on the other side. b) A close-up of the radome presenting droplets and rivulets. c) A close-up of the radome showing droplet formation. d) The same radome photographed from a different prospective. e) Another close-up showing rivulets.

4.1 Water Properties

A complete description of the problem includes starting with the definition of the dielectric constant of a lossy medium (water), then calculating the transmittance through a slab of water for different thicknesses. The complex dielectric constant (ϵ_c) of a lossy medium is defined as:

$$\epsilon_c = \epsilon - j\frac{\sigma}{\omega} \tag{4.1}$$

the second term of Eq. 4.1 represents the losses associated to the conductivity (σ). The relative dielectric constant is expressed by:

$$\epsilon_r = \frac{\epsilon_c}{\epsilon_0} = \frac{\epsilon}{\epsilon_0} - j\frac{\sigma}{\omega\epsilon_0} = \epsilon' - j\epsilon'' \tag{4.2}$$

From Zhang (2017), the real and imaginary part of ϵ_r can be expressed as:

$$\begin{aligned} \epsilon' &= \epsilon_\infty + \frac{(\epsilon_s - \epsilon_\infty)[1 + (\lambda_s/\lambda)^{1-\nu}\sin(\nu\pi/2)]}{1 + 2(\lambda_s/\lambda)^{1-\nu}\sin(\nu\pi/2) + (\lambda_s/\lambda)^{2(1-\nu)}} \\ \epsilon'' &= \frac{(\epsilon_s - \epsilon_\infty)(\lambda_s/\lambda)^{1-\nu}\cos(\nu\pi/2)}{1 + 2(\lambda_s/\lambda)^{1-\nu}\sin(\nu\pi/2) + (\lambda_s/\lambda)^{2(1-\nu)}} + \frac{\sigma\lambda}{2\pi c\epsilon_0} \end{aligned} \tag{4.3}$$

The formulas in Eq. 4.3 are the Debye's equations with the modifications introduced by Cole and Cole (1941) to account for spread effects. ϵ_∞ is the high frequency dielectric constant, ϵ_s is the static dielectric constant, λ_s is the relaxation wavelength, and ν is the spread parameter. These quantities are dependent on the temperature and can be expressed as (Zhang 2017):

$$\epsilon_s = 78.54[1 - 4.579\times10^{-3}(t-25) + 1.19\times10^{-5}(t-25)^2 - 2.8\times10^{-8}(t-25)^3] \tag{4.4}$$

$$\epsilon_\infty = 5.27137 + 0.0216474t - 0.00131198t^2 \tag{4.5}$$

$$\begin{aligned} \nu &= -\frac{16.8129}{t+273} + 0.0609265 \\ \lambda_s &= 0.00033836e^{2513.98/(t+273)} \end{aligned} \tag{4.6}$$

In Eqs. 4.4 - 4.6, the temperature (t) is expressed in degrees Celsius. The tangent loss is the parameter that quantifies the dissipation of electromagnetic energy occurring inside a lossy material. It refers to the phasor in the complex plane whose real and imaginary components are the resistive, lossy part, and reactive, lossless part. It is defined by the following relationship (Pozar 2012):

$$\tan\delta = \frac{\omega\epsilon'' + \sigma}{\omega\epsilon'} \tag{4.7}$$

ϵ_r and tanδ of fresh water were computed using Eqs. 4.4, 4.3, and 4.7 for $\sigma = 1.1117\times10^{-4}$ S m^{-1}, and they are plotted for different temperatures in Fig. 4.2. In the figure, ϵ_r and tanδ are computed in the frequency range from 2 to 11 GHz to compare the electromagnetic performance of water from S- to X-band.

Considering a plane wave propagating in a lossy medium, the propagation constant can be written as:

$$\gamma = \alpha + j\beta = \frac{\omega N}{c} \tag{4.8}$$

where c is the speed of light in the vacuum, and N is the complex refraction index of the medium defined by:

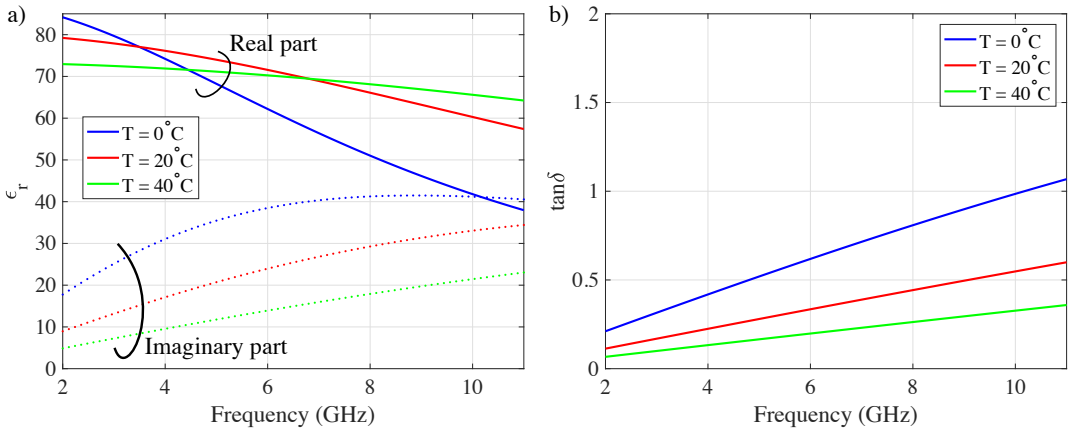

Figure 4.2: The dielectric parameters of water for different temperatures. a) The real and imaginary part of the relative dielectric constant. b) The tangent loss.

$$N = \sqrt{\frac{\epsilon\mu}{\epsilon_0\mu_0}} = n + jk \tag{4.9}$$

The power of such a wave propagating in the z-direction, is defined by the Poynting vector:

$$\mathbf{S} = \frac{1}{2} Re\{\mathbf{E} \times \mathbf{H}^*\} \tag{4.10}$$

The magnitude of $\mathbf{S}$ is called irradiance (I). If the medium is lossy (as in the case of water), part of the energy is absorbed by the material. Therefore, the irradiance is attenuated by the following law (Bohren and Huffman 1983):

$$I = I_0 e^{-\alpha z} \tag{4.11}$$

The absorption coefficient (α) determines the amount of energy lost by absorption inside the material. The absorption coefficient is defined as:

$$\alpha = \frac{4\pi k}{\lambda} \tag{4.12}$$

The imaginary part of the refractive index (k in Eq. 4.9) determines the rate at which the electromagnetic energy is lost by the material absorption. Considering a plane wave propagating in two semi-infinite media, where the first one is non-absorbing (air) with a refraction index N_1, and the second material is absorbing with a refractive index $N_2 = n_2 + jk_2$, part of the wave is reflected and part is transmitted through the first interface. The incident, reflected, and transmitted electric fields are labeled $\mathbf{E_I}$, $\mathbf{E_R}$, and $\mathbf{E_T}$, respectively. The reflection (r) and transmission (t) coefficients determine the amount of electric field reflected and transmitted. These coefficients are defined as:

$$r = \frac{|\mathbf{E_R}|}{|\mathbf{E_I}|} \qquad \text{and} \qquad t = \frac{|\mathbf{E_T}|}{|\mathbf{E_I}|} \tag{4.13}$$

Defining the ratio $N_1/N_2 = m$, the coefficients introduced above can be rewritten as (Bohren and Huffman 1983):

$$\tilde{r} = \frac{1-m}{1+m} \qquad \text{and} \qquad \tilde{t} = \frac{2}{1+m} \tag{4.14}$$

The reflectance (R) and reflection coefficient (as well as transmittance - T - and transmission coefficient) are directly related:

$$R = |\tilde{r}|^2 = \left|\frac{1-m}{1+m}\right|^2 \qquad \text{and} \qquad T = |\tilde{t}|^2 = \left|\frac{2}{1+m}\right|^2 \tag{4.15}$$

Considering an absorbing dielectric slab (medium 2, water) of thickness h, and refraction index $N_2 = n_2 + jk_2$, placed in between two semi-infinite media made of air, both with $N_1 = n_1$, the folded voltage and power transmission and reflection

coefficients t_{slab}, T_{slab}, r_{slab}, R_{slab} at the air-water interface, are defined as in Bohren and Huffman (1983):

$$\begin{aligned} r_{slab} &= \frac{\tilde{r}(1-e^{j2kN_2h})}{1-\tilde{r}^2e^{j2kN_2h}} \\ R_{slab} &= |r_{slab}|^2 \end{aligned} \tag{4.16}$$

$$\begin{aligned} t_{slab} &= \frac{4m}{(m+1)^2}\frac{e^{-jkN_1h}}{(e^{-jkN_2h}-\tilde{r}^2e^{jkN_2h})} \\ T_{slab} = |t_{slab}|^2 &= \frac{(1-R)^2+4R\sin^2\psi}{R^2e^{-\alpha h}+e^{\alpha h}-2R\cos(\xi+2\psi)} \end{aligned} \tag{4.17}$$

where:

$$\psi = \tan^{-1}\left(\frac{2n_1k_2}{n_2^2+k_2^2-n_1^2}\right) \qquad 0 \le \psi \le \pi, \qquad \xi = \frac{4\pi n_2 h}{\lambda} \tag{4.18}$$

α was already introduced in Eq. 4.12, and for this specific case, k needs to be replaced by k_2. The parameter k (without subscription), in Eqs. 4.16 and 4.17, is the wave number ($2\pi/\lambda$). A portion of the electromagnetic wave is transmitted through the first boundary. When it reaches the second interface, it partially reflected back to the first boundary and partially transmitted through the second boundary of the slab. This mechanism happens inside the slab infinite times, generating infinite terms that produce the total (folded) reflected or transmitted energy, or equivalently, the folded reflectance or transmittance. A sketch of this scenario is presented in Fig. 4.3 for an angular incidence of the electric field. In the figure, the transmitted field through the first interface is incident ($\mathbf{E_{I'}}$) to the second interface, which reflects part of the field that is incident to the first interface repeatedly ($\mathbf{E_{I''}} = \mathbf{E_{R'}}$). The total transmitted irradiance is (Bohren and Huffman 1983):

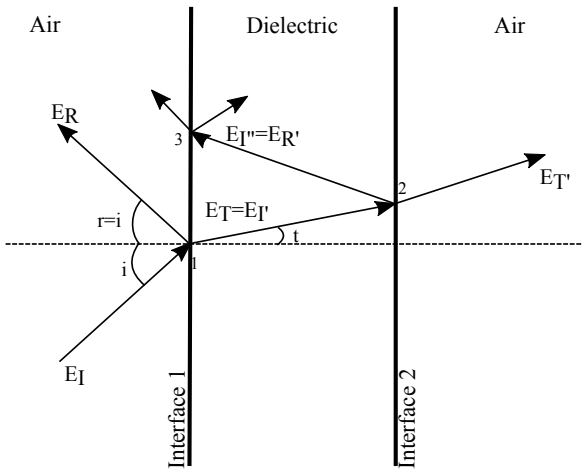

Figure 4.3: A dielectric slab separating two media made of air. The sketch shows angular incidence in order to make the representation easier. Shown in the illustration are the angles of incidence, reflection, and transmission (i, r, and t), as well as the incident, reflected, and transmitted electric fields ($\mathbf{E_I}$, $\mathbf{E_R}$, and $\mathbf{E_T}$) at the first interface. Also shown is the transmitted field through the second interface ($\mathbf{E_{T'}}$). The figure shows the multiple reflections occurring inside the slab. To avoid complicating the illustration, this mechanism is shown only three times, once at each interface.

$$I_t = I_i(1-R)^2 e^{-\alpha h}(1 + R^2 e^{-2\alpha h} + R^4 e^{-4\alpha h} + \cdots) \tag{4.19}$$

the infinite series can be written as:

$$T_{slab} = \frac{(1-R)^2 e^{-\alpha h}}{1 - R^2 e^{-2\alpha h}} \tag{4.20}$$

Eq. 4.20 is an approximation of Eq. 4.17 when the absorption (αh) is large. In this case, the oscillatory terms $\sin^2\psi$ and $\cos(\xi + 2\psi)$, are small compared to the exponential term, and they can be ignored (Bohren and Huffman 1983). The same discussion applies to the reflectance.

In the case of a plane wave incident on a boundary separating two lossless media, the law of energy conservation can be written in terms of transmittance and reflectance, as (Balanis 2012):

$$T + R = 1 \tag{4.21}$$

In the scenario where losses occur (absorbing material), Eq. 4.21 must be rewritten taking into account the portion of the energy absorbed (Wallace and Hobbs 1977; Antonets et al. 2008):

$$T + R + A = 1 \tag{4.22}$$

In Eqs. 4.21 and 4.22, T and R are the folded reflectance and transmittance for the case of a slab or multilayer material.

An analytical model was developed to evaluate the absorption occurring inside a slab of water with various thicknesses, at the temperature of 20° C. First, ϵ_s and ϵ_∞ were computed for the selected temperature from Eqs. 4.4 - 4.6, then ϵ', ϵ'', and $\tan\delta$ were obtained from Eqs. 4.3 and 4.7, respectively (Fig. 4.2 for $T = 20°$ C). Then the reflectance and transmittance through the slab were calculated using Eqs. 4.16 and 4.17. The same scenario was replicated in Ansys HFSS. The dielectric properties (ϵ' and tanδ) of the water in the simulator were set to be frequency dependent, as in Fig. 4.2, to more accurately describe the characteristics of the water. The situation presented emulates the water film that forms over the outer surface of radomes in real scenarios. The results computed by the analytical case are overlapped with the HFSS simulations in Fig. 4.4 for a slab of water without the radome. The results show good agreement between the two methods. In Fig. 4.4a, there is a noticeable increase of the reflectance with the frequency and thickness of the slab. In contrast, in Fig. 4.4b the transmittance is higher at lower frequencies and for thinner water

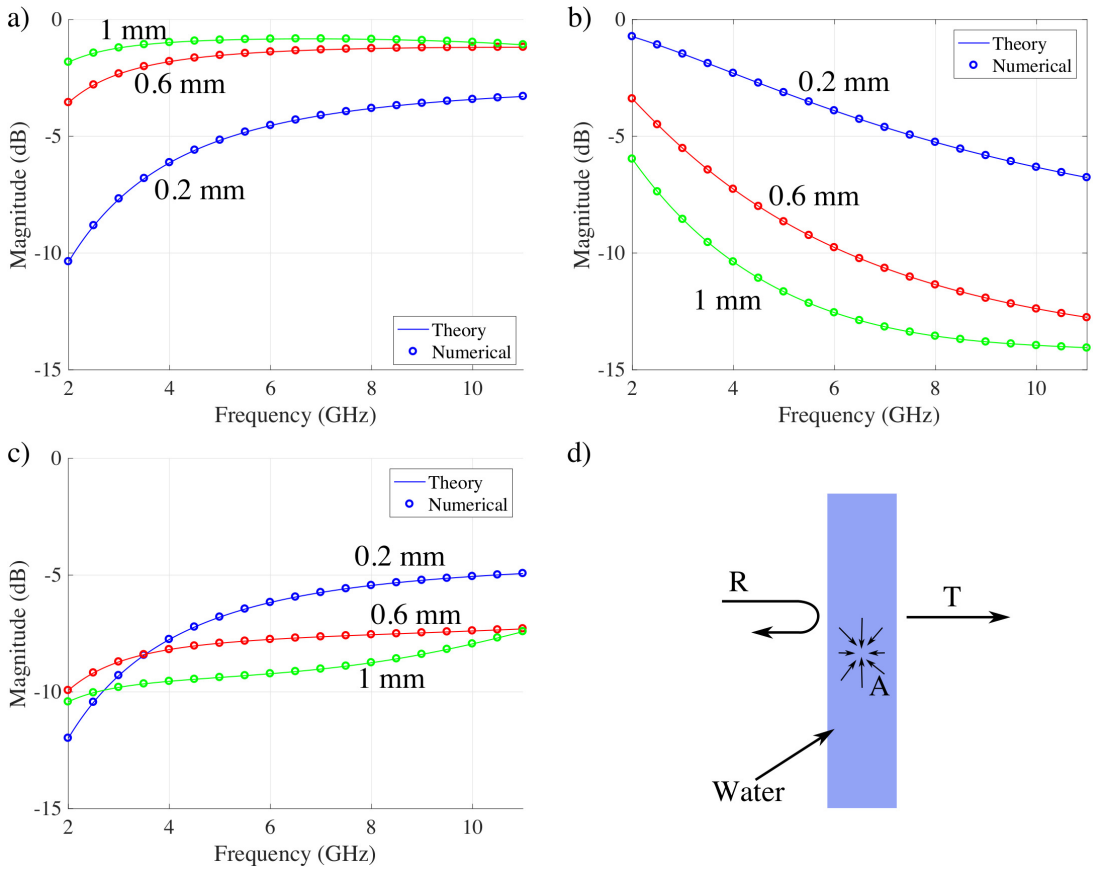

Figure 4.4: The comparison between the analytical model and HFSS simulations for different thicknesses of the slab of water (no radome included) at 20° C. a) Reflectance. b) Transmittance. c) Absorptance. d) Schematic representation of the scenario discussed.

films. The absorption in Fig. 4.4c was computed using Eq. 4.22 as a function of the known quantities R and T, because they are directly computed or simulated. The absorption is lower at S-band frequencies and increases approaching X-band. The highest absorption occurs for the thinnest slab (0.2 mm) of water. Fig. 4.4a shows that by increasing the thickness of the slab, the reflectance rises while the transmittance decreases, because the second term at the denominator of Eq. 4.17 becomes dominant. The opposite case occurs when the thickness of the layer is reduced. A draw of the scenario is presented in Fig. 4.4d.

4.2 Film Formation

This case presents when the outer skin does not have hydrophobic characteristics. Water distributes as a continuous film rather than droplets. The film might not be uniform in real scenarios, due to radome imperfections or wind presence. In this work, a uniform laminar flow is assumed for the purpose of not overcomplicating the model. The thickness of the water film can be computed as function of the rain rate and tilting angle as (Perry 1997):

$$t_{flat} = \sqrt[3]{\frac{3\Gamma\mu}{\rho^2 g \sin\theta_i}} \tag{4.23}$$

where μ is the dynamic viscosity of water (10^{-3} kg m^{-1} s^{-1}), ρ is the density of water (998.2 kg m^{-3}), g is the gravitational acceleration (9.81 m s^{-2}), θ_i is the inclination angle with respect to the horizontal plane, and Γ is the liquid mass flow rate per unit width of surface (kg m^{-1} s^{-1}). The relation between Γ and the rain rate (R) for a square flat radome is given by:

$$\Gamma = \rho \frac{RA_p}{3600 \times 10^3} \frac{1}{W} \tag{4.24}$$

The denominator in Eq. 4.24 expresses the rainfall rate in m s^{-1}. Furthermore, because the rain rate is defined as the water accumulated per unit time on a surface of 1 m^2, it is then necessary to scale the rain rate to the area of the radome projected in the direction of the rain (A_p, where subscript p stands for "projected"). Finally, W is the width (m) of the radome through which the water can fall off the surface.

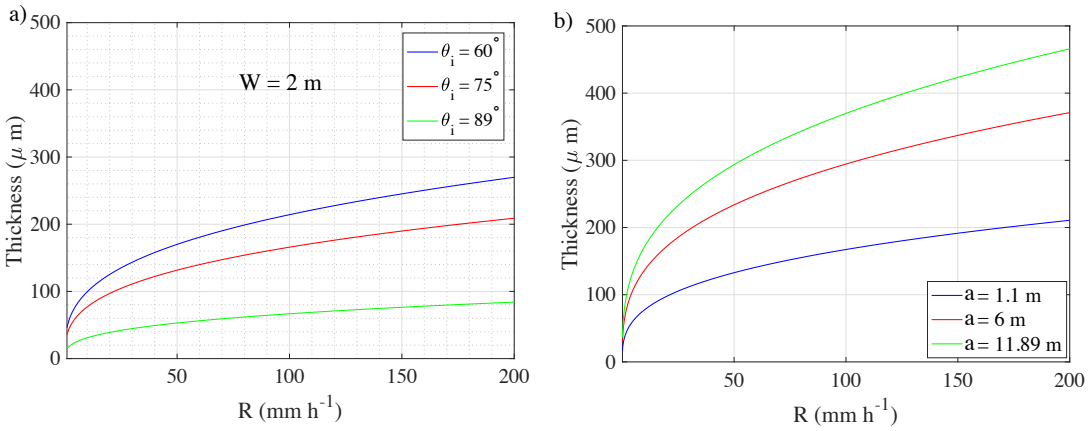

Figure 4.5: The calculated film thickness as a function of the rain rate. a) Thickness computed for a flat radome with width equal to 2 m, at various inclination angles. b) Thickness computed for a spherical radome with different radii.

The projected area for a square radome, computed in the direction of fall of the rain, is given by:

$$A_p = W^2 \cos\theta_i \tag{4.25}$$

For a spherical radome, the thickness is given by Gibble (1964):

$$t_{sphere} = \sqrt[3]{\frac{3\mu Ra}{2\rho g}} \tag{4.26}$$

where a is the radius of the spherical radome (m). The film thicknesses computed as a function of the rain rate for a flat and spherical surface are shown in Fig. 4.5. In Fig. 4.5a, the thickness is calculated for various inclination angles of a square surface with width (W) equal to 2 m. In Fig. 4.5b, the film thickness is obtained considering different radii of the spherical radome. The results show that the bigger is the radome surface, the more water collects and therefore, the thicker the water film accumulated.

4.2.1 S-band Study

A study performed to evaluate the performance of an S-band wet radome is here discussed. The radome considered in this study is the WSR-88D (Table 3.1). Its radius is 11.89 m. The dielectric constant and tangent loss of water at 20° C at the frequency of operation of the radar considered (2.85 GHz), are 78.13 and 0.16, respectively. Numerical results are presented in Fig. 4.6 for the reflectance and the transmittance calculated at various rain rates. The results show how critical is the formation of a thick film on an S-band radome. The reflectance increases more than 20 dB at 2.85 GHz which in terms of transmittance is equivalent to a 4 dB-attenuation for the thickest layer of water analyzed (Fig. 4.6a and 4.6b, respectively). Both reflectance and transmittance get worst as the steering angle increases (Fig. 4.6c and 4.6d).

4.2.2 X-band Study

A study performed to evaluate the performance of an X-band wet radome is here discussed. The radome stackup considered is the one presented in Table 3.3. The dielectric constant and tangent loss of water at 20° C at the frequency of operation of the radar considered (9.55 GHz), are 61.61 and 0.52, respectively. To make a proper comparison to the S-band case, the radius used for this analysis was selected to be the same (11.89 m) so to have the same water thickness (Eq. 4.26). Numerical results are presented in Fig. 4.7 for the reflectance and the transmittance calculated at various rain rates. Results show how critical is the formation of a thick film on an

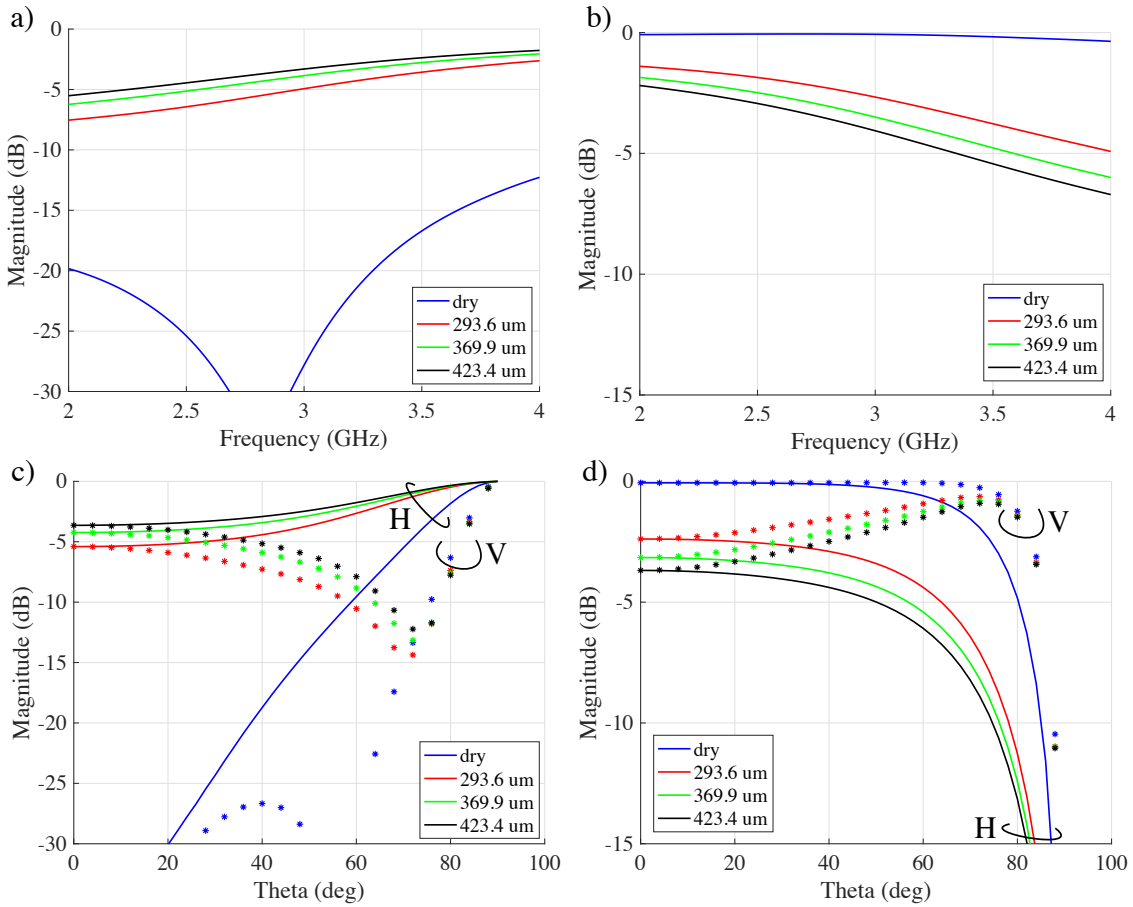

Figure 4.6: Numerical results obtained for the wet S-band radome (Table 3.1) compared to the dry scenario. a) and b) Reflectance and transmittance, respectively, as a unction of the frequency. c) and d) Reflectance and transmittance as a function of the steering angle.

X-band radome. The reflectance increases of 20 dB at 9.55 GHz which in terms of transmittance is equivalent to a 10.5 dB-attenuation for the thickest layer of water analyzed (Fig. 4.7a and 4.7, respectively). Both reflectance and transmittance get worst as the steering angle increases (Fig. 4.7c and 4.7d).

Comparing the results in Figs. 4.6 and 4.7 it is easily noted how the effect of water is more critical at higher frequencies. A comparison of the transmittances between S- and X-band cases show that for the thickest layer of water considered, a 4 dB- and 10.5 dB-attenuation is calculated, respectively.

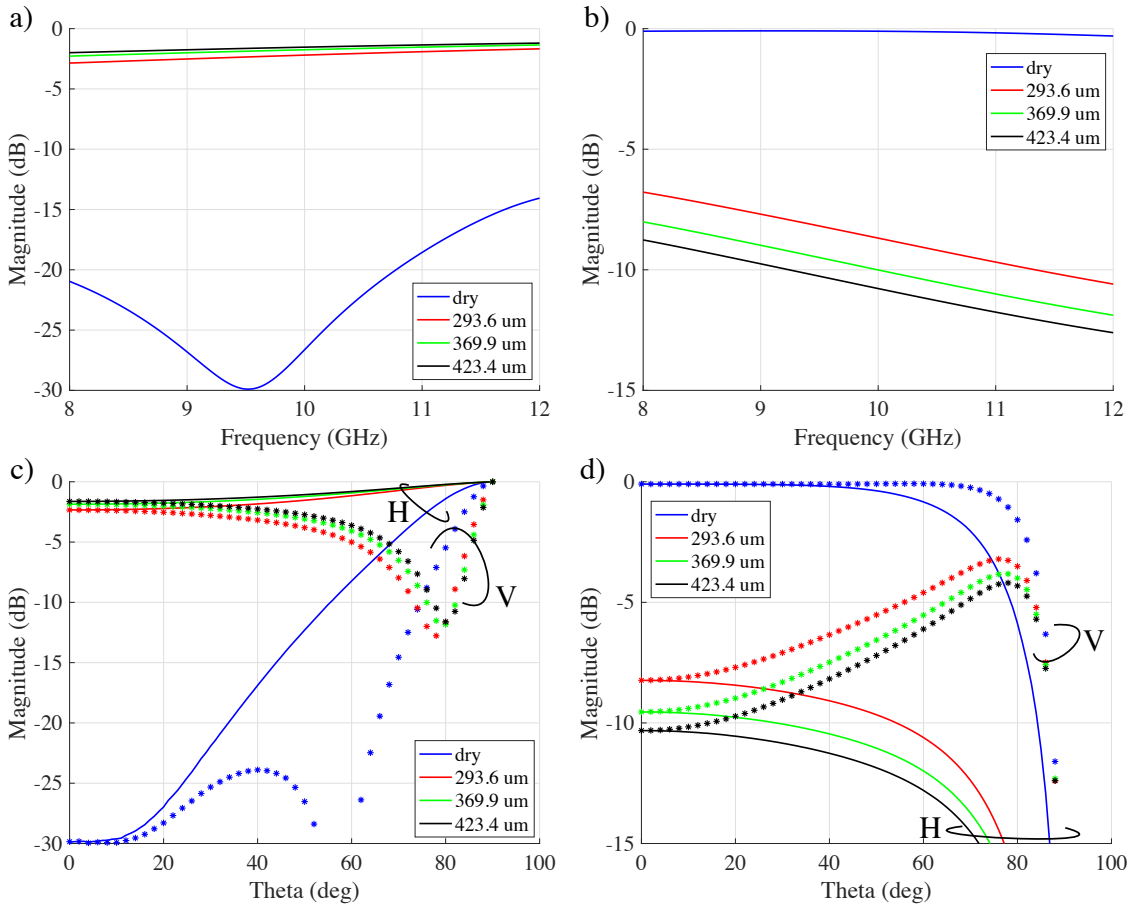

Figure 4.7: Numerical results obtained for the wet X-band radome (Table 3.3) compared to the dry scenario. a) and b) Reflectance and transmittance, respectively, as a unction of the frequency. c) and d) Reflectance and transmittance as a function of the steering angle.

4.3 Droplet Formation

An analytical model that estimates the amount of droplet collected by a radome surface was developed by Salazar et al. (2014). In this dissertation, an extension of Salazar's model is proposed. The drop-size distribution (DSD), indicated by $N(D)$, is the parameter commonly employed to describe the amount of droplets with a specified diameter contained in a cubic meter of air. Gamma distribution was used to represent the DSD by Zhang et al. (2001):

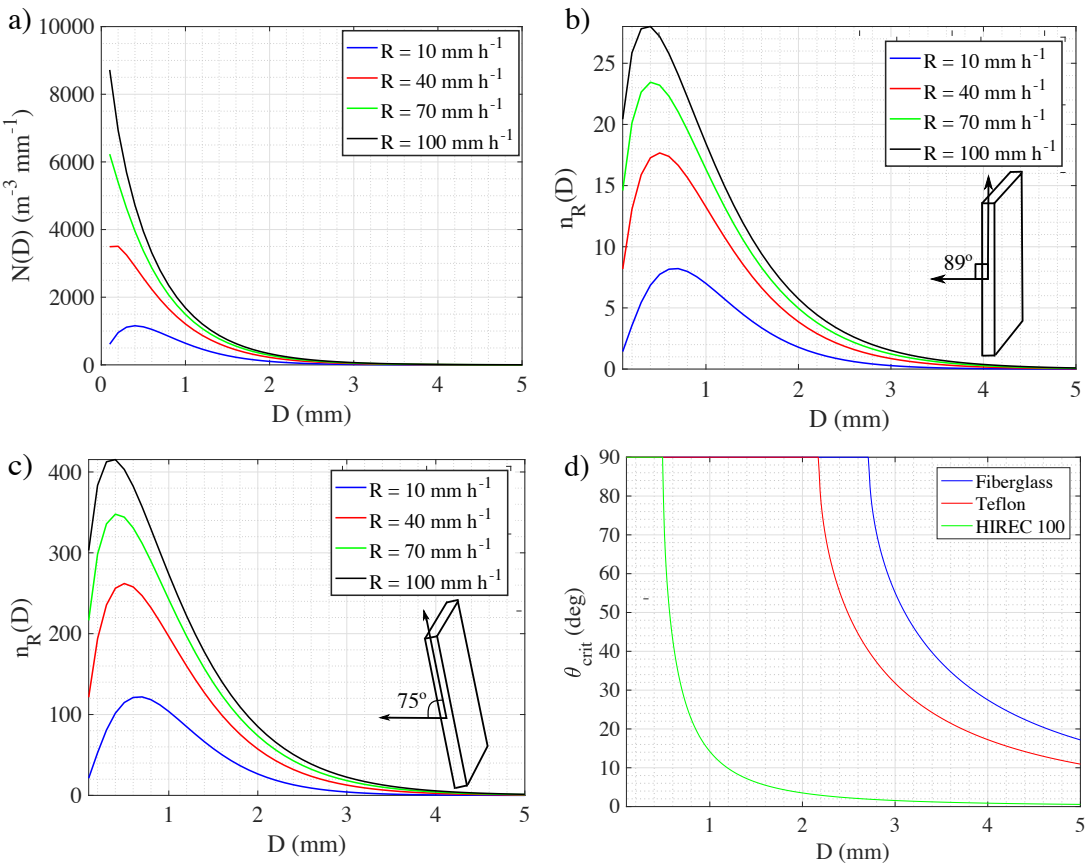

Figure 4.8: a) The drop-size distribution computed at different rain rates. b), c) The number of droplets accumulated on a 10.53×10.53 cm^2-surface for $T = 30$ s, evaluated for different rain rates, at $\theta_i = 89°$ and 75°, respectively. d) The computed critical angles for fiber-glass (hydrophilic), teflon (hydrophobic), and HIREC 100 (super-hydrophobic). The advancing and receding angles are 105° and 15° for fiber-glass, 120° and 79° for Teflon, and 151° and 144° for HIREC 100.

$$
\begin{aligned}
N(D) &= N_0 D^u \exp(-\Lambda D) \\
\Lambda &= 4.1 R^{-0.21} \\
N_0 &= 8 \cdot 10^3 \\
u &= -0.016\Lambda^2 + 1.213\Lambda - 1.957
\end{aligned}
\tag{4.27}
$$

where $N(D)$ is in m^{-3} mm^{-1}, D represents the drop diameter (mm), and R is the rain rate (mm h^{-1}). The DSD is plotted in Fig. 4.8a at different rain rates. To account for the droplet accumulation on a flat radome with unit surface area A_u (m^2), it is necessary to first compute the terminal velocity (m s^{-1}) of the droplets (Atlas and Ulbrich 1977; Zrnic and Doviak 2005) as:

$$v(D) = 386.6D^{0.67} \tag{4.28}$$

where in this case D is in meters. The total number of droplets accumulated, or droplet residual, per diameter class on a surface A_u (m^2), inclined of an angle θ_i with respect to the horizontal, computed for an observation time T (s), is given by Steiner and Smith (2000):

$$n_R(D) = N(D)A_u v(D)T\Delta D\cos\theta_i \tag{4.29}$$

where ΔD is the diameter interval (mm). The $\cos\theta_i$ term, is used to calculate the projection of A_u in the direction of the fall of the droplets at the inclination angle θ_i. The droplet residual on an area of $\lambda \times \lambda$ dimensions ($\lambda = 10.53$ cm at 2.85 GHz), for $T = 30$ s and $\Delta D = 0.1$ mm, is plotted in Fig. 4.8b and 4.8c for $\theta_i = 89°$ and $75°$, respectively. It was not possible to generate the plot that corresponds exactly to $90°$ of inclination because the cosine in Eq. 4.25 becomes zero. Therefore, instead of $90°$, $89°$ was chosen as a good approximation to evaluate $n_R(D)$. In this model, the breakup that occurs as a consequence of the droplet impacting the radome surface was not taken into account because of complexity added.

To create an accurate model, it is necessary to account for raindrops that fall off the radome surface at a specific inclination angle. Droplet removal occurs when the component of the gravity force parallel to the inclination plane defeats the surface tension at the interface of the water and the radome. Therefore, droplets with larger diameter will fall off the surface. The tilting angle at which a droplet with a given diameter starts moving is called critical angle (θ_{crit}). The critical angle, which depends on the hydrophobic properties of the surface, is evaluated by Nilsson and Rothstein (2012):

$$\theta_{crit} = \arcsin \frac{(k^{-1})^2 \sin(\pi - \theta)(\cos\theta_R - \cos\theta_A)}{4/3\pi r^2} \tag{4.30}$$

In Eq. 4.30, k^{-1} is the capillary length of water (2.7 mm), θ_A and θ_R are the advancing and receding angles, $\theta = (\theta_A + \theta_R)/2$, and r is the radius of the droplet. θ_A and θ_R depend on the hydrophobicity of the raincoat of the radome. The smaller the difference between θ_A and θ_R (hysteresis angle), the more hydrophobic the surface. From Eq. 4.30, it is immediately obvious that the bigger the droplet, the smaller the angle of inclination required to make the droplet fall. A comparison of critical angles for different materials is shown in Fig. 4.8d. In Fig. 4.9, water droplets in contact to a flat hydrophobic surface (teflon) are shown. In Fig. 4.9a, the surface is not inclined, therefore, the droplet is in a steady position. The contact angle (θ) and the surface tensions are also indicated. In Fig. 4.9b, a droplet falling off a plane inclined at θ_i is shown.

The surface roughness of the radome can affect the dynamics of the droplet on the radome. This factor is accounted for in the surface-liquid tensions term (Fig.

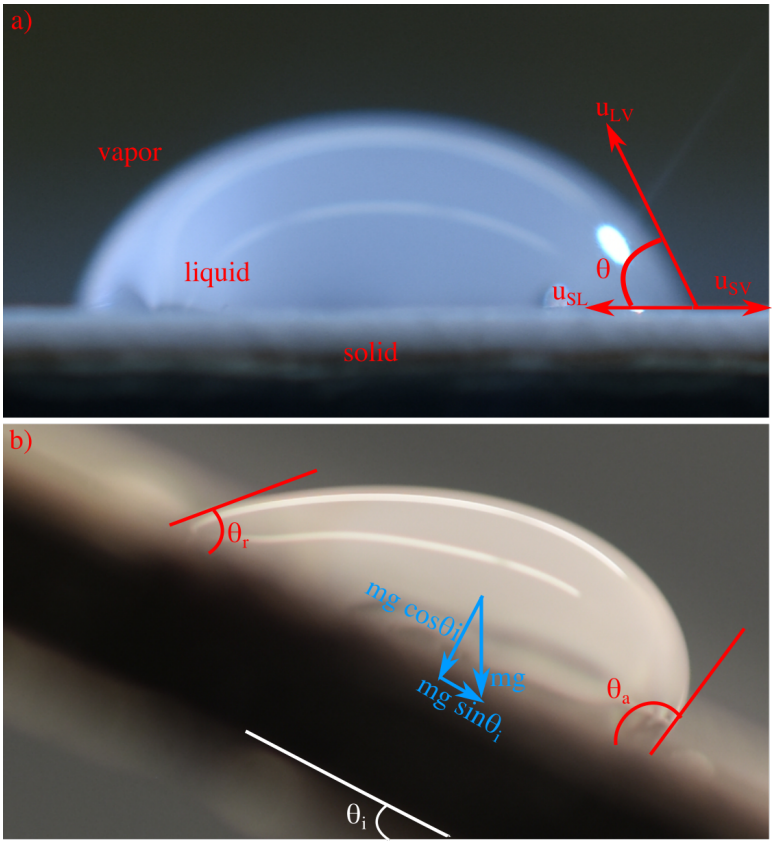

Figure 4.9: Photographs of droplets on a flat teflon surface. a) Non-inclined plane. b) Plane inclined at an angle equal to θ_i.

4.9a). u_{SL} is larger when the surface is rough than when it is smooth. The surface roughness does not affect the performance of a dry radome, because irregularities of the surface are too small compared to the wavelength for cases considered in this work.

To complete the analytical model, the final step is to estimate the attenuation due to droplet residual (n_R) accumulated on the flat square radome. To account for this, a simulation was developed to randomly place these residual droplets on a lattice that represents the radome surface of dimensions $\lambda \times \lambda$ (where $\lambda = 10.53$ cm). The lattice resolution was 0.05 mm. Because two droplets could be placed to overlap each other, and because it is necessary to account for the droplet removal

at a specific critical angle, the simulation replaces two droplets that intersect with one equivalent droplet. The equivalent droplet has a volume that is the sum of the volumes of the two overlapping droplets. The diameter of the equivalent droplet is computed from the equivalent volume. Then, if the corresponding diameter is too large (Fig. 4.8d), the droplet is removed, because it would fall off. This process is repeated until the total number of droplets accumulated (Eq. 4.29) is placed in the lattice.

To estimate the attenuation due to the layer of droplets on the radome, the Maxwell-Garnett's concept was used. This technique allows to model a material containing spherical inclosure with dielectric constant different than the enclosing medium, to an equivalent material. The equivalent material is now homogeneous and its dielectric constant is obtained by combining the dielectric properties of the outer material and the spheres located inside. The dielectric constant so obtained is called an effective dielectric constant (ϵ_{eff}) and it is computed as in Sihvola (2000):

$$\epsilon_{eff} = \epsilon_e + \frac{3\delta_i \epsilon_e(\epsilon_i - \epsilon_e)}{\epsilon_i + 2\epsilon_e - \delta_i(\epsilon_i - \epsilon_e)} \tag{4.31}$$

In Eq. 4.31, ϵ_e is the dielectric constant of the enclosure (air), ϵ_i is the dielectric constant of the enclosed sphere (water), and δ_i is the fractional volume. δ_i was calculated as the ratio between the total volume of water and the rectangular air volume that encloses the droplets. A graphical representation of this concept is shown in Fig. 4.10. In Fig. 4.10a, the real scenario is depicted. In Fig. 4.10b, the equivalent homogeneous material transformed by using Eq. 4.31 is presented.

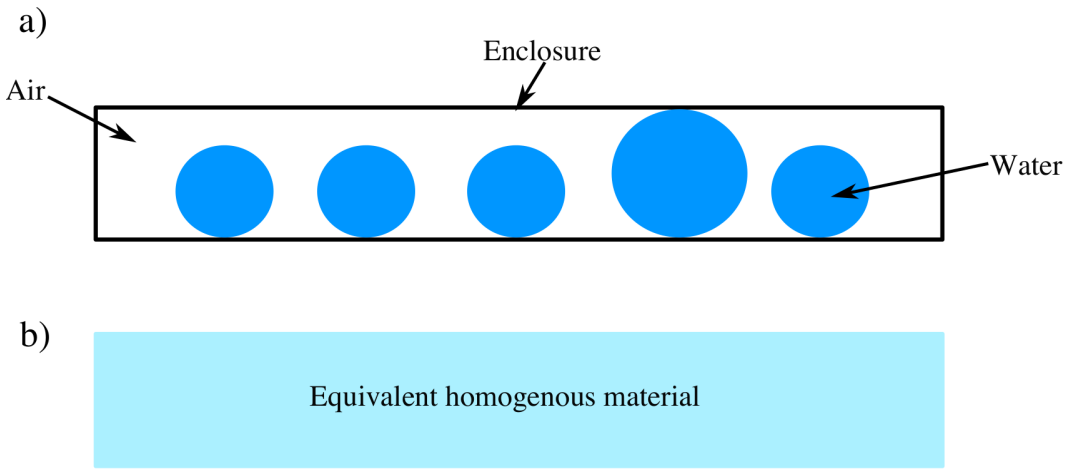

Figure 4.10: A graphical representation of the Maxwell-Garnett's concept. a) The real scenario showing water spheres enclosed in a rectangular air box. b) The equivalent homogenous material with dielectric constant ϵ_{eff} (Eq. 4.31).

4.3.1 S-band Study

A numerical simulation was performed to compute the reflectance and transmittance of the layer obtained by combining air and droplets with dielectric constant ϵ_{eff}. The reason for modeling the layer of droplets with an equivalent material of laminar shape with dielectric constant ϵ_{eff}, is to reduce the simulation time, without affecting the results accuracy. An example of operation of this simulation for R = 10, 100, and 200 mm h^{-1}, $\theta_i = 75°$, ΔD = 0.5 mm, and considering Teflon as a raincoat (Fig. 4.8d), was performed for a flat radome sample in S- and X-bands. The S-band case employs a λ x λ flat radome (λ = 10.53 cm at 2.85 GHz). The resulting droplet placement is presented in Fig. 4.11 for the observation times of 1 - 5 mins. The effective dielectric constants (ϵ_{eff}) computed by using Eq. 4.31 for the cases shown in Fig. 4.11, are listed in Table 4.1. As noticed from the table, the effective dielectric constant is very close to the one of air, because droplets do not fully occupy the rectangular volume that encloses them. It can also be noticed that for higher rain

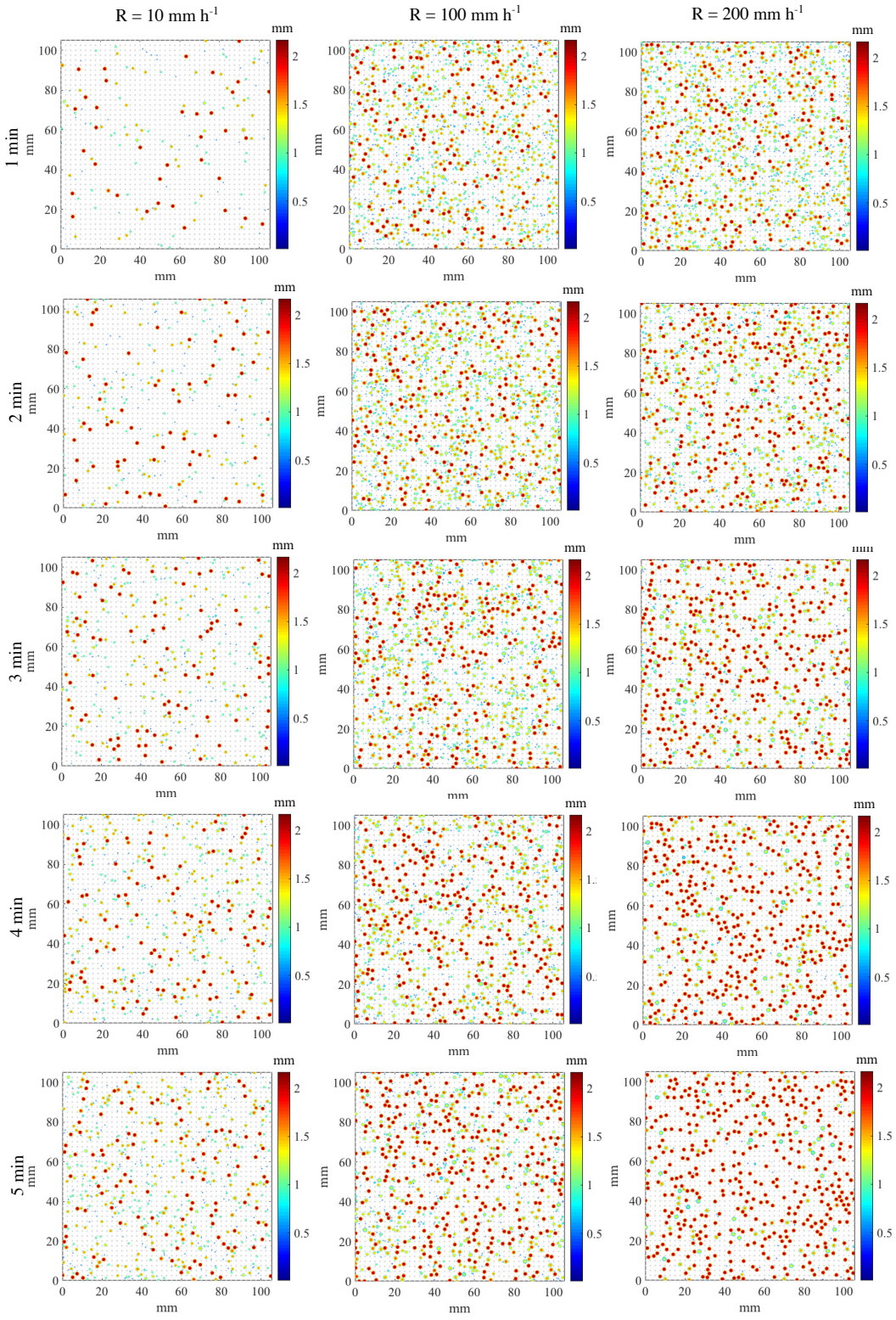

Figure 4.11: A comparison of droplets accumulated on a flat S-band radome unit cell with dimensions $\lambda \times \lambda$ ($\lambda = 10.53$ cm at 2.85 GHz) at $\theta_i = 75°$, for $R = 10$, 100, and 200 mm h^{-1}, for $T = 1$ - 5 min.

Table 4.1: The effective dielectric constant (ϵ_{eff}) calculated for the S-band scenarios presented in Fig. 4.11.

T	$R = \mathbf{10\ mm\ h^{-1}}$	$R = \mathbf{100\ mm\ h^{-1}}$	$R = \mathbf{200\ mm\ h^{-1}}$
1 min	1.04 - j0.000003	1.28 - j0.000027	1.35 - j0.000035
2 min	1.07 - j0.000006	1.36 - j0.000035	1.35 - j0.000034
3 min	1.10 - j0.000009	1.35 - j0.000034	1.34 - j0.000033
4 min	1.13 - j0.000012	1.33 - j0.000033	1.34 - j0.000034
5 min	1.16 - j0.000014	1.35 - j0.000034	1.35 - j0.000034

rates, by increasing the observation times, the effective dielectric constant does not increase, but it seems to reach a maximum value. This can be explained by the fact that the radome saturates and it cannot host more droplets. The higher the rain rate, the faster the radome saturates. For $R = 10$ mm h^{-1}, it takes longer than 5 minutes for the radome to become saturated, while for $R = 200$ mm h^{-1}, 1 minute is enough to fill the radome with droplets. It is important to remember that the droplets placement is random and therefore, the effective dielectric constant is computed as a result of a random process. Based on this consideration, by running a simulation twice for a given rain rate and observation time, two slightly different ϵ_{eff} can be calculated.

Numerical results of the scenarios presented in Fig. 4.11, with the computed effective dielectric constants listed in Table 4.1, are shown in Fig. 4.12. By increasing the amount of droplets accumulated, either because the rain rate is higher or because the observation time is longer (or both), the effective dielectric constant of the equivalent Maxwell-Garnett layer increases as discussed. In Fig. 4.12a, the reflectance is shown. The reflection coefficient rises as the effective dielectric constant becomes larger. An increase of 5 dB is noticed for the reflectance from the dry case to the wet scenario for $R = 10$ mm h^{-1} and $T = 9$ min. The transmittance is

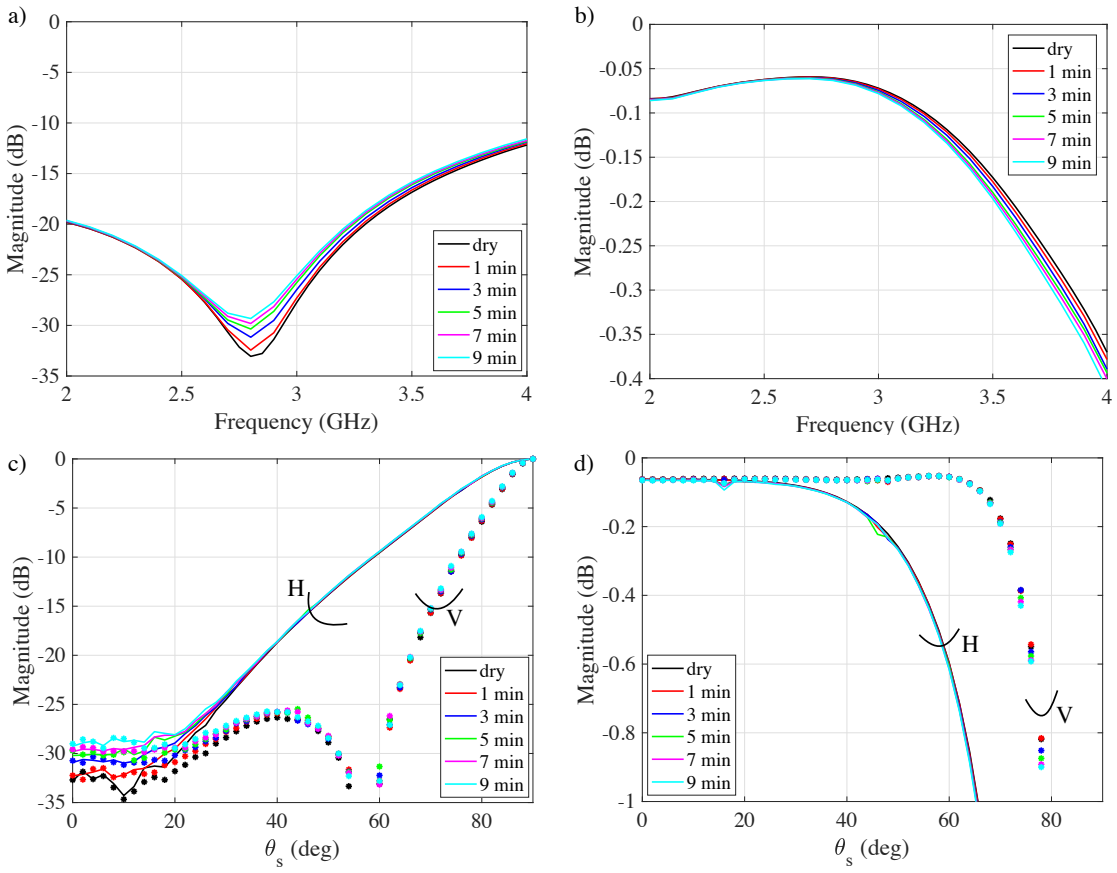

Figure 4.12: Numerical results obtained for the S-band scenarios presented in Fig. 4.11. The radome stackup is listed in Table 3.1. a) and b) Reflectance and transmittance as a function of the frequency. c) and d) Reflectance and transmittance as a function of the steering angle.

plotted in Fig. 4.12b. At 2.85 GHz, the transmission coefficient does not show an appreciable difference, however, the attenuation increases with the frequency. The reflectance and transmittance as a function of the steering angle are plotted in Fig. 4.12c and 4.12d. Both reflectance and attenuation increase with the the steering angle, as expected.

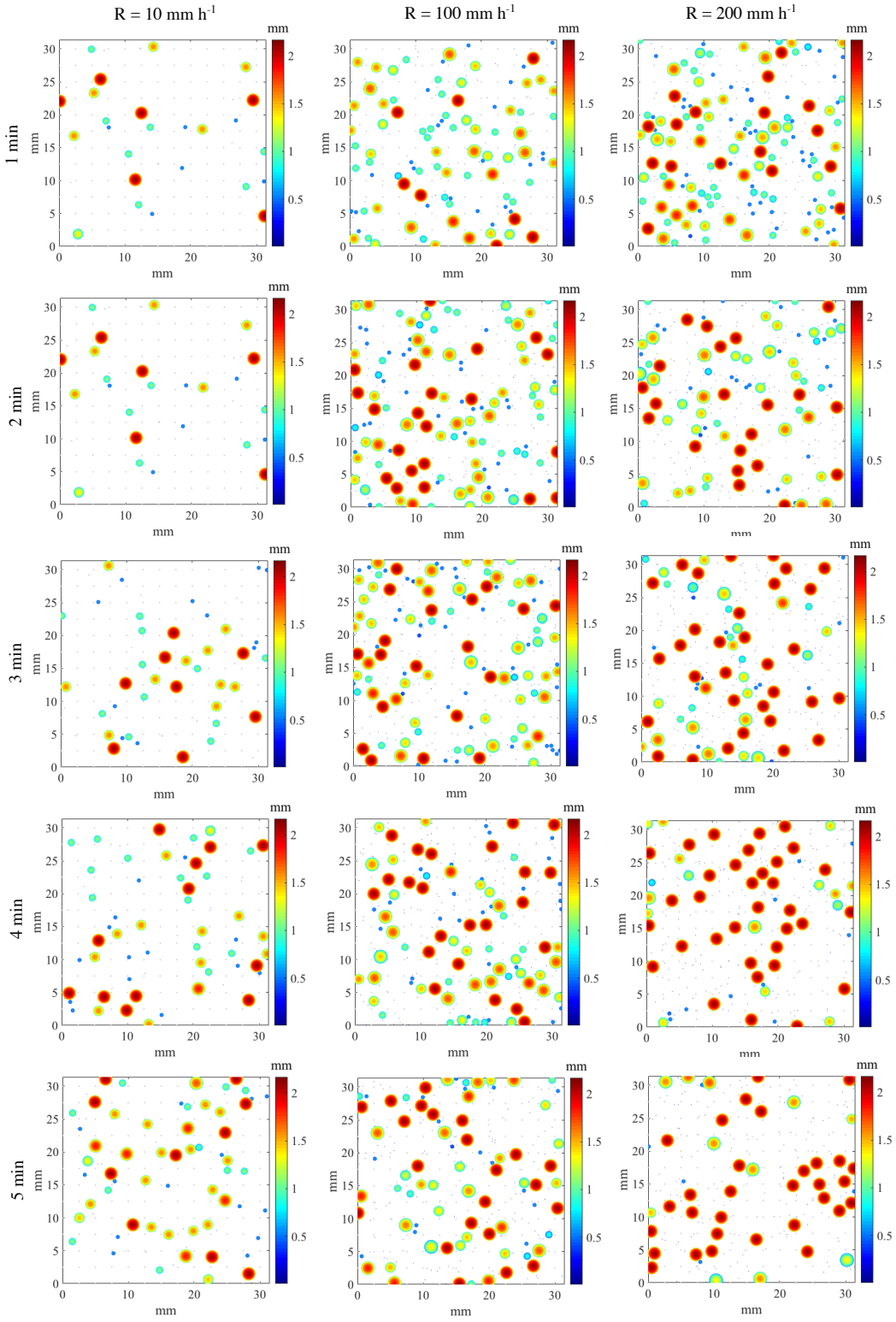

Figure 4.13: A comparison of droplets accumulated on an X-band radome unit cell with dimensions $\lambda \times \lambda$ ($\lambda = 3.14$ cm at 9.55 GHz) at $\theta_i = 75°$, for $R = 10$, 100, and 200 mm h^{-1}, for $T = 1$ - 5 min.

Table 4.2: The effective dielectric constant (ϵ_{eff}) calculated for the X-band scenarios presented in Fig. 4.13.

T	R = **10 mm h^{-1}**	R = **100 mm h^{-1}**	R = **200 mm h^{-1}**
1 min	1.03 - j0.000003	1.24 - j0.000023	1.35 - j0.000034
2 min	1.07 - j0.000061	1.38 - j0.000038	1.31 - j0.000030
3 min	1.10 - j0.000060	1.39 - j0.000038	1.34 - j0.000033
4 min	1.15 - j0.000013	1.36 - j0.000035	1.34 - j0.000033
5 min	1.18 - j0.000017	1.34 - j0.000033	1.37 - j0.000036

4.3.2 X-band Study

The X-band scenario is plotted in Fig. 4.13 for the same conditions used for the S-band case. In the X-band scenario, the dimensions of the flat radome sample were λ x λ (λ = 3.14 cm at 9.55 GHz). In Table 4.2, the effective dielectric constants computed by using Eq. 4.31 are listed for the corresponding cases shown in Fig. 4.13.

In Fig. 4.14a and 4.14b, a comparison of the simulated reflectance and transmittance for observation times equal to 1 and 5 min, for the rain rates of 10, 100, and 200 mm h^{-1}, is shown for the X-band case. The same quantities are plotted in Fig. 4.14c and 4.14d as a function of the steering angle. As expected, the reflectance and attenuation are both higher for the X-band than for the S-band case.

4.4 Ice and Snow Formations

Ice and snow formations are not the focus of this dissertation, therefore they are not object of investigation. However, a short discussion is provided. It is possible to define an analytical model similar to the one created for water, to calculate the dielectric constant and tangent loss of ice and snow. Then, it will be necessary to

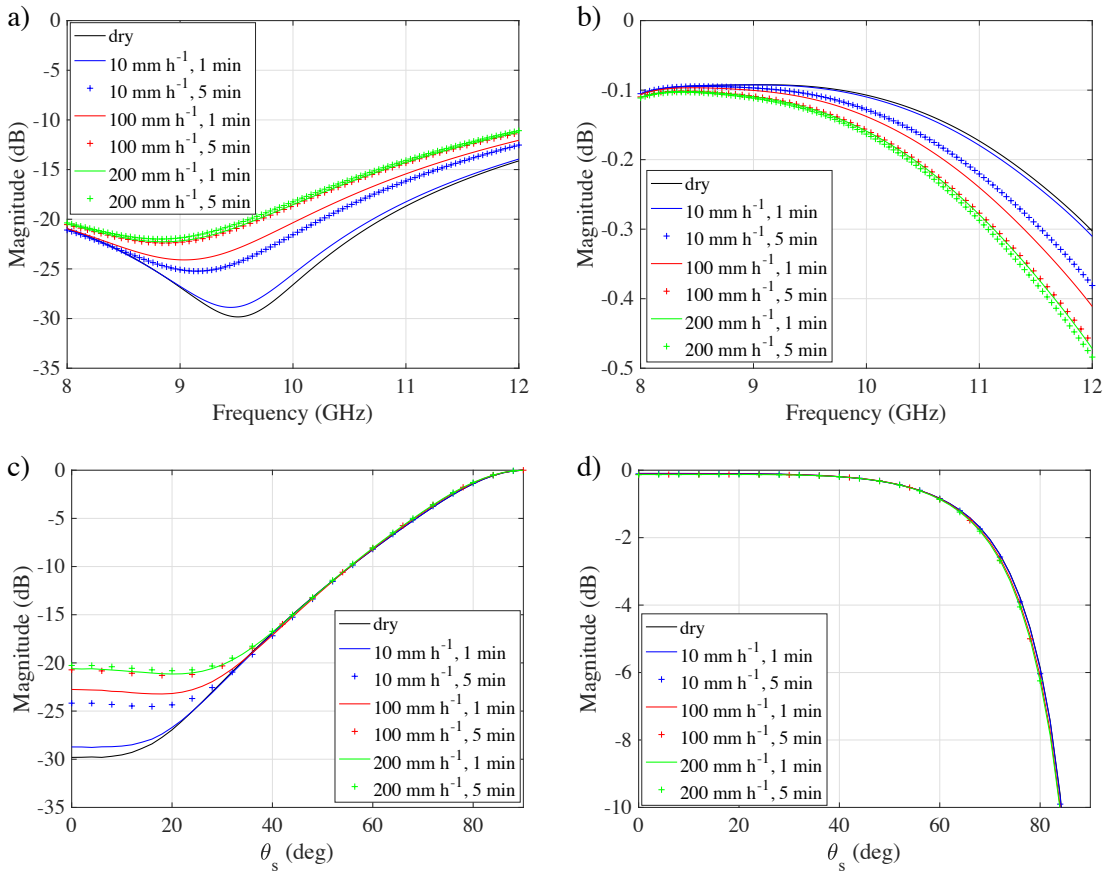

Figure 4.14: Numerical results obtained for the X-band scenarios presented in Fig. 4.13. a) and b) Reflectance and transmittance as a function of the frequency. c) and d) Reflectance and transmittance as a function of the steering angle.

find a relation between the snow rate and the thickness of the snow accumulated on the radome, as a function of the geometry of the radome. The same should be done for ice. Numerical simulations can be performed for various thicknesses of ice (or snow) to estimate reflectance and attenuation. The formulations to compute the thickness of snow as a function of the snow rate, or similarly, to estimate the thickness of the ice formed on the radome is not available in the literature. Ice can be formed because of the presence of water when the temperature is low enough. However, the freezing process is not immediate and water can fall off by the time that it becomes ice. Estimating how much water is actually transformed to ice is

Table 4.3: A comparison of the dielectric parameters of water, ice, and snow at X-band.

Content	ϵ_r	**tan**δ
Water	60	0.5
Ice	3.14	10^{-7}
Snow	2.1	0.2

hard to perform. In addition, ice is also formed through deposition or desublimation. Deposition is the process by which, in sub-freezing air, water vapor changes directly to ice without first becoming a liquid. This is how snow forms in clouds, as well as how frost and hoar frost form on the ground or other surfaces (USGS 2018). The estimation of the ice and snow thicknesses are left for future works.

The dielectric constant of ice is strongly dependent on temperature (Matsuoka et al. 1996), while the one of snow (Achammer and Denoth 1994) mostly depends on the liquid content and the density. In Table 4.3, a comparison of the dielectric constants and tangent loss of water, ice, and snow measured at X-band is presented.

4.5 Summary

This chapter provided the analytical formulations to compute the dielectric constant of water as a function of the frequency and temperature. It was shown that the real part of the dielectric constant decreases with the frequency and the rate of this changes depends on the temperature considered. For example, at 2 GHz, the real part of the dielectric constant is higher at lower temperatures, but this is not true at higher frequencies ($>$ 7 GHz) because the steepness of the curve is different at various temperatures. On the other hand, the imaginary part and tangent loss of

water both increase with frequency within the selected range analyzed. The lower is the temperature, the higher is the loss. The dynamic behavior of the real and imaginary parts of the dielectric constant as well as the tangent loss, is probably due to the relaxation time of the electric dipoles at a selected frequency and temperature of water.

The chapter also provided an analytical model to compute the reflectance, transmittance, and absorption of the water based on the type of water formations considered (film or droplets). In S-band, a rise of the reflectance of 25 dB from the dry case to the scenario considering a water thickness of 423.4 μm, was measured. This corresponds to an increase of attenuation of 4 dB when a 423.4 μm-film thickness is present. The same analysis was repeated in X-band. The results showed that the attenuation can reach 10.5 dB when water is present on the radome.

The last analysis was performed considering droplet formation on the radome. To execute this study the Maxwell-Garnett equation was used to simplify numerical simulations. The results showed that by increasing the rain rate, a shorter time is required to saturate the radome with droplets, and therefore, results do not show a decrease of the radome performance when saturated. It was shown that in S-band, for a 10 mm h^{-1}-rain rate, the reflectance increases from -33 dB for the dry case, to -29 dB for droplets accumulated during an observation time of 9 minutes. The transmittance does not show appreciable difference because absorption and reflectance are small for the droplet formation scenario. At X-band, for a rain rate of 10 mm h^{-1}, the reflectance increases from -29 dB for the observation time of 1 minute, to -25 dB for the same rain rate and 5 minutes of observation time.

Analytical models to characterize the thicknesses of ice and snow accumulated on the radome are not available yet and they are left for future works.

Chapter 5

Proposed Radome Measurement Technique

This chapter discusses the two proposed techniques to characterize the effect of various water formations on the radome. The first approach discussed is called the single-probe technique. This procedure evaluates the performance of the radome in both wet and dry conditions based on the measurement of the reflection coefficient. Because the level of the reflections increases when water is added on the radome surface, it is possible to determine the performance degradation by measuring the folded reflectance generated from a radome including water. The important aspect of this proposed technique is that it allows real-time measurements while the radar is operating. It will be shown that the absorption occurring in the water layer can be estimated by a purposely developed algorithm and therefore, the attenuation of the wet radome can be estimated. The principle of operation of the single-probe technique, as well as the devices necessary to perform such a type of measurement is discussed in this chapter.

The second technique proposed consists in characterizing the impact water located on the radome, on the radiation pattern of a phase array antenna. To perform this study, an 8 x 2 S-band array for weather radar is employed. To evaluate the impact of various water formations on the radiation pattern of the mentioned antenna, water was placed on the internal radome of the antenna. Then, the near-field

radiation pattern is measured in near-field chamber. The results proposed later in this chapter show how the SLL, cross-polarization and main beam are affected by water.

5.1 Conventional Method: Two-Probe Technique

The traditional system used to measure attenuation in a radome is called two-probe technique and it is shown in Fig. 5.1. For this technique, two probes are necessary, one for transmit and the other for receive. Both antennas have to be perfectly aligned facing each other, with the sample material located exactly halfway between the probes. Based on this configuration, part of the incident field at the air-radome interface is reflected, and part is transmitted through the sample material. Although this technique provides excellent results, it is impractical for radome characterization in operational radar systems. This procedure, in fact, requires the use of a two-port network analyzer to measure the electric field that is reflected and transmitted through the radome sample. Additional limitations of this technique are the facts that is bulky and that it can only characterize samples of flat radomes, whereas most radomes employed in operational radar systems are of different shapes (bullet, spherical, conical, etc).

In the following section, the new technique to characterize the radome performance is presented and discussed. In addition, numerical simulations are performed on dry radome to validate the new method.

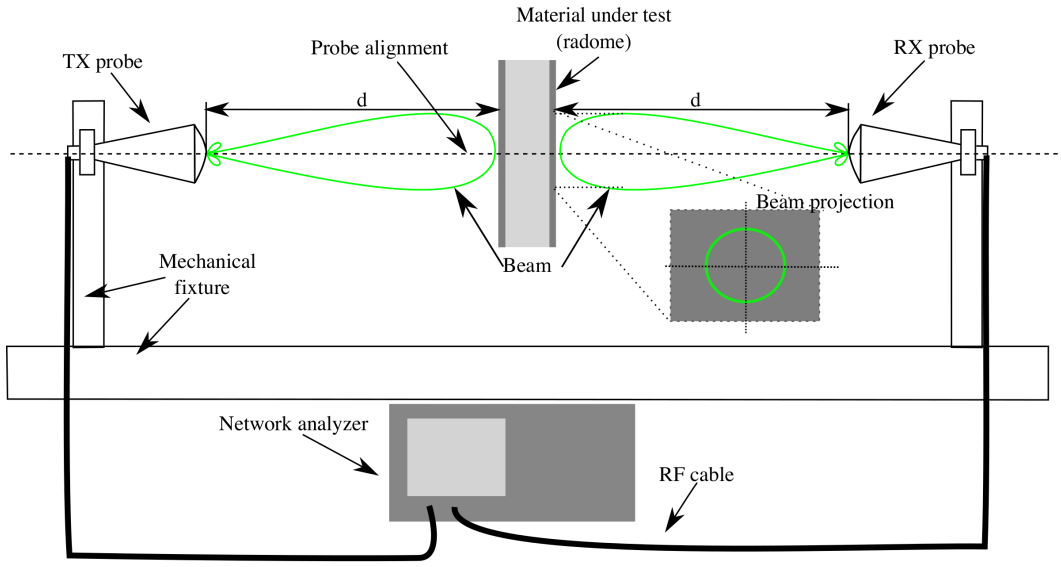

Figure 5.1: A schematic representation of the conventional two-probe method to characterize the radome performance, including the network analyzer and mechanical fixture.

5.2 Proposed Method: Single-Probe Technique

The conventional two-probe method allows to account for reflections and attenuation of the radome under test. However, the system is bulky, expensive, it does not allow to characterize radomes in real-time, and it can be only used for flat radome samples. To overcome these drawbacks, a different solution was developed. The proposed technique is called one-probe method and it is presented in Fig. 5.2. This method characterizes the performance of the radome based on the reflection measurement. The system requires a single-port reflectometer connected to the probe to measure the reflections generated at the air-radome interface. Because a multilayer radome is usually employed for practical applications, the reflectometer measures the "folded" reflectance. The folded reflectance is a combination of all the reflections occurring inside the multilayer material. To better measure the reflectance generated by the

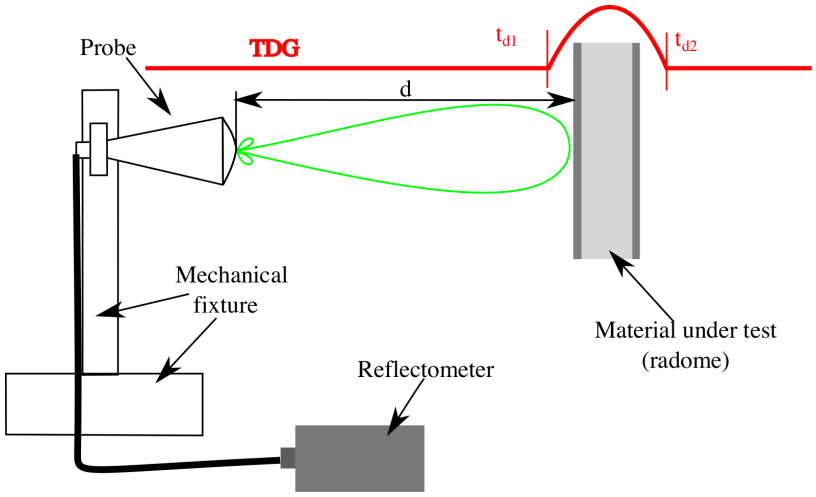

Figure 5.2: A schematic representation of the novel method to characterize the radome performance using a single probe.

radome, it is necessary to filter out all the unwanted reflections produced by the multi-path of the signal. This goal is achieved by operating the reflectometer in the time domain and setting the Time Domain Gating (TDG) according to the distance between the probe and the reflectometer. By using TDG, all the unwanted reflections can be eliminated and only the reflectance produced by the multilayer radome is measured. As later will be shown, the application of the filter in the time domain noticeably improves the data quality.

The advantage of using this technique is that it is practical for in-field operations with operative radomes. Because the reflectometer is small and only one antenna is needed, the mechanical fixture requirements can be relaxed. For comparison, in the two-port system, because of the necessary alignment accuracy between the two probes, the mechanical setup is more complex and bulky.

To better evaluate the performance of the radome, the probe employed for the measurement should have a narrow beamwidth. A narrow beam results in high

spatial resolution and therefore, any imperfection or damage, if presents inside the radome, can be detected. Flaws or damages of the radome can occur during both the fabrication and assembly processes and they can affect the performance of a dual-polarized radar signal because of their geometry. Flaws and damages can be in various form, but in cases where their geometry is more pronounced in the horizontal or vertical plane, the attenuation generated by the imperfection is not the same in the two planes. This factor is critical for the radar performance and it is necessary to account for these imperfections in the radome. In this dissertation a dielectric rod antenna was employed as a probe to perform analysis with the one-probe method. This type of antenna matches the requirements discussed.

An example of an application of the one-port system for real-time operation is shown in Fig. 5.3. In the figure, a dielectric rod antenna was employed as a probe. The single port reflectometer, set in time domain, reads the reflections directly measured by the probe. By mounting the probe at the antenna feed position, scans in azimuth and elevation with resolution dictated by the radar system, are possible. This configuration allows full real-time RF characterization of the radome. A probe smaller than the antenna feed is required to minimize the attenuation due to potential blockage. This requirement is necessary to measure the radome reflections without affecting the radar performance. A customized probe with a small transversal area and narrow beam for high spatial resolution tests, is required. The probe collects reflections generated from the radome in the same direction that the radar is scanning, because it is mounted in the radar antenna. Although mounted on the radar antenna, the operation principle of the radome characterization device

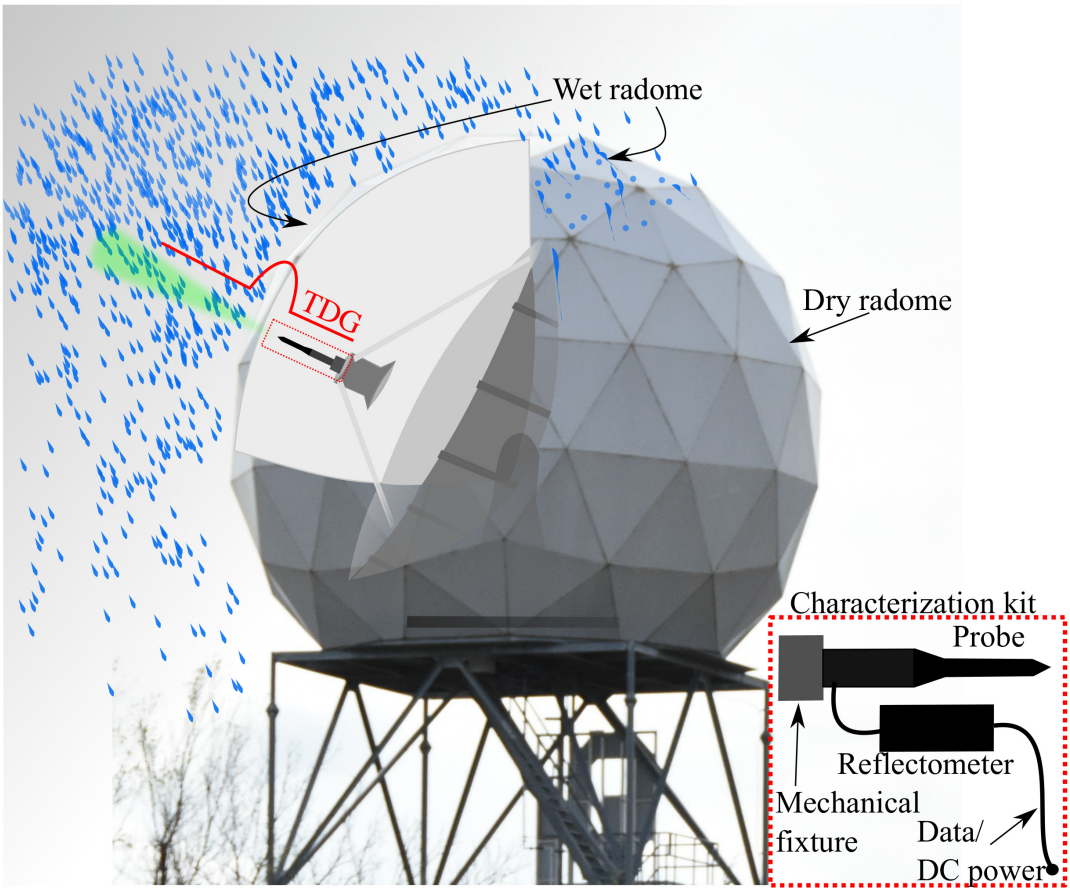

Figure 5.3: A schematic representation of the novel method to characterize a radome performance using a single probe employed for real-time assessment in an operational radar.

is totally independent on the radar, and it does not affect the radar operating bandwidth. The proposed method allows to measure the effect of water on the radome outer surface when rain reaches the radar location. Water accumulation is not the same on all the parts of the radome. Multiple factors, including dirt on or damage to the radome and blowing wind can influence water distribution on the surface.

The probe is connected to the single-port reflectometer, and the TDG is set to measure the reflectance at the radome interface by filtering out all the multiple

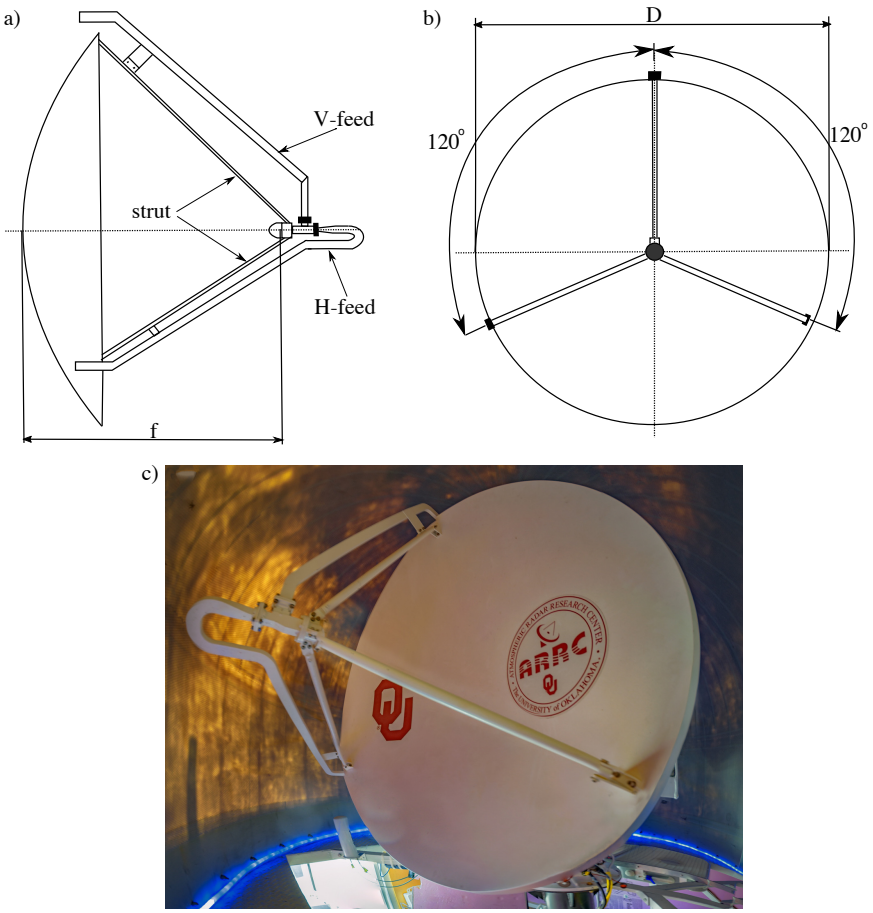

Figure 5.4: An illustration of the X-band PX-1000 radar antenna showing the feed and the struts arrangement, the focal distance (f, 18 in), and the diameter of the parabolic reflector (D, 48 in). a) The side view. b) The front view showing the struts only. c) A photograph of the parabolic reflector (Photo taken by Arturo Yoshiyuki Umeyama).

reflections coming from the surrounding environment. The low size of the instrument, composed of a probe and reflectometer, allows ease of transport for infield measurements in the case of mobile radar stations, and quick implementation in existing operational radars. To simultaneously measure the reflections generated by the radome in the H- and V-polarizations, a dual-polarized probe can be suitably designed or two linearly-polarized probes used where one is 90°-rotated respect to the other one. The influence of a dual-polarized probe on the performance of a

Table 5.1: A comparison between the measured and simulated antenna performance of the PX-1000 at 9.55 GHz.

Parameter	**Measured**	**Simulated**
Gain (dB)	39.3	39.7
Beamwidth (°)	1.8	1.8
SLL (dB)	-26	-34.6

parabolic reflector antenna was estimated through simulations in Ansys HFSS. To evaluate the impact of the instrument on an operational radar, two scenarios were considered. The first case simulated the reflector system of the PX-1000 weather radar (Cheong et al. 2013) with no radome included and without the dielectric probes. Two dielectric antennas were then added for a second simulation, placed right behind the feed of the reflector system, to evaluate their effect on the radiation pattern. An illustration and a photograph of the PX-1000 parabolic reflector are shown in Fig. 5.4. The measured performance of the PX-1000 radar was executed in an outdoor far-field test range by the manufacturer. Unfortunately, a copy of these measurements is not available, but only information such as gain, beamwidth, and the levels of sidelobes are provided.

A comparison between the measured and simulated performance of the parabolic reflector is listed in Table 5.1. The gain and beamwidth achieved through simulation is the same as the one measured in actual performance, but in the simulation, a lower sidelobe level is obtained. The discrepancy between the measured and simulated sidelobe level is probably due to the fact that, since the measurement was done outdoors, multiple reflections have raised the level of the sidelobes, while this does not occur in the simulation. Since the model created well represents the actual radar antenna, both in terms of physical dimensions and in terms of electrical performance,

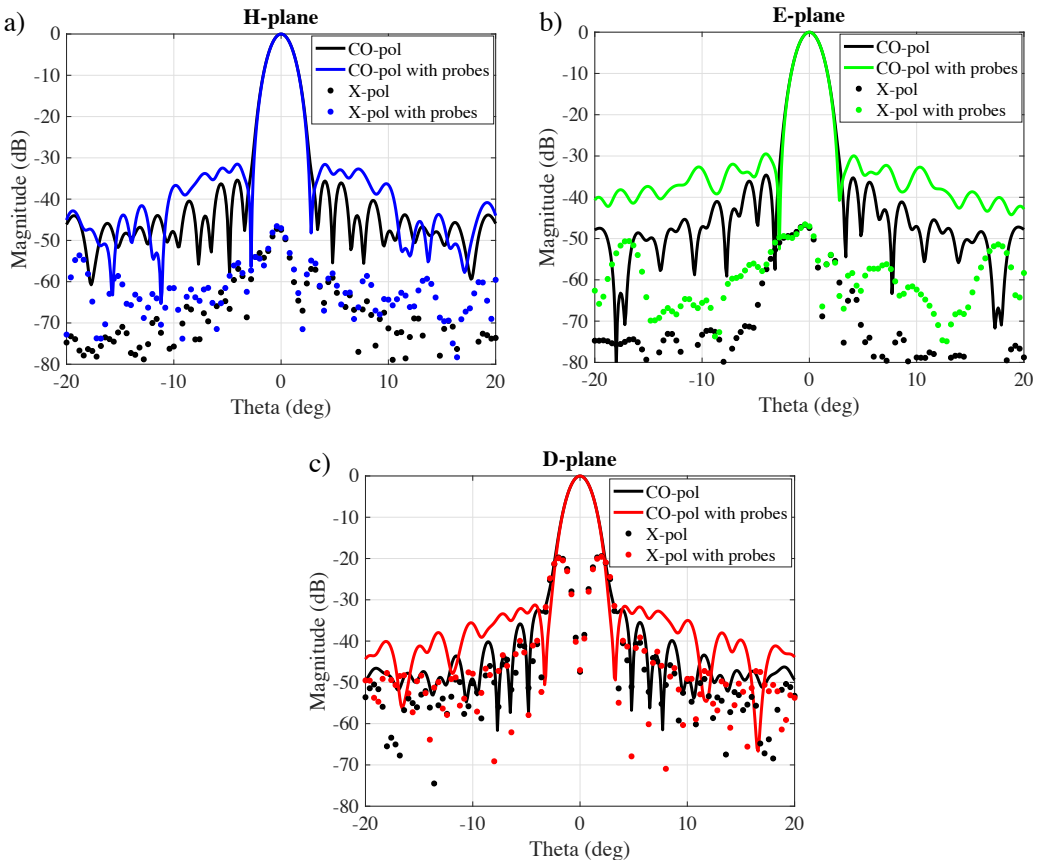

Figure 5.5: The effect of a dual-polarized probe in the far-field radiation pattern of the X-band reflector used in the PX-1000 radar. Results based on numerical simulation. a) The H-plane. b) The E-plane. c) The D-plane.

the effect of the probes can be now evaluated. The results regarding the influence of the dual-polarized probe on the parabolic reflector performance are presented in Fig. 5.5. Simulations show that the gain is not affected by the presence of the probe, while a rise of the secondary beams is noticeable. The level of the cross-polarization, in the -5° to 5° range, remains the same (Mancini et al. 2017), but at other elevation angles it increases due to the probe presence. The E-plane is more affected by the presence of the dual-polarized probe than the other principal planes. This is probably because the dielectric antennas are aligned in the corresponding direction, presenting a larger obstruction than in the H-plane. Although the impact

on the radar performance was evaluated by using a dual-polarized probe, while in the experiments a single-polarized probe was employed, this result is important for validating the proposed technique. Furthermore, by using two probes instead than one, it creates a worst-case scenario with respect to the case where only a single probe was used. Considering the impact of the probe on the radiation pattern of the parabolic reflector, a miniaturized version of the dielectric antenna will be necessary for real-time applications, in order to further reduce its impact on the radar performance.

The probe does not need to sample the radome every time the radar transmits/receives. It is sufficient to take a sample every N times the radar samples. If, for instance, the radar samples N times consecutively, at the $N+1$ transmitting period, the probe samples instead of the radar. The echoes from the radar would be very low in this circumstance, and would not interfere with the probe. Sacrificing one sample every N samples of the radar, would not affect the measurement of the weather measurements. In practice N is about 100. In this way, the probe can sample at the same frequency the radar operates without interference from the radar (Irazoqui and Fulton 2018). To relate the data collected to the actual position, synchronization will be required. In this way, it is possible to have information about the radome conditions at the same time and in the same position where the radar is scanning.

In general, the radome performance is characterized in terms of attenuation. The single-probe method is based on the measurement of the reflection coefficient generated by the air-radome interface, and therefore, it cannot provide information

about the attenuation. However, an algorithm to estimate the attenuation produced by a wet radome was developed by the author and it is explained in the next section. It is anticipated that the method can be applied both to laminar flow and droplet distribution of water on the radome.

5.2.1 Correction Algorithm

This section describes the procedure to estimate the transmittance that occurs through a wet radome based on the fact that the reflectance is directly measured (reflectometer) and that the absorptance can be calculated. Such an algorithm will be applied to estimate the attenuation through an operative radome. By this assumption, it follows that Eq. 4.22 can be rewritten as:

$$T_{r+w}^{true} = 1 - R_{r+w} - A_{r+w} \tag{5.1}$$

where the subscript means "radome + water", to indicate a wet radome. Eq. 5.1 represents the exact (true) solution to evaluate the transmittance, if reflectance and absorptance are known. The proposed technique employs a reflectometer, which means that the reflection coefficient is always known. This is not true for the absorption in cases when it occurs. To overcome this drawback, an approximation that requires the absorptance to be evaluated separately is necessary. Since the absorption is mostly due to the presence of water over the radome, as droplets/rivulets or water film formation, Eq. 5.1 is rewritten in its approximate form as:

$$T_{r+w}^{est} \approx 1 - R_{r+w} - A_w \tag{5.2}$$

In Eq. 5.2, the superscript "est" stands for estimated, while the term A_w is the computed absorptance due only to the water without radome. Eq. 5.2 can be employed instead of Eq. 5.1 when the radome absorption is small, or when the radome stackup is unknown. If the radome stackup is not known, the related absorption cannot be computed. It is important to note that the attenuation is different from the absorption. Attenuation is quantified by the transmission loss ($TL = 1/T$), which represents what is not transmitted, both because the signal is absorbed and because part of it is also reflected. If a sample of flat radome is available, the absorption can be measured by using the technique shown in Fig. 5.1. However, it is rare that a separate sample of the same radome material actually employed in the radar is available, thus in this work the radome stackup is assumed to be unknown. The following algorithm allows the estimation of the transmittance through a wet radome by ignoring the absorption occurring inside the radome itself. It is shown that if the absorption generated in the water layer is dominant with respect to the one produced inside the radome, the algorithm produces accurate results. This procedure is described below for cases when water distributes as a film or as droplets.

5.2.1.1 Water Film Formation

When water distributes as a film, the thickness of the slab depends on the rain rate (R). For a spherical radome, the thickness is given by Eq. 4.26 (Gibble 1964). Once the thickness is calculated, the reflectance and transmittance through a slab of water can be computed by using Eqs. 4.16 and 4.17. Then by reordering Eq.

Table 5.2: The water film thicknesses calculated for different rain rates. In the third column is shown the maximum relative error (Δ_{max}) between the true value of transmittance, simulated in HFSS, and the approximated value computed by Eq. 5.2 in the frequency band considered. In the fourth column, the relative error (Δ) calculated at 9.55 GHz is shown. In the last two columns, a comparison of the attenuation found in the current study with Frasier et al. (2013) is presented.

R (**mm h^{-1}**)	**Thickness** (μ**m**)	Δ_{max} (%)	Δ (%) **at 9.55 GHz**	**Mancini (dB)**	**Frasier (2013) (dB)**
5.3	63	4.4	0.72	2.15	1.7
20	98.06	3.59	0.03	3.3	2.5
40	123.5	3.78	0.51	4.1	3.1
60	141.4	4.07	0.83	4.6	3.5
120	178.2	4.56	1.32	5.6	4.4
200	211.3	4.81	1.62	6.5	5.2

4.22 for A, the absorptance can be found. The absorption derived is the term A_w to employ in Eq. 5.2. Since the reflectance for the "radome + water" film stackup (or wet radome) was directly measured by the reflectometer, and the absorption of the water film (no radome) is known for a specific rain rate, the transmittance through the wet radome can be estimated by using Eq. 5.2.

To validate this algorithm, simulations in HFSS were performed. The X-band PX-1000 radome (Table 3.3) was used for the simulation. The water thickness was computed for a radius equal to 1.1 m by using Eq. 4.26. In Table 5.2, the thicknesses calculated at different rain rates are shown. First, a simulation of this radome was performed by adding a layer of water at 20 °C. In this way, the true value of transmittance (T_{r+w}^{true}) was identified for the purpose of comparison. Second, using Eqs. 4.16 and 4.17, the reflectance (R_w) and transmittance (T_w) through a slab of water without the radome were computed analytically. Then, the absorption (A_w) is calculated by reordering Eq. 4.22. Finally, the transmittance of the wet radome (T_{r+w}^{est}) is estimated by Eq. 5.2. In Fig. 5.6, the comparison between

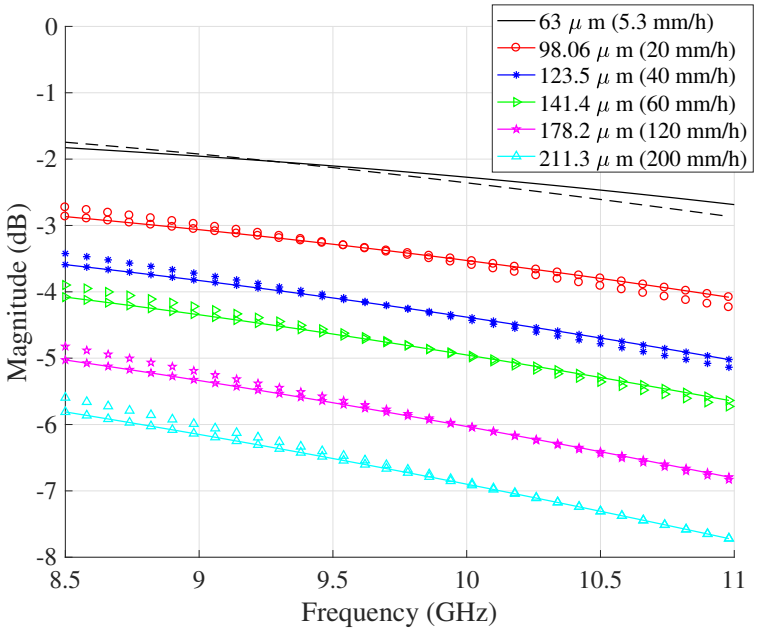

Figure 5.6: Shown is the comparison between the true (dashed line) and estimated (continuous line) transmittances for different water film thicknesses. In the legend, in parentheses, are also shown the equivalent rain rates for each thickness.

T_{r+w}^{true} and T_{r+w}^{est} is shown for different water layer thicknesses. In the third column of Table 5..2, the maximum relative error of the transmittance is presented. The relative error is computed as the absolute value of the difference between T_{r+w}^{true} and T_{r+w}^{est}, normalized with respect to T_{r+w}^{true}. The maximum relative error occurs at different frequency points for the various thicknesses in the band 8.5 - 11 GHz. For all the cases, the error is below 5 %, demonstrating that the approximation does not introduce a large bias in the computation of the transmittance for film formation. This is because the absorption of the dry radome is low. In the fourth column of the table, the relative error at the frequency at which the radome was designed, 9.55 GHz, is presented.

In the last two columns a comparison of the true value of the attenuation $(1/T_{r+w}^{true})$ obtained in this study, and the one computed by Frasier et al. (2013)

is shown. Two results can be observed. First, the attenuation obtained in this work overestimates the one computed using Frasier et al. (2013). Second, the difference between the attenuation level increases as the rain rate increases. The discrepancy between the two studies depends on the radome stackup employed, the radome conditions (not mentioned in Frasier et al. (2013)), and considerations about the water temperature (Fig. 4.2). In addition, in Fig. 6 of Frasier et al. (2013), it is shown that the attenuation computed underestimates the other studies used as purpose of comparison. Regarding the second observation, Frasier's formula was found to fit Marshall-Palmer and WSR-88D up to a rain rate of 20 mm h^{-1} (Frasier et al. 2013). At higher rain rates, the equation employed by Frasier et al. (2013) might need adjustment of the parameters.

5.2.1.2 Water Droplet Formation

The correction algorithm applied to estimate the transmittance for film formation, is repeated considering droplets accumulated on the radome. The rain rates employed for this study are 10, 100, and 200 mm h^{-1} for the observation time of 1 minute. The corresponding dielectric constants of the equivalent medium computed with Eq. 4.31, are listed in Table 4.2. The thickness of the equivalent air-water mixture is 2.1 mm.

A comparison between T_{r+w}^{true} and T_{r+w}^{est} for the droplet scenario is shown in Fig. 5.7. For this scenario, the algorithm generates a large error to estimate the attenuation of a wet radome. This mismatch happens because the absorption occurring in the water layer (droplets) is comparable to the one occurring inside the radome.

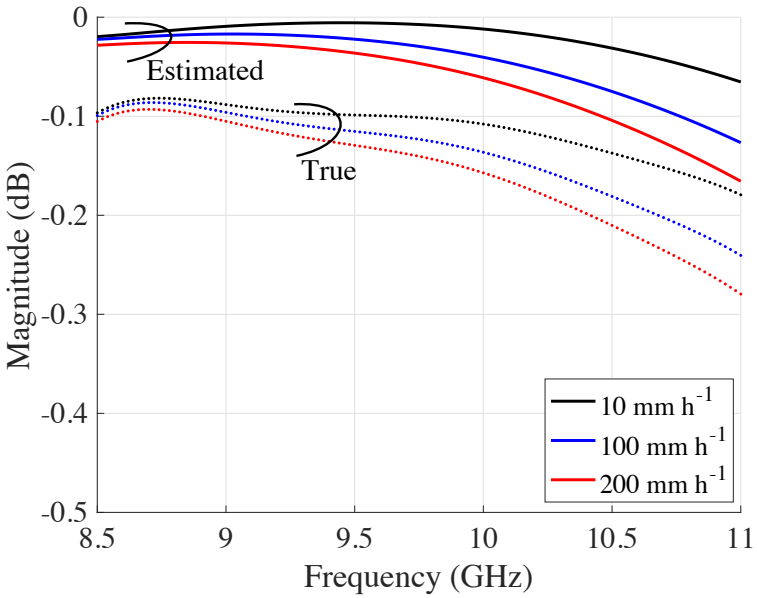

Figure 5.7: Shown is the comparison between the true (dashed line) and estimated (continuous line) transmittances for different rain rates considering droplet formation.

Therefore, when the absorption of the water layer is not dominant, the proposed algorithm is not accurate. This is a limitation of the presented procedure.

5.2.2 Experimental Setup

This section presents the key components to perform measurements with the single-probe technique. To operate, the proposed method requires a narrow beamwidth probe, to achieve high spatial resolution and a reflectometer,

5.2.2.1 Dielectric Rod Antenna

To fully characterize the radome surface using the proposed technique, the antenna employed as a probe requires a small size and narrow beamwidth. An antenna beamwidth is measured at the half-power (-3 dB) point of the main beam. A

narrow beamwidth enables high spatial resolution of the radome measurements and makes it suitable for the investigations proposed in this work. However, if a narrow beam probe is used, the area of the radome sampled by the probe is much smaller than the one sampled by the radar antenna, which operates in the near-field at the distance of the radome. For the case proposed, the sampling area of the probe is only 9 % of the area sampled by the parabolic reflector. A wider area can be sampled if a probe with a larger beamwidth is designed, but it comes at the expense of the spatial resolution. It is left to the user, based on the primary purpose of the application to define this tradeoff. Low weight and small transversal area are key features for easy implementation in operational radars. A small size probe is necessary in order to minimize the signal blockage. The type of antenna selected by the user for conducting this research is the dielectric rod antenna. In the past, dielectric rod antennas were used for diverse applications by Mueller and Tyrrell (1947), Watson and Horton (1948), Kobayashi et al. (1982), Studd (1991), Zucker and Croswell (2007), and Stroobandt (1997). The advantage of using this antenna is that it can be 3D-printed (Saeidi-Manesh et al. 2018; Mirmozafari, Saeedi, Saeidi-Manesh, Zhang and Sigmarsson 2018).

The dielectric rod antenna belongs to the family of surface-wave antennas, and is obtained by placing a dielectric rod in the waveguide aperture. The portion of the dielectric located inside the waveguide is called the feed taper. The feed taper has the function of providing impedance matching at the waveguide-dielectric transition, increasing the efficiency of excitation. The body taper, another part of the dielectric, mainly reduces the level of sidelobes and also increases the bandwidth. The terminal

taper, located at the tip of the dielectric, improves the impedance matching between the dielectric and the air, decreasing the reflected surface wave level (Zucker and Croswell 2007). The length of the neck of the dielectric (Fig. 5.8a) determines gain and beamwidth. However, if there is not sufficient headroom between the radar feed and the radome, or if a smaller impact of the probe on the radar antenna is desired, it is possible to decrease the size of the probe by employing miniaturizations techniques (**?**). In general, a smaller version of the dielectric rod can be obtained by choosing a material with higher dielectric constant. If the beam of the probe is narrow, it is possible to use this antenna as an RF probe for characterization of a smaller radome panel. A narrow beam is more easily confined in the radome sample and no fringing effects from the borders occur (Díaz et al. 2014). The far-field distance of this kind of antenna is 2 - 3λ (λ = 3.2 cm at 9.4 GHz). Considerations about the far-field distance of the probe are important, because the analytical models presented in this work are based on the assumption of a plane wave propagating, which is only valid in the far-field region of the probe. Thus all devices under test must be located in the far-field of the probe.

The dielectric rod antenna employed as a probe, needs to be customized in order to operate at the same frequency band as the radar. In the present research, the probe employed for radome characterization was composed of a rectangular waveguide (commercially available) and a dielectric rod optimized to operate at X-band (designed in HFSS and in-house 3-D printed). The acrylonitrile butadiene styrene (ABS), which is a common thermoplastic polymer, is the material the author had available for 3-D printing the dielectric rod. The probe was then constructed by

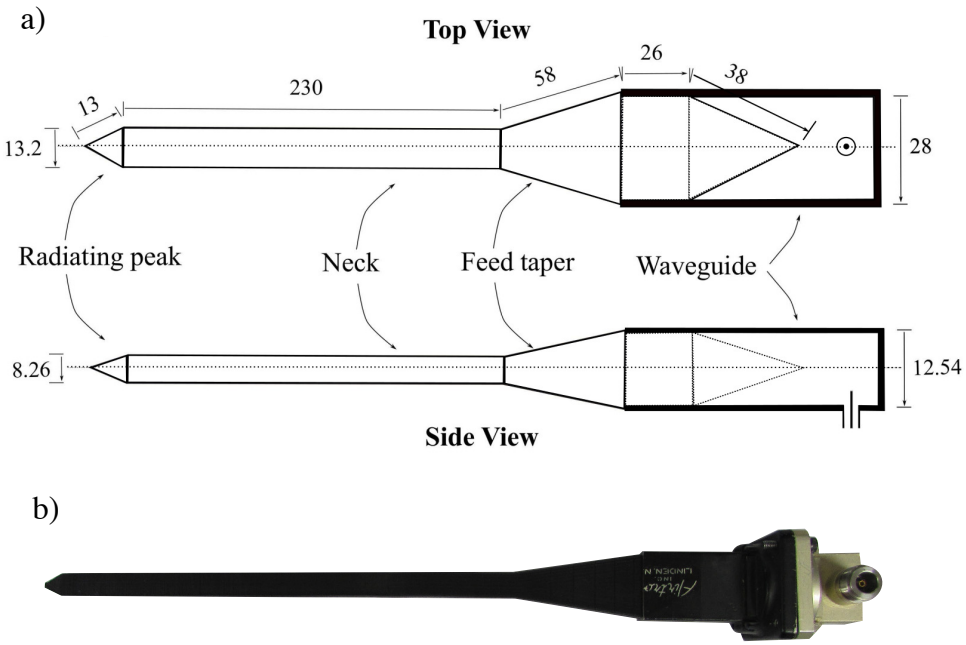

Figure 5.8: a) Two illustrations showing the X-band dielectric rod dimensions (in mm), at top and side views. b) A photograph of the dielectric rod antenna.

wedging the dielectric rod inside the waveguide. In Fig. 5.8a, illustrations of the top and side views of the dielectric rod employed in this study are shown. In this work, an H-band rectangular waveguide was employed to operate in the portion of the frequency spectrum that overlaps with X-band (8.2 - 10 GHz). The reason for this was because an X-band waveguide was not available at the time of the experiments. In Fig. 5.8b, a photograph of the antenna is presented.

The return loss of the dielectric rod antenna is shown in Fig. 5.9. From the plot it can be noted that the antenna provides at least a bandwidth of 10 dB with resonant frequency at 9.4 GHz. In Figs. 5.10a and 5.10b, the radiation patterns of the dielectric rod antenna measured in a far-field chamber are presented for the H- and E-planes, respectively. The measured gain of the probe is 17.5 and 19 dB at 8.8 and 9.8 GHz, respectively. As noticeable from the radiation pattern plots,

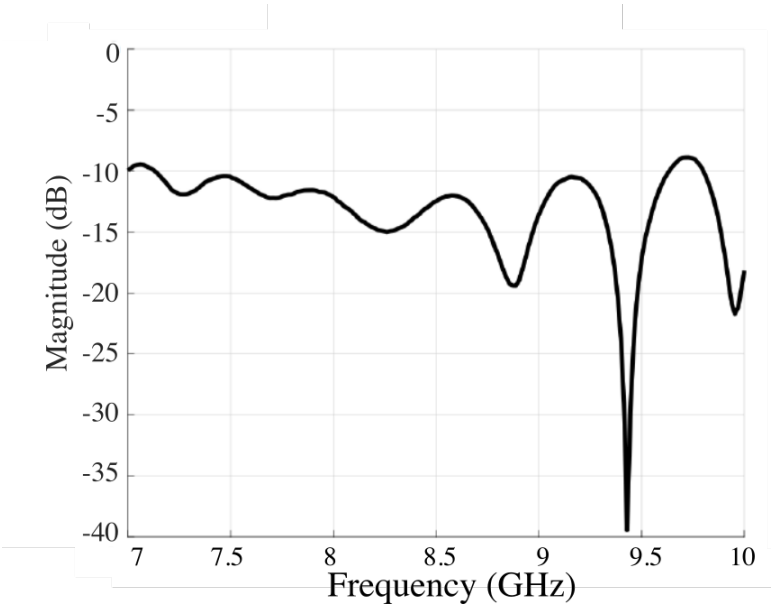

Figure 5.9: The measured return loss of the dielectric rod antenna shown in Fig. 5.8.

the probe presents narrow beamwidth and the low cross-polarization level. Other antennas that provide low cross polarization are discussed in Saeidi-Manesh et al. (2017); Mirmozafari, Saeidi-Manesh and Zhang (2018); Saeidi-Manesh and Zhang (2018).

5.2.2.2 Reflectometer

The novelty of this study is that the radome characterization is performed by measuring reflection coefficient. To accomplish this goal, a vector network analyzer (VNA) reflectometer R140 by Copper Mountain was employed. This device has several applications, including adjustment and testing of antenna-feeder devices and use in automated measurement systems. The operative frequency range of the reflectometer is 85 MHz - 14 GHz. It operates with the assistance of an external computer which also powers the device. The block diagram of the reflectometer (VNA R140)

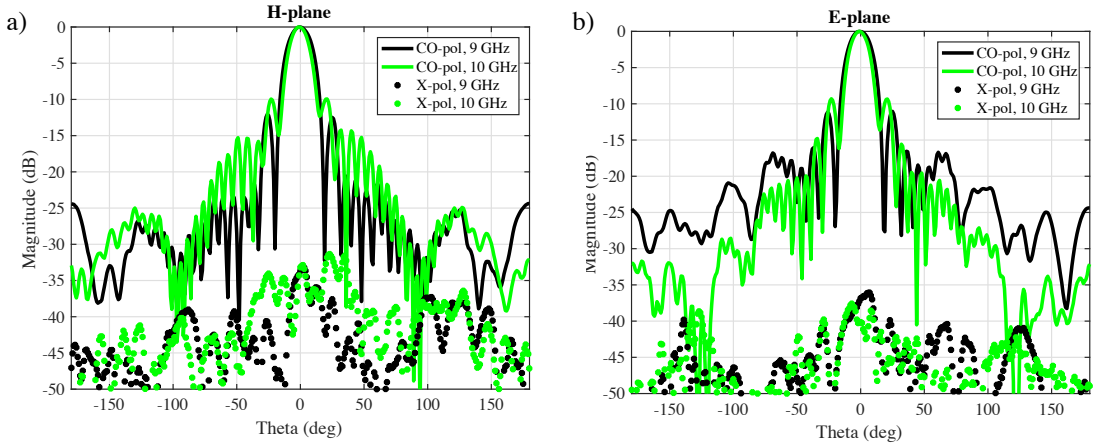

Figure 5.10: The radiation pattern of the dielectric rod antenna measured at 9 and 10 GHz in a far-field anechoic chamber. a) The H-plane. b) The E-plane.

Table 5.3: Measurement accuracy of the VNA R140 reflectometer.

Measurement	**85 MHz-4.8 GHz**	**4.8 GHz-14 GHz**
-15 dB to 0 dB	± 0.4 dB / ± 4°	± 0.5 dB / ± 5°
-25 dB to -15 dB	± 1.2 dB / ± 8°	± 1.5 dB / ± 10°
-35 dB to -25 dB	± 4.0 dB / ± 22°	± 5.0 dB / ± 29°

is shown in Fig. 5.11a. A photograph of the R140 VNA reflectometer is presented in Fig. 5.11b. The main components of the VNA are a source oscillator, a local oscillator, a directional coupler, and a DSP. The output of the reflectometer (test port) is the incident signal. The two-channel receiver filters and digitally encodes the signals. Additional processing of the signals is performed into the DSP. The reflection measurement is performed by comparing the received (reflected) signal with the source signal. An important aspect of the reflectometer is the ability to operate in time domain using the time domain gating analysis which will be discussed next. The pulse repetition frequency of the VNA R140 is 30 KHz. The peak power was set to -10 dBm for the measurements subsequently described. The frequency accuracy of the VNA is ±25 PPM. Other information about the measurement accuracy is summarized in Table 5.3.

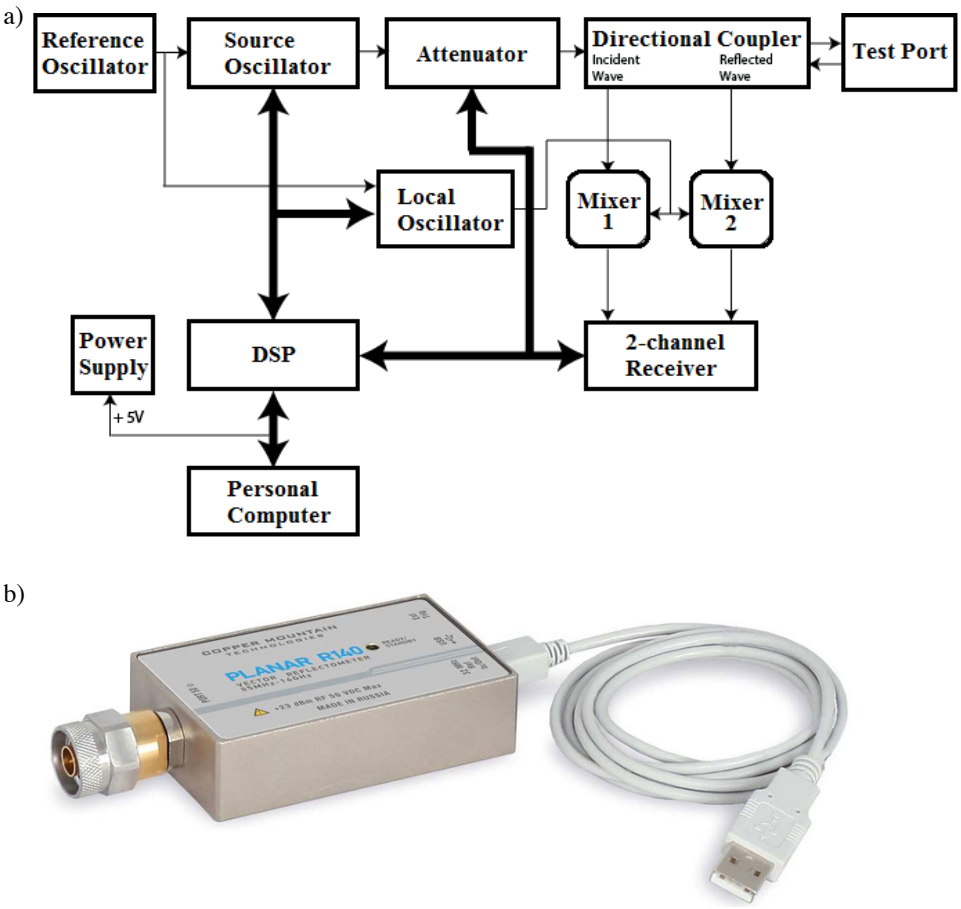

Figure 5.11: a) The block diagram of the reflectometer (R140). b) A photograph of the R140 VNA reflectometer (source: www.rtelecom.net/product/218/r140-1-port-vna-up-to-14ghz-copper-mountain-technologies.html).

5.2.2.3 Time Domain Gating

The concept of time gating is to apply a filter in the time domain. Time gating is distance or spatial filtering, which means that only data from a certain range gate are processed. TDG was employed in the past by various researchers for disparate applications. For example, Archambeault et al. (2006) used it to remove discontinuities or reflections in a free-space context and for tuning purposes. Burrell and Jamieson (1973), Wayapattanakorn and Parini (1993), and Fordham (2010)

employed the TDG to measure radiation patterns, while Ghodgaonkar et al. (1989) and Zaho et al. (2006) used this filter for calibration in free-space measurements.

The Fourier Transform is the operation necessary to switch from frequency to time domain representation, and it applies to continuous signals. The VNA, or reflectometer, performs a Digital Fourier Transform, since it works with discrete data, and the measured signal is a sampled representation of the continuous signal. Consequently, a problem of this operation is the presence of aliasing. Aliases are undesired replicas of the same signal distributed periodically in the time axis. It is fundamental to operate in an environment free of aliases in order to make a correct interpretation of the measurements. The R140 is implemented in order to always represent data free from aliases. Another unwanted effect is produced by the truncation generated by the frequency-finite representation of a signal, which in the real world it is non-limited in frequency, and thus sidelobes are introduced in the time domain. These ringing effects are described by a $sinc(t)$ function and they cannot be totally eliminated (Agilent 2012). To enhance the time domain response, a window can be applied in the frequency domain to control the sidelobes in the time representation due to the truncation process. In the presented study, a normal type of Kaiser window with -44 dB of sidelobe level was used.

The gate can be thought of as a filter in the time domain. However, the operation of "gating" is actually applied in the frequency domain by defining the start and stop gate times which determine the dual frequency gating function. Dunsmore (2008) conducted a study to evaluate errors in the time domain response due to an

inaccurate positioning of the gate around the desired region. Other limitations of the gating function are described in the application note (Agilent 2012).

The process of representing a continuous signal by a sampled (discrete) version of itself produces periodic repetitions. These unwanted replicas are called aliases and they are located at multiples of $1/B$ seconds. In this specific context, the band B is the frequency range selected to represent the signal in the frequency domain. The alias-free range is also called the unambiguous range. It is the maximum (time or distance) range where replicas of the signal are not visualized. Defining $B = f_{max}$ - f_{min}, f_{min} and f_{max}, the start and stop frequency respectively, the time range can be computed as:

$$T = \frac{N-1}{B} \tag{5.3}$$

where N is the number of measurement points. For example, by choosing $N = 61$ and $B = 3$ GHz a time range of 20 ns is achieved. The ambiguity range is given by:

$$R_{max} = \frac{cV_fT}{2} \tag{5.4}$$

where c is the speed of light and V_f is the cable velocity factor. The ambiguity range is 3 m if $V_f = 1$ and $T = 20$ ns. The factor 2 at the denominator is necessary to take in to account the roundtrip of the signal.

The range resolution is the capability of the reflectometer to resolve two responses close (in space or time) to each other. It is calculated as (Agilent 2012):

$$\Delta R = \frac{\Delta tcV_f}{2} \tag{5.5}$$

where Δt is the 50% points of the impulse width (time). It is defined as:

$$\Delta t = \frac{1.95}{B} \tag{5.6}$$

The constant 1.95 is related to the choice of a normal Kaiser window (Table 1-3 in Agilent (2012)). There is no specific reason for the choice of the Kaiser window of type normal for the experiments performed in this work. For a 3 GHz bandwidth the Δt is equal to 0.65 ns, and the range resolution is 9.75 cm. From Eqs. 5.5 and 5.6, it is clear that increasing the frequency range decreases the minimum distance at which two targets must be located in order to be resolved.

In the proposed study, TDG is necessary to more accurately measure the reflections produced from the radome without contamination from the reflections generated by the surrounding environment. The TDG is an important technique to remove undesired reflections. Such reflections are generated by impedance mismatches and it is fundamental to understand what is the cause of them. Impedance mismatches create loss of the energy of the incident signal because part of it is reflected. Furthermore, impedance discontinuities can obscure the response of the subsequent mismatches, because the energy reflected from the first impedance mismatch never reach the following ones. Such an effect is called masking (Agilent 2012). The factors that contribute to generate discontinuities in the proposed research is the presence of cable, waveguide, and dielectric rod (previously described).

5.3 Summary

The first part of the chapter described the common two-probe technique to characterize radomes. However, because the limitations of this method a new approach was presented and validated. The proposed method is the single-probe technique which bases the radome characterization on the measurement of the reflection coefficient. The two-probe method uses the TDG to improve the measurement quality. This solution can be employed in operative radars that have a reflector dish as an antenna to perform real-time assessment of the radome during radar operations.

In addition, the electrical devices needed to implement the single-probe method were introduced. To achieve high spatial resolution, a narrow-beam probe is necessary. This allows to characterize small flaws and imperfections present in the radome. The reflectometer was introduced and its principle of operation is discussed. In addition, the TDG was also discussed and the related formulations for the correct implementation were presented. The following chapter will show radome characterization performed by using the single probe technique.

Chapter 6

Validation of the Proposed Method

In this chapter, measurements performed on operational S- and X-bands radomes are discussed. The purpose of this chapter is to validate the proposed technique based on the single-probe characterization method. For both the S- and X-bands cases, the radome characterization is carried out in the far-field region.

To measure the effect of water on the far-field radiation pattern, a second experiment is performed in a near-field chamber on an S-band 8 x 2 dual-polarized phased array antenna. The antenna used for this second type of experiments is a prototype of antenna developed for the Horus project (Díaz et al. 2016). These tests were executed to evaluate the amplitude and phase degradation of the far-field radiation pattern of the antenna, in the presence of water in the near-field region of the antenna.

6.1 Far-Field Radome Characterization

6.1.1 Laboratory Setup with Flat Radome Panels

To validate the single probe radome characterization technique, discussed in Chapter 5, a laboratory setup was built to enable the testing that provided preliminary

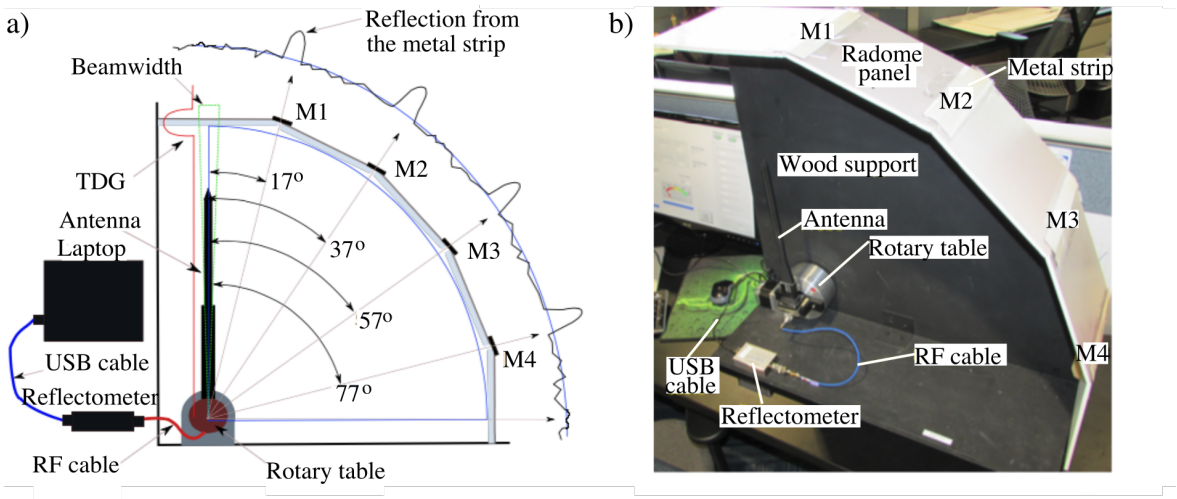

Figure 6.1: The setup for laboratory experiment performed at X-band using the single-probe technique. a) Graphic representation of the radome setup including the probe, rotary motor, and reflectometer. b) Photograph of the setup with probe, rotary motor, and reflectometer.

results. This section is divided into two parts. The first section describes the measurements obtained from a setup composed of flat radome panels (Fig. 6.1). The purpose of these experiments is mainly to validate the dielectric antenna, reflectometer, and TDG, as a system to evaluate the effect introduced by the radome in terms of reflections (Mancini et al. 2017).

In Fig. 6.1a and 6.1b, a schematic representation and a photograph of the setup are shown. The laboratory setup is composed of five radome panels arranged to approximate a quarter of circumference. The rotary motor with the probe mounted on it is located at the origin of the circumference. The panels are placed abutting each other leaving small air gaps between each other. These air gaps are located at $\theta = 17°$, $37°$, $57°$, and $77°$ with respect the initial position of the rotary motor, as shown in Fig. 6.1a and 6.1b. To keep the radome panels in a stable position above the antenna, and to secure the rotary motor to a fixture, a wooden support was

used. Because imperfections of the setup, the distance between the antenna and each panel is not identical.

The radome panel is made of foam as an inner layer (6.62 mm) and teflon as a skin layer (0.53 mm). In Fig. 6.1a, the antenna is placed at the start position (broadside, $\theta = 0°$) of the rotary motor, the probe beamwidth is shown in green, the TDG is displayed in red and centered at the radome location, and the predicted results for reflection measurement are shown. Both a flat response of the reflection coefficient from the radome panel, and a strong reflection coefficient peak generated from each metal strip located at the junction between two consecutive panels, are expected.

Based on the analytical formulation of the TDG, presented in Chapter 5, it is necessary to set the the filter in the domain in agreement with the setup configuration. In this way, it is possible to center the gating window appropriately to remove the unwanted reflections and therefore, improving the measurements. In addition, it is necessary to take into account the RF cable calibration. The procedure about how to setup the TDG and cable calibration is described in detail in Appendix A. Software considerations are reported in Appendix B.

Results obtained from the laboratory setup are shown in Fig. 6.2 (Mancini, Salazar, Lebrón and Cheong 2018*a*). Measurements of the reflection coefficient are plotted as function the tilting angle of the probe, at the frequency of 9.4 GHz. A 3-GHz bandwidth (7 - 10 GHz) is considered to have good resolution in time domain. The experiments were performed three times under the same conditions to assure the reproducibility of the experiment. The measurements were then compared

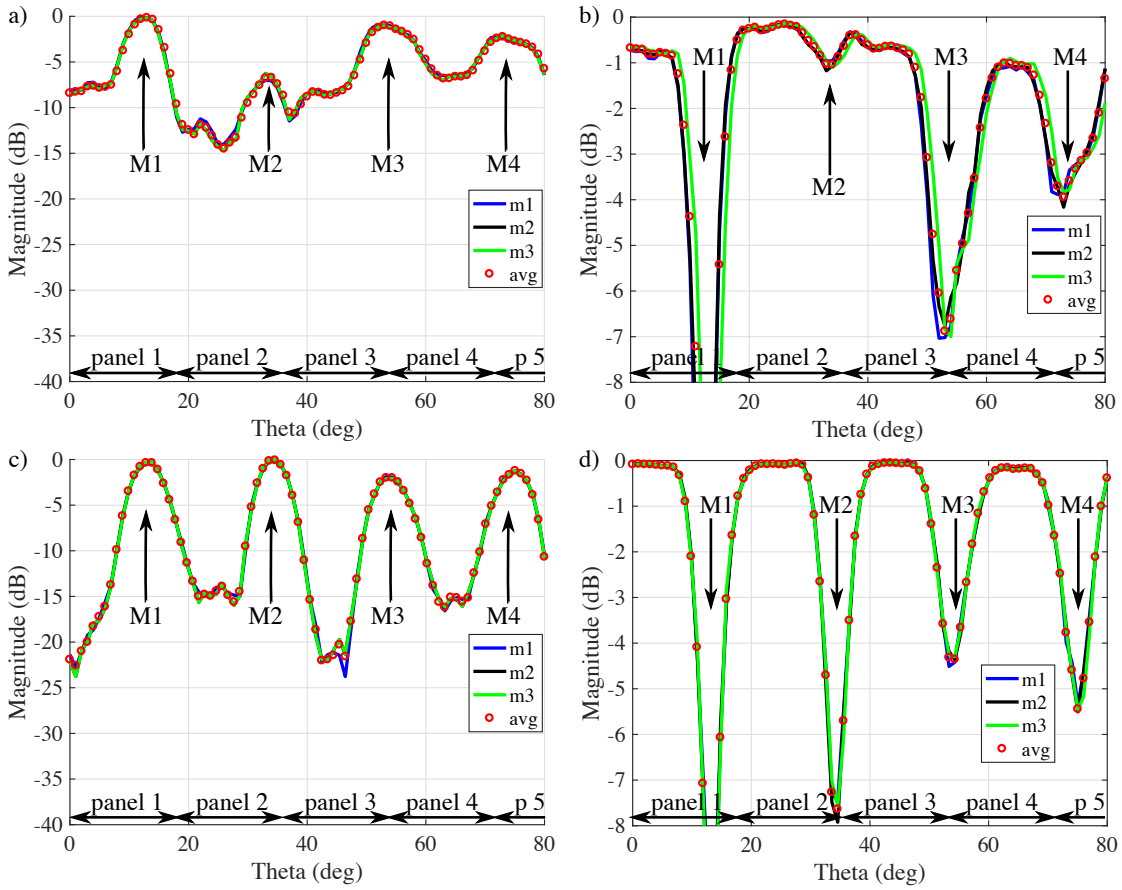

Figure 6.2: The results of the X-band flat radome setup in dry conditions shown in Fig. 6.1. Results plotted at 9.4 GHz. a) The measured reflectance without applying TDG. b) The calculated transmittance without applying TDG. c) The measured reflectance with TDG applied. d) The calculated transmittance with TDG applied.

with the average. In the first experiment, the TDG was not employed in order to determine if a good quality of the reflectance measurement could be achieved without using the gating in time domain. Strong reflections (peaks) from the metal strips were expected, and therefore could be visualized without TDG. In the current work, the same results are shown in terms of transmittance by applying Eq. 4.21, and are shown in Fig. 6.1c. In Fig. 6.2a and 6.2b results for the reflectance and transmittance are presented without applying TDG. In the figures, $m1$, $m2$, $m3$, and avg represent the three measurements and the related average, while $M1$, $M2$, $M3$,

and $M4$ indicate the metal strip locations. The goal of this first set of measurements is to prove that the TDG is a fundamental analysis to remove undesired reflections and improve the measurement quality. As noticeable from the Fig. 6.2a, without TDG it is not possible to identify the strong reflections coming from the metal strips located at the top of the radome. Therefore, it will results much more difficult to evaluate the effect of the radome, because its electromagnetic transparency. Results for the reflectance show that the multiple paths generated from other surfaces of the setup, affected the measurements considerably by canceling some of the peaks. From Fig. 6.1c, only the first strip ($M1$), located at 17°, generates a well formed peak. The peaks related to M3 (at 57°) and to $M4$ (at 77°) are less pronounced. The peak of $M2$ (at 37°) is barely visible due to a combination of destructive reflections. The peaks $M1$, $M3$, and $M4$ shown in Fig. 6.1c do not have the same amplitude, partially due to the fact that the distance from the antenna to each radome panel is not the same. In Fig. 6.2b, the transmittance was calculated by using Eq. 4.21. The absorption of the dry radome was neglected.

In the second set of experiments, the TDG was applied. In Fig. 6.2c, the measured reflectance is presented. As noticeable, the measurement is much improved for the previous case where TDG was not included. All four peaks are now well defined and clearly identifiable. In Fig. 6.2d, the calculated transmittance (Eq. 4.21) with TDG applied present better nulls at the locations of the metal strips with respect the scenario where TDG was not applied (Fig. 6.2d).

In the following section, the setup considered for this experiment is slightly modified to provide additional validation of the single-probe radome characterization technique.

6.1.2 Laboratory Setup with Parabolic Radome

For the second part of this study, the setup was modified. The reason for this modification is to characterize an operational radome that is not flat, but presents a curvature. Three of the radome panels were removed and a Ku-band radome (also applicable at X-band) replaced them, leaving a large air gap between the radome and the remaining two panels. The Ku-band radome has a circular shape with a 60 cm-diameter and presents a small angle curvature from the center to the peripheral area. However, at the borders the termination is cornered, so it can be mechanically fixed to the reflector. In Fig. 6.3a and 6.3b, a schematic view and a photograph of the modified setup are presented, showing the predicted behavior for the reflection coefficient as in the previous setup.

To have a complete scan of the Ku-band radome, it was necessary to start the measurements at θ = -25° (instead of 0° as in the first setup employed). In the tests performed with the modified setup, no metal strip was employed, so the normalization was with respect to the highest level of reflection which occurred at broadside (θ = 0°). The TDG analysis was not employed for the first experiment. Measurements performed without using the TDG, are shown at the frequency of 9.4 GHz in Fig. 6.4a and 6.4b for the reflectance and the transmittance. The transmittance was again computed by Eq. 4.21. As in the case presented in Fig. 6.1c, this test also

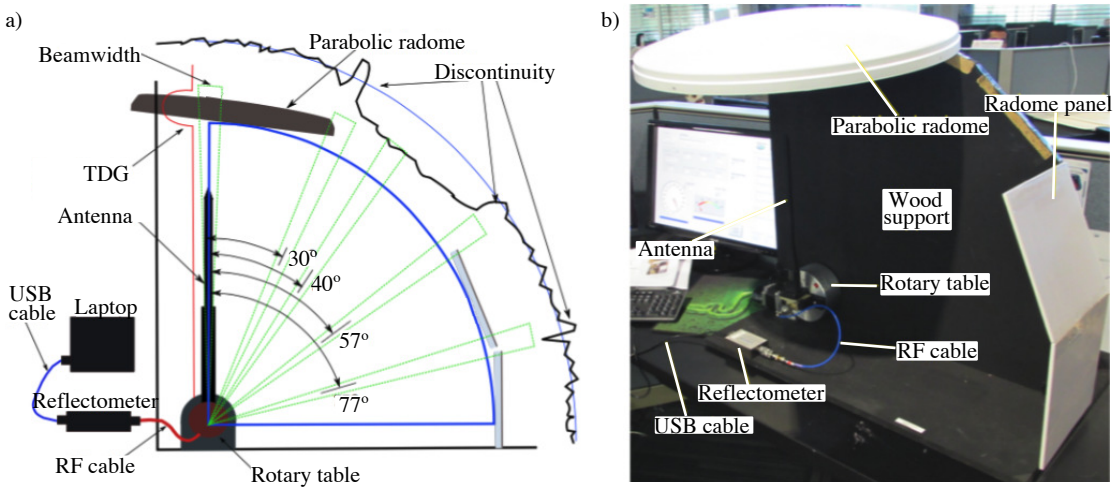

Figure 6.3: The laboratory setup employing the proposed technique using a parabolic Ku-band radome. a) Graphic representation of the setup including the probe and reflectometer. b) Photograph of the setup with probe and reflectometer.

required the filter in the time domain in order to improve the quality of the experiments. In the second test the TDG analysis was applied and a 3 GHz-bandwidth (7 - 10 GHz) was considered to assure good resolution in the time domain. The TDG start and stop times were adjusted to account for the dimensions of the new radome, taking into account its curvature. Results are shown in Fig. 6.4d and 6.4f for the reflectance and transmittance. It is valuable to compare the two plots in Fig. 6.4c and 6.4d in the range of 30° to 60°, where no reflection was supposed to be measured, since it is the air region. In the air region, the value of reflection is higher without applying the filter in the time domain, because reflections from other parts of the setup and the rest of the environment were not filtered out.

6.1.3 S-band Radome

The performance of a radome panel of the WSR-88D radar (2.7 - 3 GHz) was tested in both dry and wet conditions at orthogonal incidence. The radome panel is of

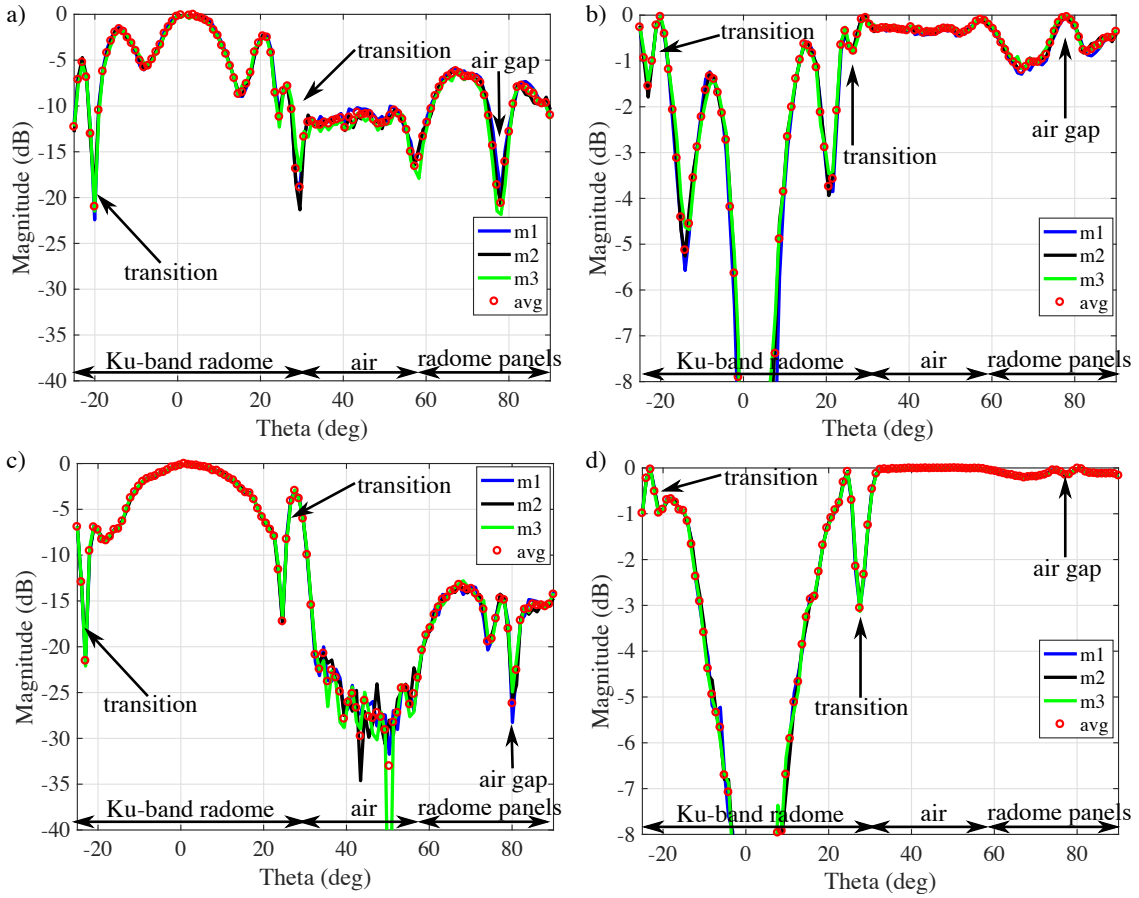

Figure 6.4: The results obtained from the setup shown in Fig. 6.1. Results plotted at 9.4 GHz. a) The measured reflectance without applying TDG. b) The calculated transmittance without applying TDG. c) The measured reflectance with TDG applied. d) The calculated transmittance with TDG applied.

pentagonal shape and is shown in Fig. 6.5a. The dimensions of the panel are 2.34 m in height and 2.27 m in width. The method uses a single probe connected to a reflectometer to measure the folded reflectance generated from the multilayer radome. By using the TDG analysis, implemented in the reflectometer, it is possible to minimize the effect of multiple reflections coming from the surrounding environment, and therefore, improve the data quality. The single probe method, as well as the benefit of using TDG, were discussed in Mancini, Salazar, Lebrón and Cheong (2018*a*) and Mancini, Salazar, Lebrón and Cheong (2018*b*). In this research, a horn antenna (2.6

- 3.95 GHz) was used to characterized the RF performance of the WSR-88D radome. The reflectometer employed is the R140 series by Copper Mountain, which operates in the range of 85 MHz to 14 GHz, with a pulse repetition frequency of 30 KHz. Further technical aspects of this device are discussed in Mancini, Salazar, Lebrón and Cheong (2018*a*). To have good spatial resolution in time domain, the frequency range should be as wide as possible. The largest possible band of operation of the reflectometer is dictated by the frequency band of the horn antenna, which ranges from 2.6 GHz to 3.95 GHz. The distance probe-radome panel was about 1.5 m, which assured that the horn antenna would operate in far-field. That distance also allowed confining the beam of the horn antenna inside the radome sample (no fringing effect from the borders). The start and stop times of the gating function were 6.8 ns and 7.28 ns. The probe was mounted on a robotic arm to assure good stability and accuracy during the measurements. The robotic arm also allowed keeping the horn antenna aligned with the center of the radome when the probe was rotated to 90° to measure in the other polarization. The experimental setup is shown in Figs. 6.5a and 6.6d.

Radome performance was initially measured in dry conditions for both polarizations (Mancini, Lebrón and Salazar 2018). Then, a subsequent experiment repeated the first, but used an ordinary sprinkler to wet the radome. The sprinkler was placed on a pole in front of the radome panel, outside of the range of time gating, to make sure that the reflections produced by the pole were filtered. The sprinkler wet the radome at the top, with water flowing naturally down to the base of the radome. Since the radome panel was not new, the hydrophobic property of the raincoat had

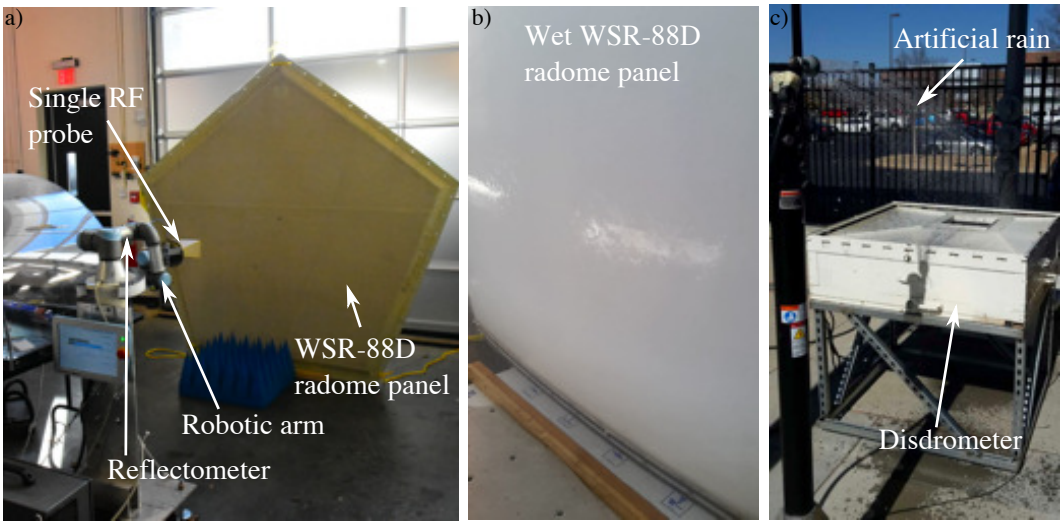

Figure 6.5: The experimental setup employed to characterize in far-field the RF performance of the S-band WSR-88D radome panel. a) The radome panel, probe, and reflectometer mounted on the robot arm. b) A photograph taken during the experiment under artificial rain conditions, showing the water distributing as a continuous film. c) The 2-DVD employed to measure the rain rate of the sprinkler.

been exhausted before the the experiments were conducted. Therefore, water distributed as a film, as shown in Fig. 6.5b. To have an approximate measurement of the rainfall rate produced by the sprinkler, a 2-D Video Disdrometer (2-DVD) was used. The sprinkler mounted on the pole, and the 2-DVD, are presented in Fig. 6.5c. The measured rain rate was not constant because wind moved the water beam away from the aperture of the disdrometer, causing only a portion of the water to fall inside the sampling window. The measured rain rate is shown in Fig. 6.6a. The average and peak rain rates are 63 and 102 mm h^{-1}. The measured reflectance for the dry, wet, and drying scenarios are shown in Fig. 6.6b. The curves plotted in time domain were obtained as an average of the reflectance measured in frequency domain over all of the bandwidth selected (2.6 - 3.95 GHz). These curves are normalized, with respect to the reflectance obtained, by placing a metal plate behind

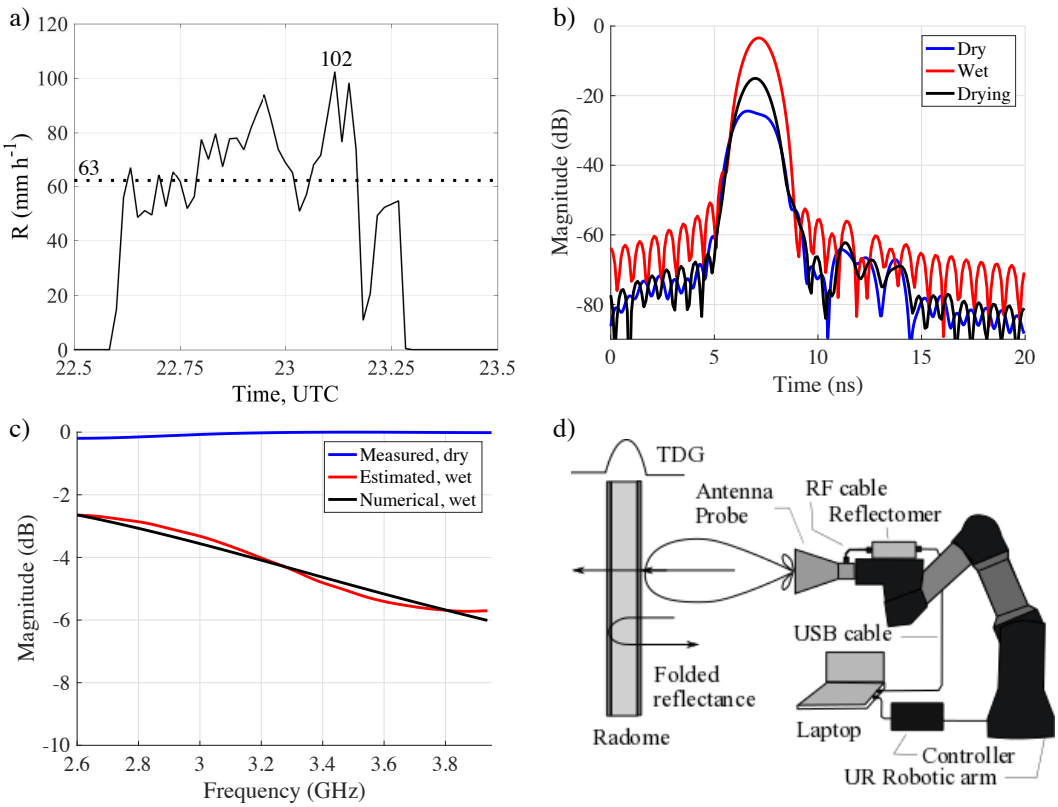

Figure 6.6: The RF characterization of the S-band radome (WSR-88D) in far-field using a single probe. a) The rain rate generated by the sprinkler and measured from the 2-DVD. b) The reflectance in time domain. c) The transmittances obtained for the dry and wet scenarios compared to the one simulated numerically. d) A schematic representation of the setup employed for the experiment.

the radome for the purpose of calibration. As expected, the curve corresponding to the dry scenario presents the lowest reflectance, while the one obtained in wet conditions produces the highest values of reflectance. The curve that represents the drying case was measured when water was no longer sprayed on the radome. Therefore, the amount of water on the radome was lower than in the wet scenario. Since these tests were performed using a single probe, it is not possible to directly measure the transmittance, because absorption (A) occurs (T = 1 - R - A). However, it was demonstrated in Mancini, Salazar, Lebrón and Cheong (2018*a*) and Mancini, Salazar, Lebrón and Cheong (2018*b*), that by knowing the rain rate, it is possible to

compute the thickness of the water film accumulated on the radome. By executing a numerical simulation, it is possible to estimate the attenuation of the signal crossing the water layer. Therefore, the transmittance can be indirectly computed. For the simulation, the thickness of the water layer was computed by using Gibble's formula (Gibble 1964), also employed by Mancini, Salazar, Lebrón and Cheong (2018*a*). To compute the thickness of the water film, the maximum rain rate measured by the 2-DVD, was used. The highest rain rate registered during the experiment was 102 mm h^{-1} (Fig. 6.6a). The radius of the spherical radome was equal to 11.89 m. The calculated thickness was of 372 μm. The simulated and estimated transmittances are plotted in Fig. 6.6c. The figure shows that the estimated transmittance closely approximates the one obtained through numerical analysis, proving the validity of the chosen approach. The transmittance of the drying scenario was not estimated, because it was not possible to evaluate the thickness of the film while the water was drying. In Fig. 6.6d, a schematic representation of the technique is presented.

6.1.4 X-band Radome

Fig. 6.7 shows photographs of the X-band PX-1000 radome taken outdoors on a sunny day. The physical external dimensions of the bullet shape radome are 87.23 in (2.22 m) in diameter, 75.25 in (1.91 m) in total height, and 31.63 in (0.8 m) for the height of the cylindrical base. The dark areas noticeable in most of the sub-figures in Fig. 6.7 are non-homogeneities located inside the radome. Such non-homogeneities are imperfections occurring either during the fabrication or assembly processes, and they can generate nonuniform levels of attenuation in various parts of the radome.

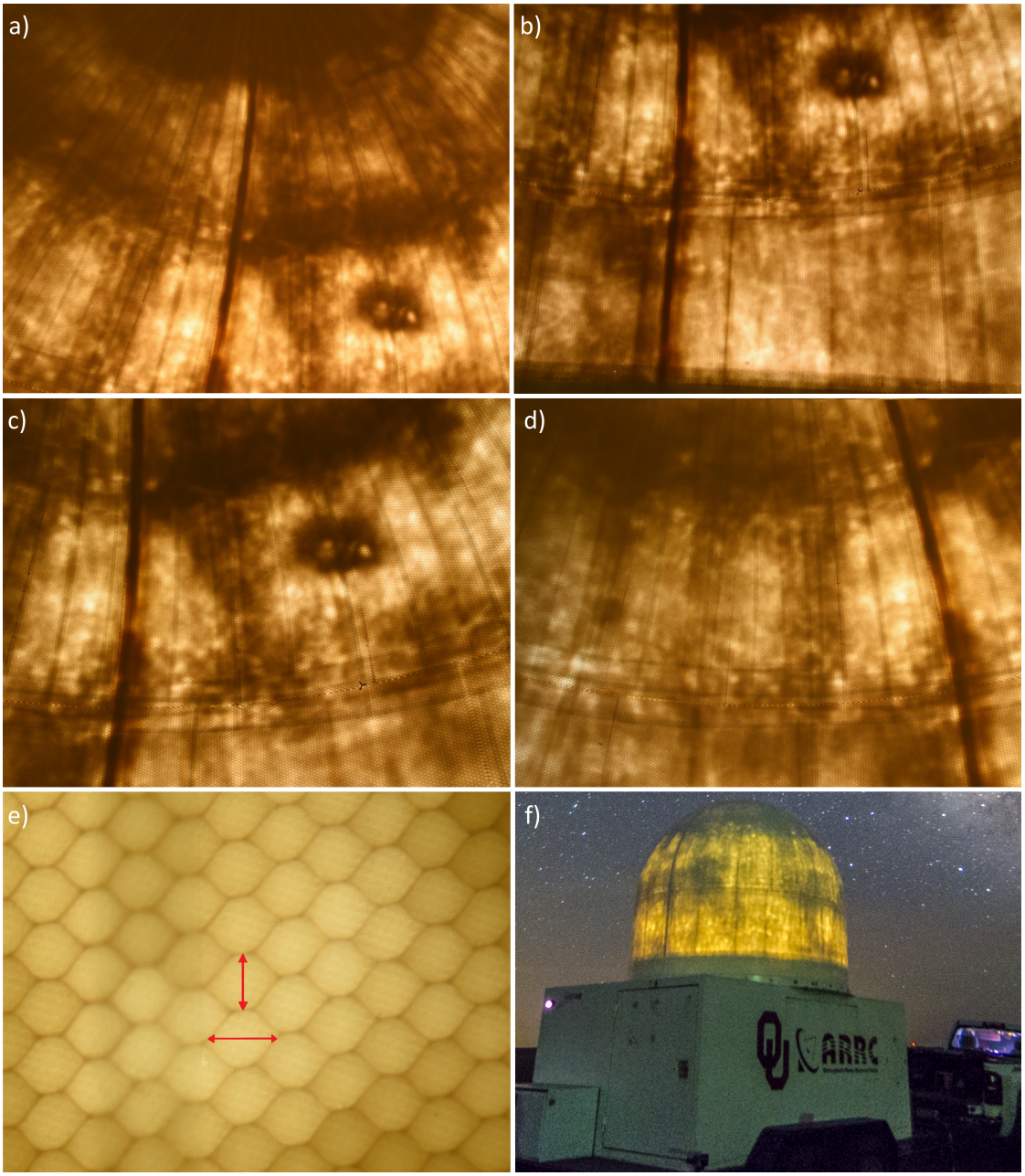

Figure 6.7: The X-band PX-1000 radome: a) an overview, b) the cylindrical base, c) and d) two photographs of the spherical part at different azimuth locations, e) a close-up, and f) a long-exposure photo taken at night (photo courtesy of Jim Kurdzo).

An example is visible in Fig. 6.7a, 6.7b, and 6.7c, where a dark area, similar to an 8 laying horizontally, is discernible. Another factor that could introduce an additional level of attenuation is due to the junctions where the panels composing the radome are attached to each other. Radome panelization is noticeable in Fig. 6.7f. Furthermore, the radome was constructed in halves, with the dark vertical line appearing in the first four photos in Fig. 6.7 showing the junctions between them. An additional element that is able to affect dual-polarized radar performance, is the geometry of the honeycomb hexagons composing the radome. Honeycomb geometry forms different patterns along the directions of x and y, resulting in the distance between adjacent hexagons being different in vertical and horizontal. All the above-mentioned factors may affect the level of polarization in the V- and H-polarizations and the related attenuation. This effect is accentuated when water is present on the outer surface of the radome.

Besides the flaws apparent by simple visual inspection, other imperfections might be present that cannot be detected by the naked eye. To detect and quantify the effect due to all imperfections, a dry radome RF characterization is useful. Mapping the position of the imperfections makes it possible to correct for attenuation of the radome while the radar is operating.

On a quarter of the surface of the radome hemisphere, Rain-X was applied before starting the experiment in wet conditions. Rain-X by ITW Global Brands, is a substance designed to increase the hydrophobic properties of the car windshields to improve visibility, keeping water in droplet form. It is a hydrophobic silicone polymer that forces water to bead and roll off of the car. Rain-X was employed in

this experiment to compare different water formations on the surface of the radome. For instance, droplets and rivulets were anticipated to be distributed on the portion of the radome where Rain-X was applied, while a continuous film was expected on the reminder of the radome. The Rain-X treated portion of the radome, is predicted to have a different response from the untreated area in terms of reflectance (R), or similarly, in terms of transmittance (T). Furthermore, the presence of Rain-X, will have a different influence when the signal is horizontally polarized than when it is vertically polarized. This is not expected on the rest of the radome where water distributes as a continuous film.

6.1.4.1 Case 1: Cylindrical Radome in Dry Conditions

For the dry case scenario, the cylindrical and the hemispherical parts of the radome is discussed separately. The scenario for the wet case will be presented showing the characterization of the radome for only the hemispherical portion. Results for each of the cases will be discussed presenting the reflectance and the estimated transmittance for H- and V-polarizations (R_H, T_H and R_V, T_V, respectively). The absorption of the radome in dry conditions was neglected because it is very low, while for the wet radome was estimated by using the algorithm discussed in Mancini, Salazar, Lebrón and Cheong (2018*a*). A vertical metal strip, of 15.6 cm width, was placed on the outer surface of the radome to provide reference during the tests (Mancini, Salazar, Lebrón and Cheong 2018*b*).

The cylinder was tested only in dry conditions. The related measurements are shown in Fig. 6.8 for the reflectance and Fig. 6.9 for the transmittance. In all the

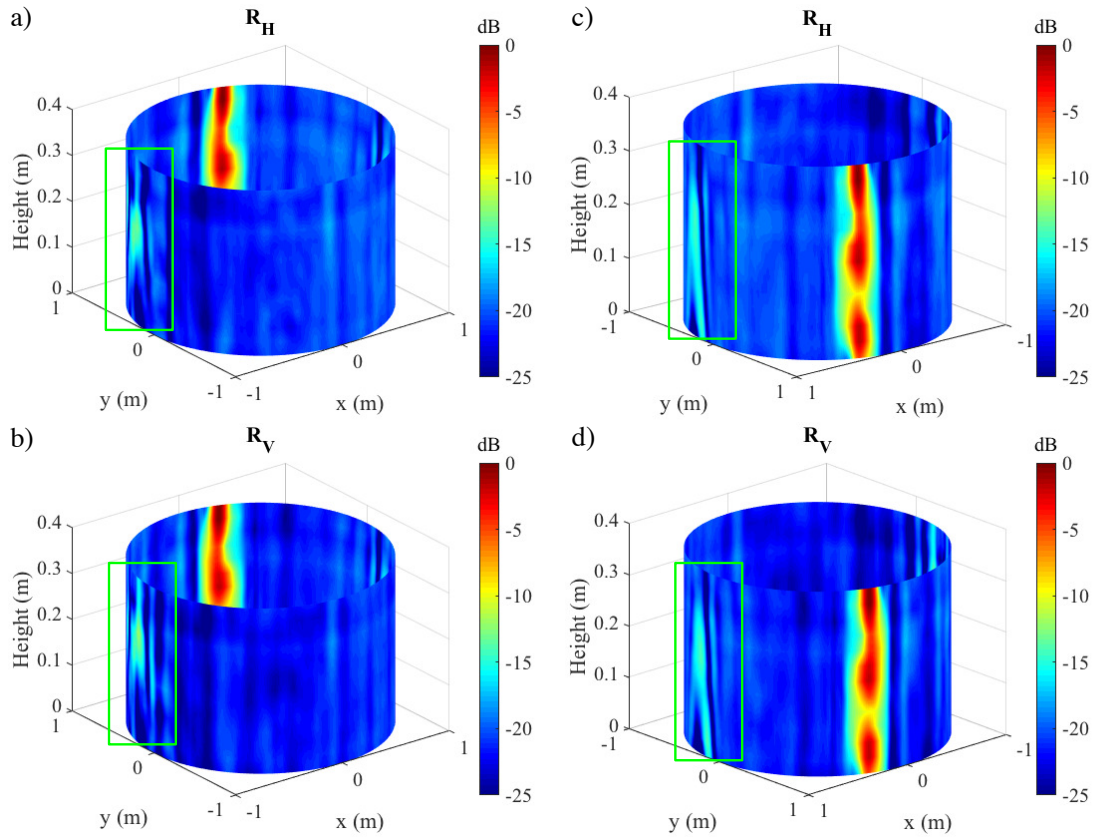

Figure 6.8: Shown is the reflectance (R) measurement for the cylindrical part of the radome in dry conditions. The top row shows the H-polarization and the bottom row presents the V-polarization. Shown in a) and b) are results for one side of the radome. Shown in c) and d) are results for the opposite side. The line marked in red represents the reflection coming from the metal strip.

sub-figures of Fig. 6.8, it is important to note the area of high reflection discernible on the left side of the radome. The level of reflectance at that location is about -12 dB and -17 dB on the two sides of the radome. This area of high reflection is probably due to an imperfection produced during the assembly process. The cylindrical part of the radome is constructed with joined halves. The area shown in this figure is the junction where the two halves are attached and patched, introducing a discontinuity. When the probe scans in the regions where such imperfections occur,

diffraction is generated. In the rest of the cylindrical part of the radome, the level of the reflectance is about -25 dB.

The transmittance for the test performed under dry conditions, is shown in Fig. 6.9. The two polarizations present similar values of transmission coefficient (about -0.1 dB). To the left of these figures, corresponding to the spot where the radome imperfection is located, an area with 0.2 dB attenuation is noticeable. This flaw generates a peak of -0.25 dB when the probe is vertically polarized (Fig. 6.9b). This peak value is not reached when the probe is horizontally polarized (Fig. 6.9a), suggesting that the imperfection affects the two polarizations in a slightly different way, probably because of the geometry of the flaw. In Fig. 6.9e, a photograph of the radome from outside and a close-up of the inside are shown. In Fig. 6.9e, highlighted are the characterized portion of the cylinder (in red), the locations where the internal close-up was taken (in yellow), and the flaw in the radome (in green).

To conclude this section, the difference in dB between the reflectance measured with the probe polarized horizontally and the one obtained with the probe polarized vertically (differential reflectance) is discussed. Such results are important because they provide an idea of how much the dual-polarized radar products can be biased due to the presence of the radome imperfections. Results are shown in Figs. 6.10a and 6.10b for the differential reflectance. As noticeable from the figure, the level of reflectance is not uniform. In fact, there are various locations the present +2.5 dB difference in the front and back part of the B-side (Fig. 6.10a). In addition, the side of the radome where the junction between the two halves are located, presents larger difference than the reminder of the radome. Such a difference also changes quickly

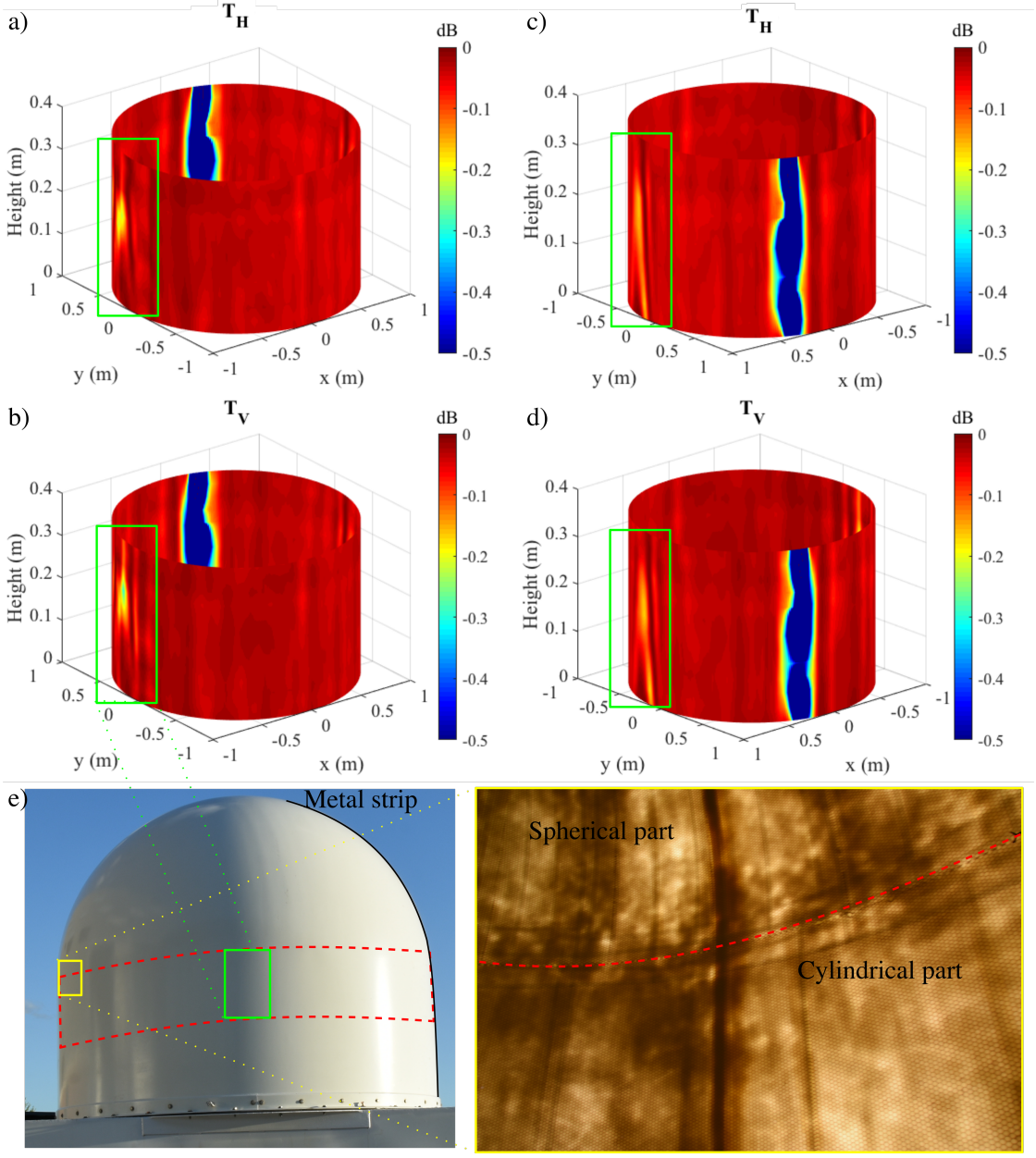

Figure 6.9: Shown is the transmittance (T), neglecting the absorption, for the cylindrical part of the radome in dry conditions. The top row shows the H-polarization and the bottom row presents the V-polarization. Shown in a) and b) are results for one side of the radome. Shown in c) and d) are results for the opposite side. Shown in e) are photographs of the radome from outside, and a close-up of the internal view.

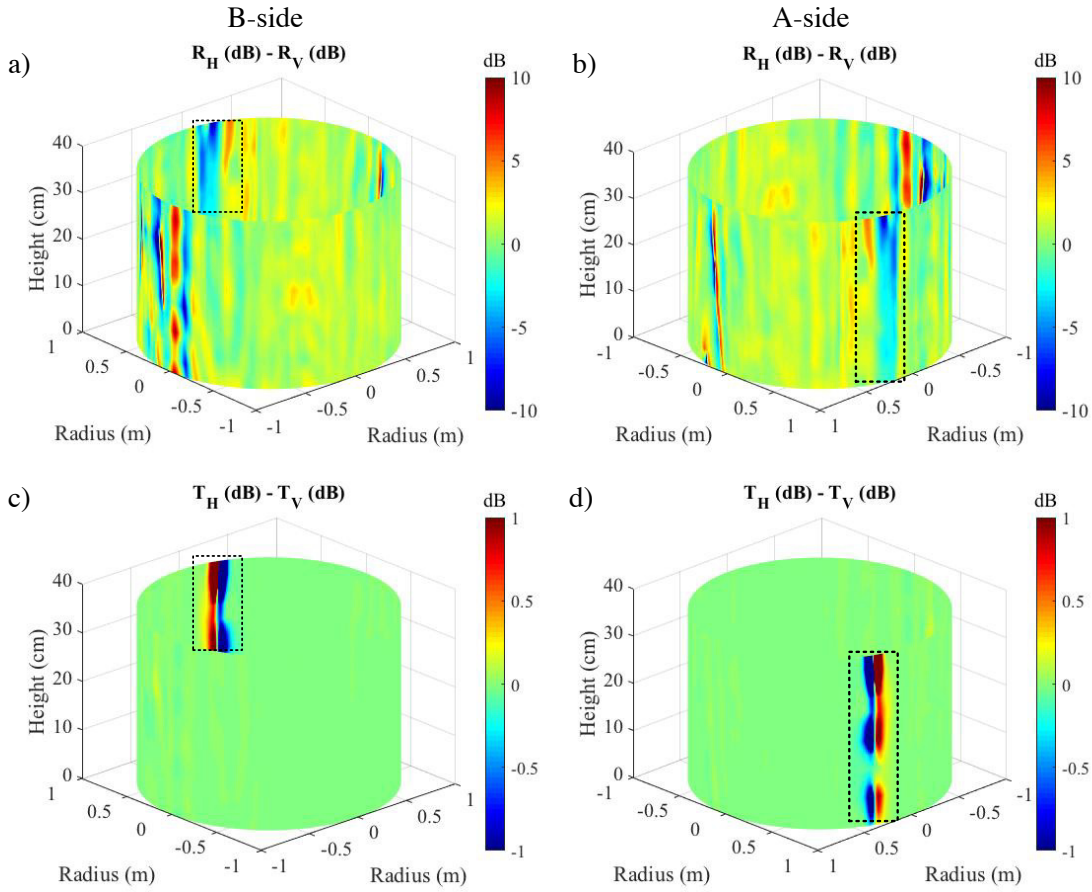

Figure 6.10: Shown is the difference between the H- and V-polarizations for the reflectance (R) and transmittance (T) for the measurements performed for the cylindrical part of the radome in dry conditions. a) and b) Results for the differential reflectance for the A- and B-side of the radome. c) and d) Results for the differential transmittance for the A- and B-side of the radome. Highlighted with a dashed rectangle is the portion of the radome covered with the metal strip.

with respect to the location nearby. For example, over -5 dB-difference is because diffraction is generated in portions of the radome that presents non-homogeneities.

Results for the differential transmittance are shown in Figs. 6.10c and 6.10d. As it can be observe from the figure, the highest difference occurs where the two halves of the radome are attached. This difference is about +0.2 dB. In the reminder of the radome, the differential transmittance is uniform and the value presented is about ± 0.05 dB.

6.1.4.2 Case 2: Semi-Spherical Radome in Dry Conditions

Reflectance results for the hemispherical part of the bullet-shaped radome are shown in Fig. 6.11. Just as with the cylindrical portion, the spherical part of the radome shows good agreement between both polarizations. Looking at Fig. 6.11a and 6.11b for the reflectance R, or equivalently at Fig. 6.12a and 6.12b for T, another example of a flaw not detectable by visual inspection is located at the base of the hemisphere, but is present only on the B-side of the radome. The flaw is shown in Fig. 6.11a and 6.11b in a green frame. In the author's opinion, this is an air gap formed during the assembly of the radome. The level of higher reflection that is generated by diffraction occurring at the border of the air gap is due to manufacturing imperfections. There is also some difference on the order of magnitude between A- and B-side (Fig. 6.11). In B-side, vertical lines showing a reflection coefficient of -17 dB are more frequent than in the A-side, for both polarizations. A magnitude of -25 dB is more uniformly distributed in the A-side.

In Fig. 6.12, the transmittance is shown. Similar comments can be deduced for T. A photograph of the external part of the radome is shown in Fig. 6.12e, where the portion of the radome characterized is highlighted by a red line and the spot related to the imperfection is marked in green. Two close-ups of the internal part of the radome, taken at different elevations, are also shown.

To conclude the study performed on the hemispherical part of the dry radome, the differential reflectivity and transmittance are presented and discussed. In Figs.

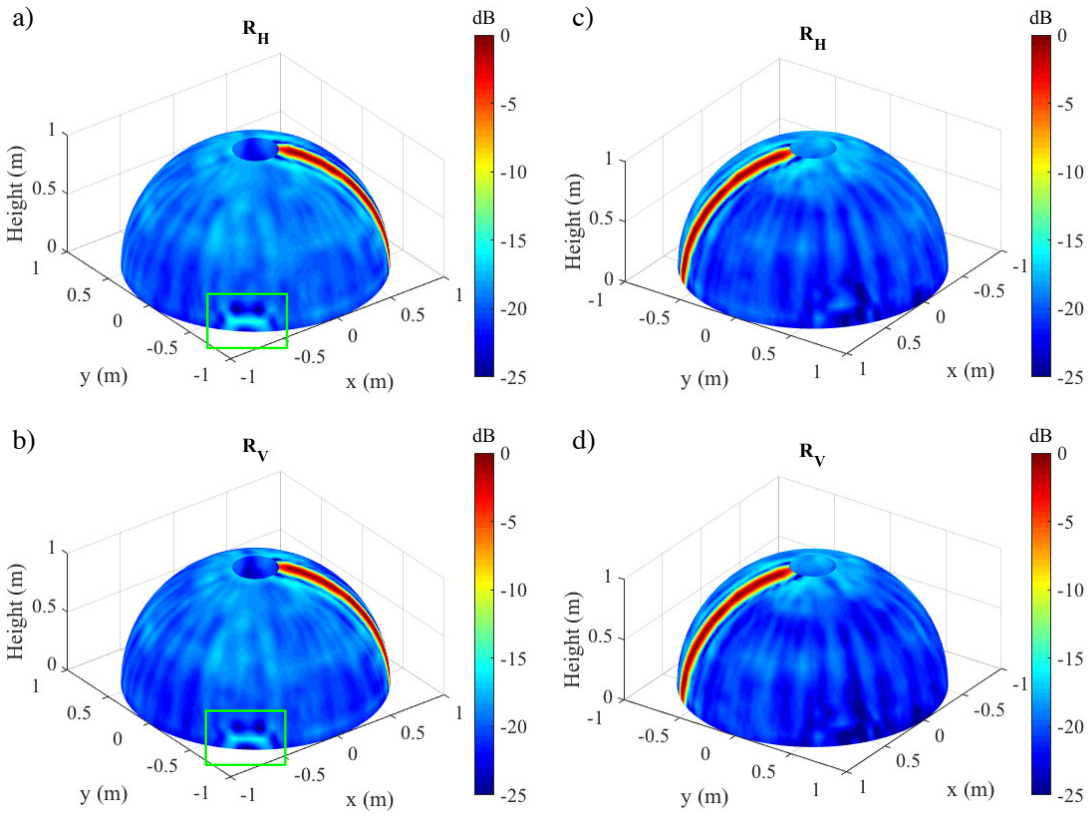

Figure 6.11: Shown is the reflectance (R) measurement for the hemispherical part of the radome in dry conditions. The top row shows the H-polarization and the bottom row presents the V-polarization. Shown in a) and b) are results for one side of the radome. Shown in c) and d) are results for the opposite side. The line marked in red represents the reflection coming from the metal strip.

6.13a and 6.13b is shown. As it can be noted from the figures, the difference between the horizontal and vertical polarization of the reflectance changes within a few centimeters in the various locations of the radome. These level of differences are within +2.5 dB and -2.5 dB and they are due to the honeycomb composition and non-homogeneities occurring in the radome locations. In particular, it is easily detectable a red spot which corresponds to +7 dB of difference in Fig. 6.13b. The reason of this large different value is a damage or flow located inside the radome.

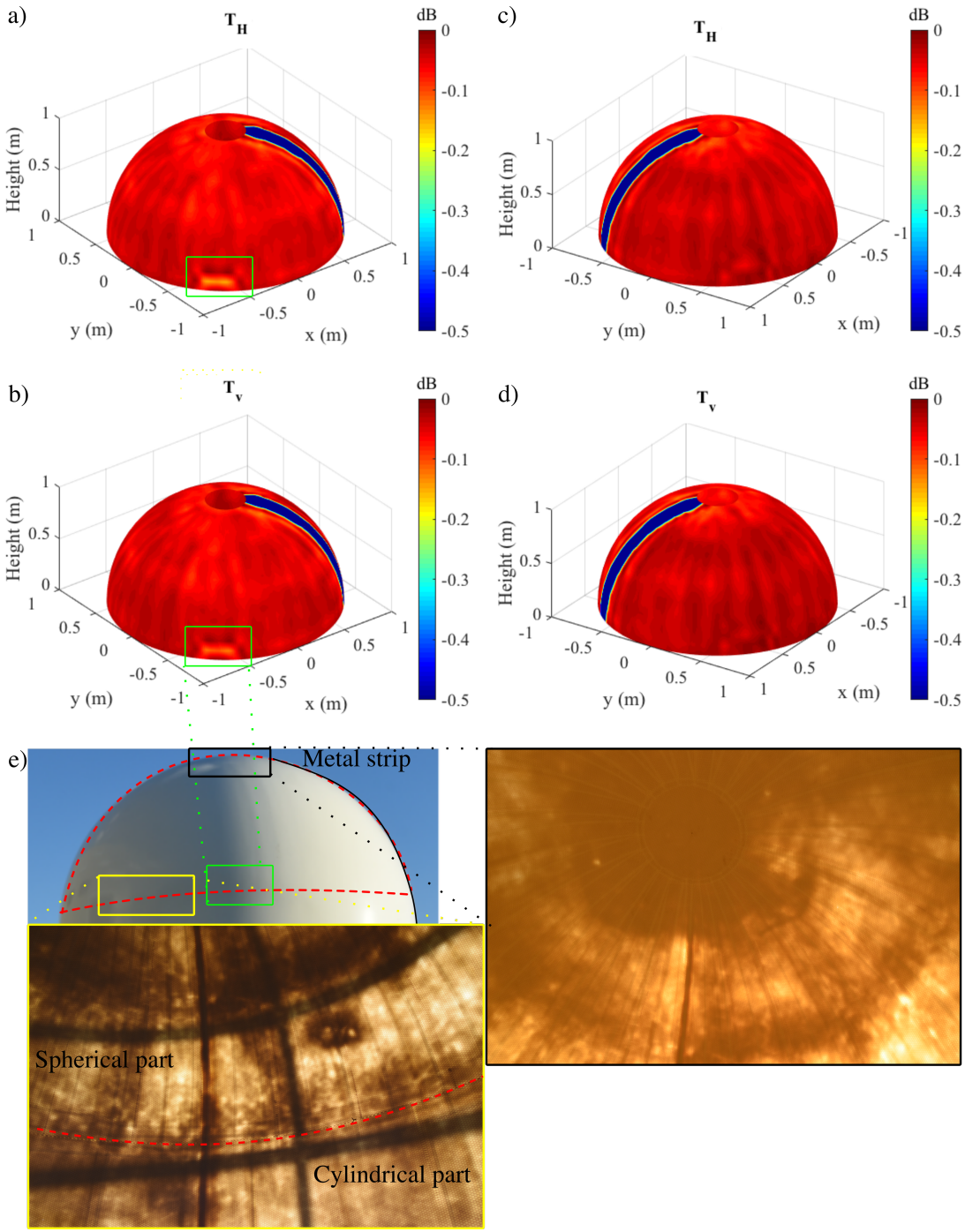

Figure 6.12: Shown is the transmittance (T), neglecting the absorption, for the spherical part of the radome in dry conditions. The top row shows the H-polarization and the bottom row presents the V-polarization. Shown in a) and b) are results for the B-side of the radome. Shown in c) and d) are results for the A-side (opposite side). Shown in e) are photographs of the radome from outside, and two close-ups of the internal view.

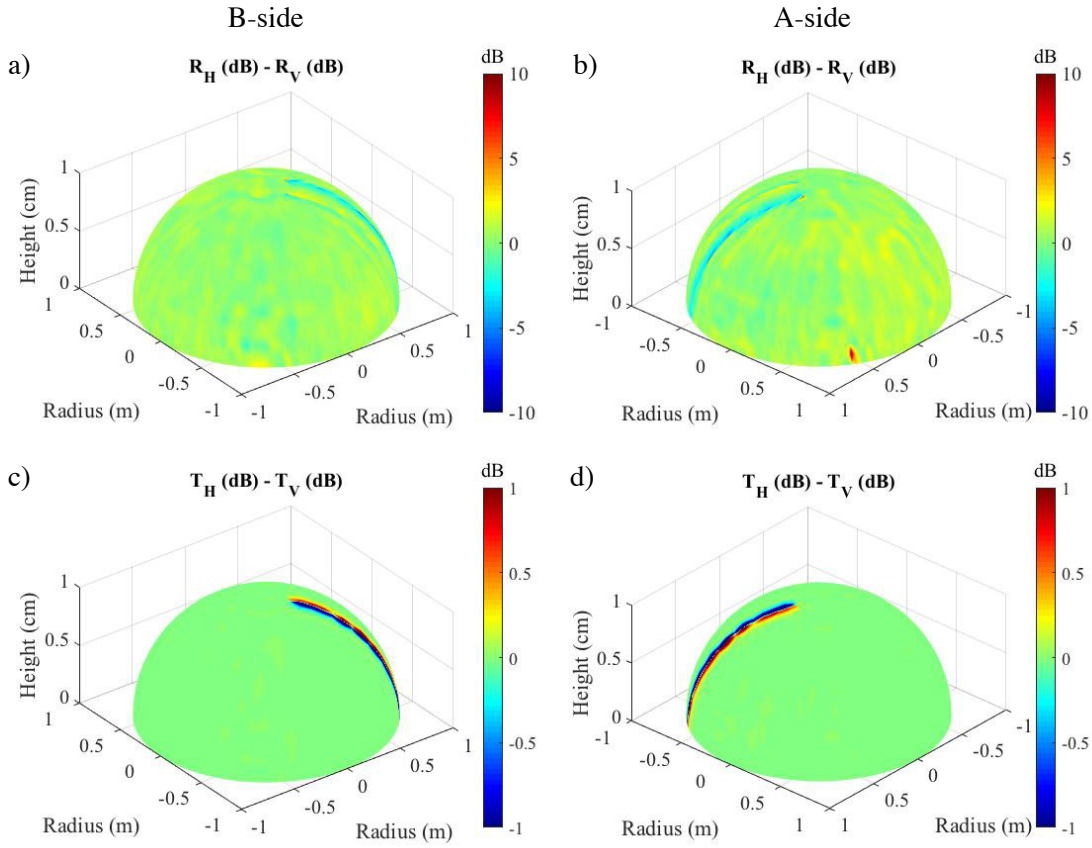

Figure 6.13: Shown is the difference between the H- and V-polarizations for the reflectance (R) and transmittance (T) for the measurements performed for the hemispherical part of the radome in dry conditions. a) and b) Results for the differential reflectance for the A- and B-side of the radome. c) and d) Results for the differential transmittance for the A- and B-side of the radome.

The results corresponding to the differential transmittance are shown in Figs. 6.13c and 6.13d. The differential transmittance presents values located within ± 0.05 dB in all the radome showing that there is no remarkable difference in the transmitted component of the signal.

6.1.4.3 Case 3: Semi-Spherical Radome under Artificial Rain

A common garden sprinkler was employed to produce artificial rain. No rain rate or DSD was taken into account when wetting the radome. As a result of the consistent

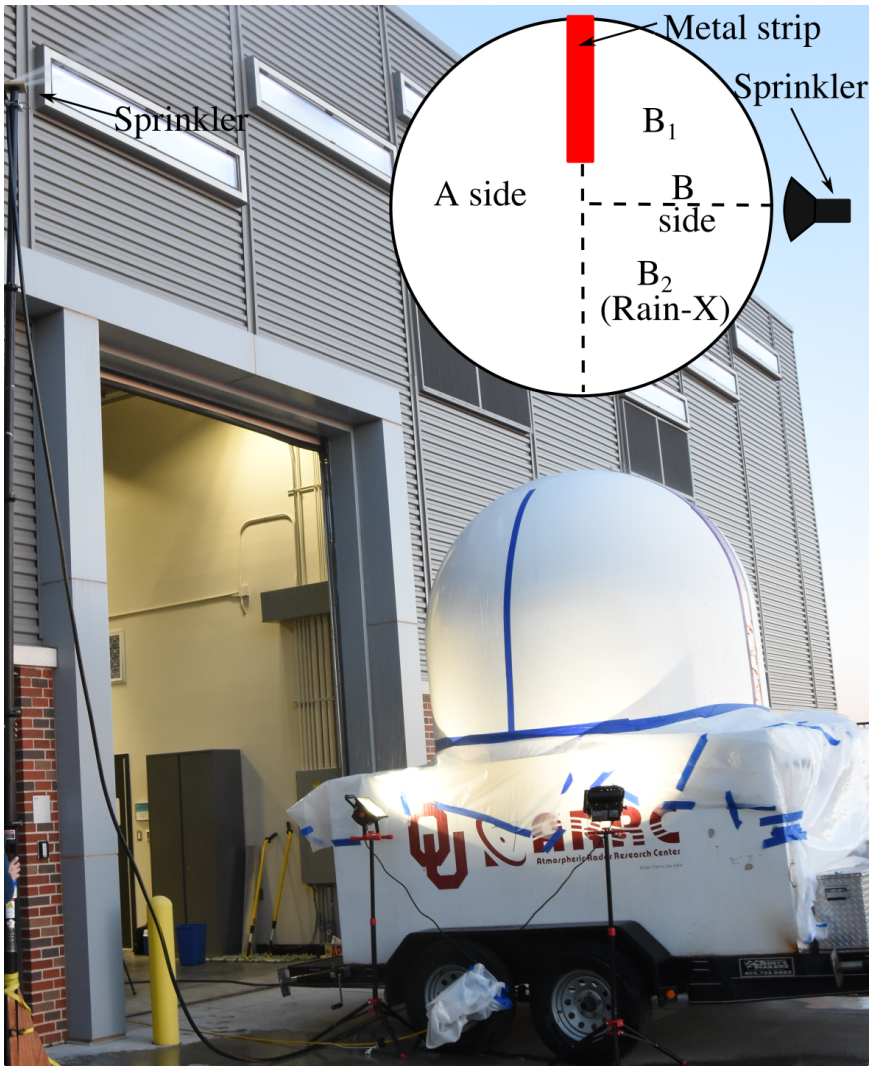

Figure 6.14: A photograph taken during the X-band radome characterization under artificial rain. At the top right, is a schematic representation (top view) of the radome subdivision (not on scale).

flow of water through the sprinkler, the artificial rain was fairly uniform over time, except for the impact of the wind. The purpose of this test is to evaluate the effect of a continuous intense rain over the radome. In Fig. 6.14, a photograph shows the rain setup used for this experiment. The setup was designed with the sprinkler pointing at the top of the radome so that the water stream could flow down naturally and equally on both sides. The schematic representation depicted at the top right

of Fig. 6.14, shows a top view of the radome and the related sector subdivisions called A- and B-sides. B-side directly faces the sprinkler. Although the water flow was supposed to hit the radome from the top, wind action caused uneven water distribution on the radome. As a consequence of the wind, it was predicted that the A-side would be less exposed to the rain than the B-side. B_2-side, a subsection of B, is the sector where Rain-X was applied.

The following test under artificial rain conditions was performed on February 25^{th}, 2016, the same day that Rain-X was applied to the radome. A comparison between A-side and B_2-sector is shown in Fig. 6.15. The photographs were taken during the experiment using artificial rain, and show a comparison between the part of the radome not treated with the Rain-X and the area where it was applied. Only the B_2-sector presents droplets, while on the rest of the radome, a water film of varying thicknesses was formed. Different thickness of the water film may occur as a consequence of the wind presence, because one portion of the radome might not be exposed to the same rain intensity as another part. However, in this case, the "wavy" pattern of the film shown in Fig. 6.15f, is due to the fact that when a critical thickness is reached, water just runs off, producing "wavy" behavior (Ruze 1965). In the photograph, droplets and rivulets on the the B_2-side are highlighted. In Fig. 6.15a, the Rain-X effect is shown. In the portion of the radome where the Rain-X was applied, the water remains as droplets or rivulets, while it stays as a film on the rest of the radome. In Fig. 6.15b, another photo emphasizes the A-side, showing that the water film is not homogeneous, but actually appears "wavy" (close-up in Fig. 6.15f). The top part of the subdivision B_2 was not treated with the hydrophobic

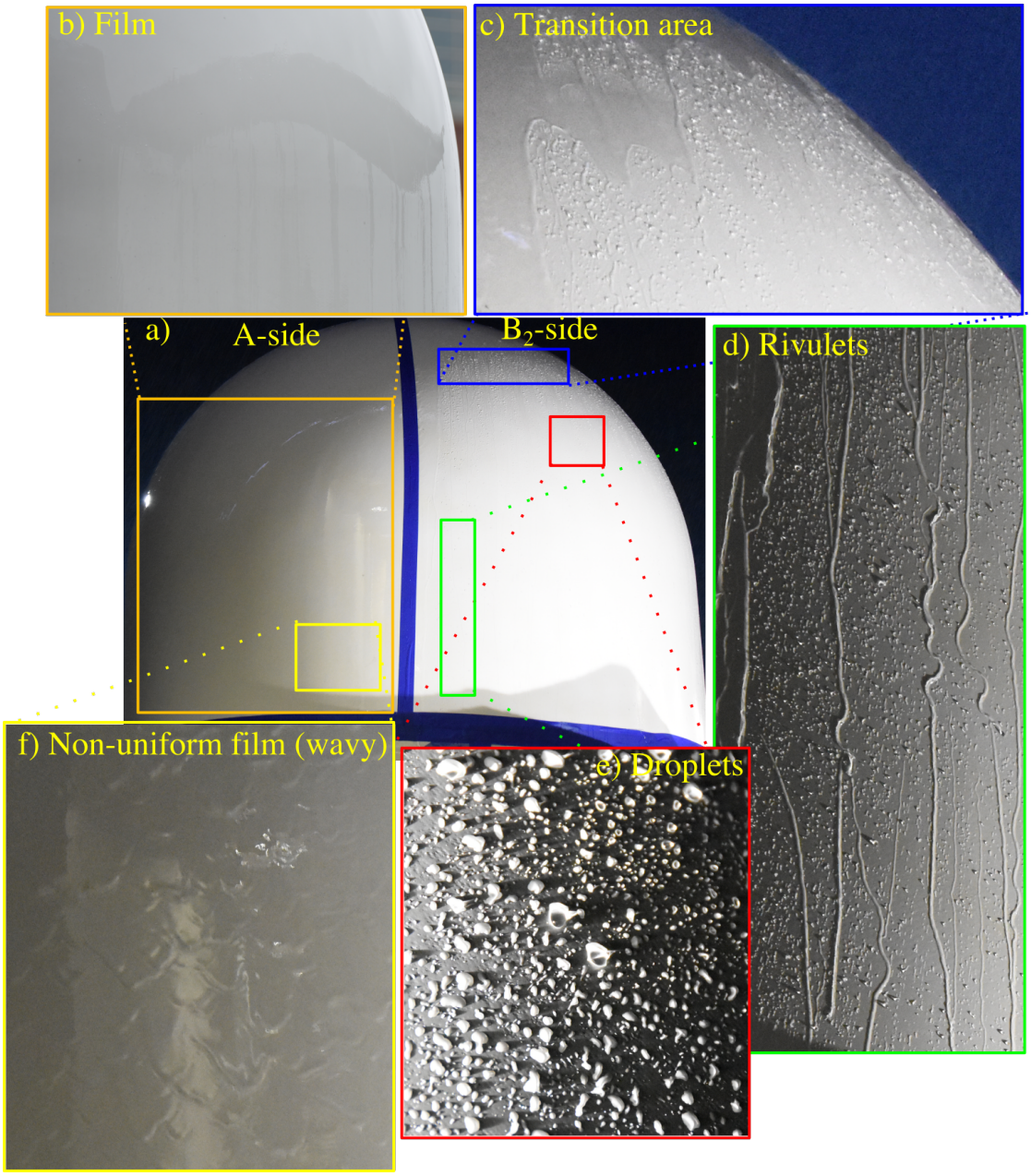

Figure 6.15: a) A photograph that shows the Rain-X effect on the X-band PX-1000 radome during artificial rain. A comparison of the water distribution between A-side and B_2-sector are shown in close-ups b) and e). The boundary where Rain-X was applied is shown in c). A close-up of the A- and B_2-sides showing the rivulet formations, and the continuous but non-homogeneous film, are shown in d) and f).

substance because it was not possible to be physically reached. Consequently, at the top of this sector, the water distributes as a film, like the other untreated areas of the radome. This is confirmed in the close-up in Fig. 6.15c, where the distinction between the part of the radome where the Rain-X was applied, and the top portion without Rain-X, is obvious. In Fig. 6.15d and 6.15f, two close-ups of the B_2-side are shown. In these, the droplet and rivulet formations due to the Rain-X effect are highlighted.

The measured reflectance is shown in Fig. 6.16. It is noticeable the level of reflection increased as a results of the heavy rain (Fig. 6.16c and 6.16d). For such an area, the level of reflection increases from -20 dB in dry condition, to -6 dB for the wet case. Fig. 6.16a presents the reflections for the H-polarization for the sector treated with the Rain-X (B-side). Reflections are lower (below -10 dB) at the bottom of the hemisphere and higher (-6 dB circa) at the top part of the hemisphere, where Rain-X was less efficient. However, the transition between -6 dB and -15 dB reflectance, visible in Fig. 6.16a, does not match with the elevation corresponding to the top border where Rain-X was not applied. This value of the transition of the reflectance is probably more due to the large stream of water occurring at the top of the B-side, the region where the sprinkler was directly wetting the radome, than it is to exposure to a higher quantity of water (Fig. 6.14). The hydrophobic effect at that elevation was nullified. There is a noticeable difference between R_H and R_V in the sector treated with the hydrophobic substance. Water stays mostly as droplets and rivulets on hydrophobic surfaces. Rivulets, have a vertical geometry, which gives them a larger vertical cross-section than a droplet, while the horizontal cross-section

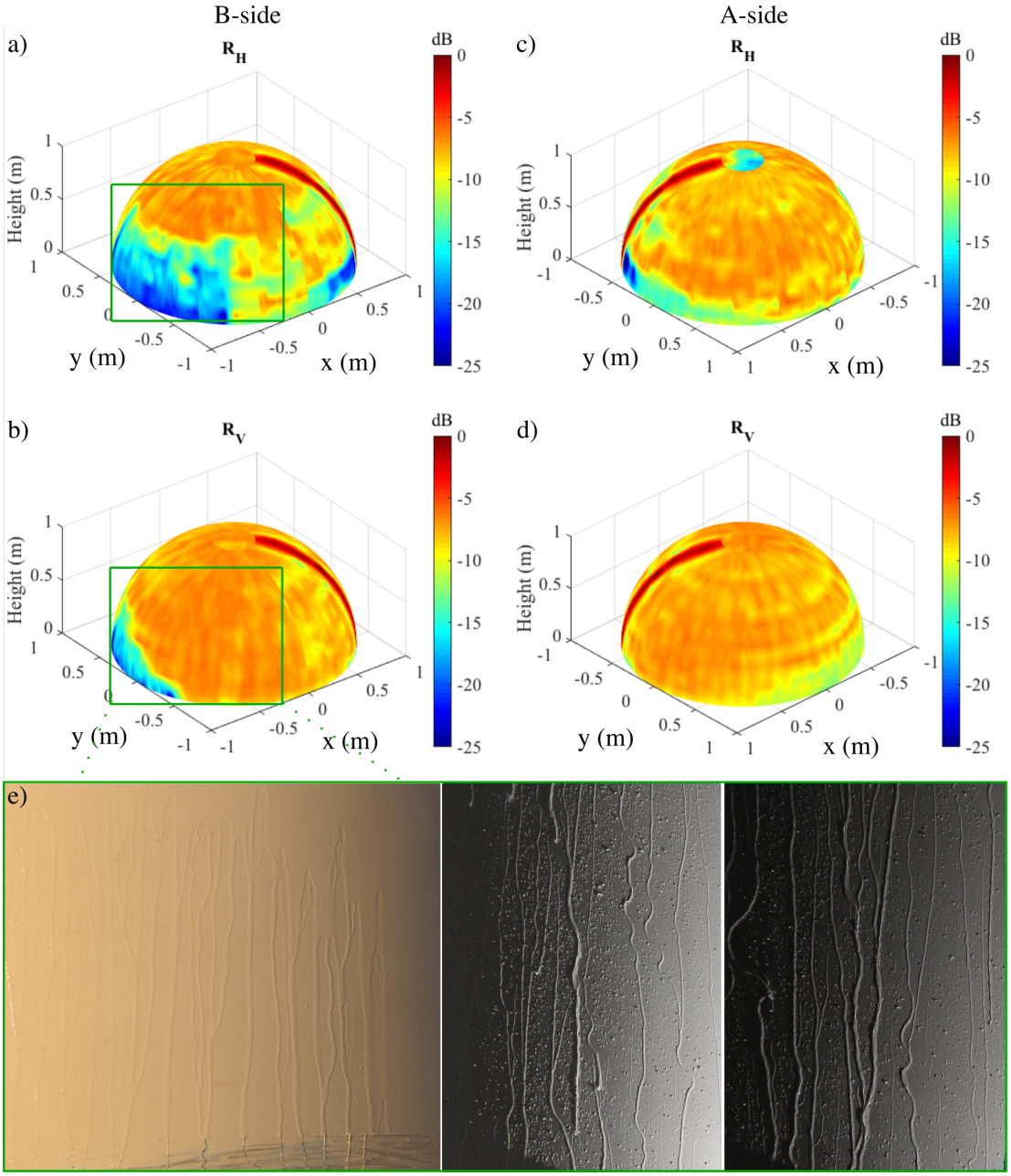

Figure 6.16: Shown is the reflectance (R) measurement for the spherical part of the radome in wet conditions during artificial rain. The top row shows the H-polarization and the bottom row presents the V-polarization. Shown in a) and b) are results for B-side of the radome. Shown in c) and d) are results for the A-side (opposite side). The line marked in red represents the reflection coming from the metal strip. Shown in e) are photographs of rivulet formation occurring on the B_2-side.

is the same as a droplet. This is highlighted in the photographs shown in Fig. 6.16e. In this way, a rivulet reflects more an electromagnetic wave polarized vertically than one polarized horizontally. When water presents as a film (non-hydrophobic portion), there is no remarkable difference between H- and V-polarizations. This is confirmed by the comparison of Fig. 6.16a and 6.16b, where the reflectance is higher for R_V than R_H, for the B-side (which part treated with hydrophobic substance).

The estimated transmittance is not available because no rain rate was measured at the time of the experiment. Furthermore, even if the rain rate was measured, the sprinkler did not wet the radome in a uniform way for the reasons mentioned earlier. This makes the absorption hard to compute since the water, either as a film or as droplets/rivulets, was highly non-homogeneous (Figs. 6.15 and 6.16e). As a consequence, the authors chose not to show the transmittance. However, the results of this scenario are still interesting because they highlight the effects of different water formations caused by a very intense stream of water. These two factors show how the level of reflectance is higher compared to the level of reflection of the dry radome. Various levels of attenuation for the two polarizations are expected, not only in the sector where Rain-X was applied, but also on the rest of the radome, as Figs. 6.16c and 6.16d demonstrate.

In Fig. 6.17, the differential reflectivity is shown for the scenario of the radome under artificial rain. It is important to mention that because, the tests were not performed with a dual-polarized probe, the measurements of the radome in wet conditions for one polarization and then for the other one, were not done simultaneously, as already explained earlier in the text. Therefore, showing the differential

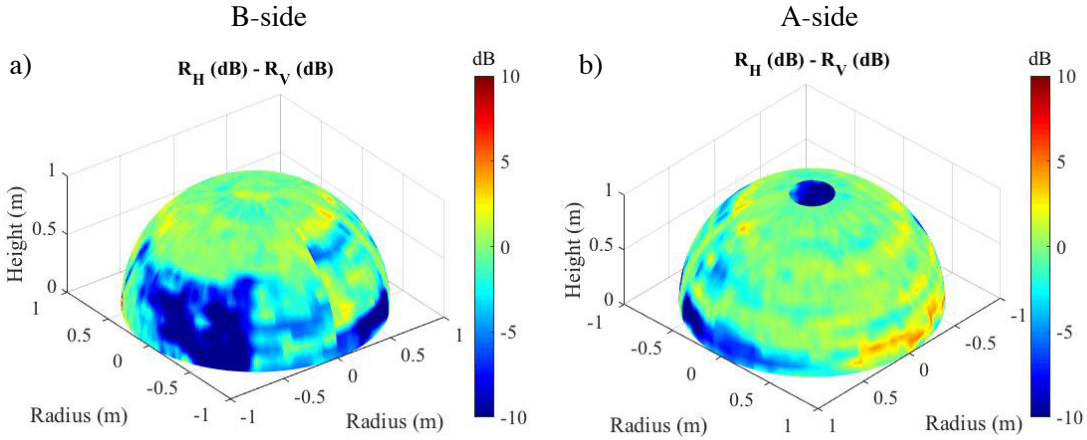

Figure 6.17: Shown is the difference between the H- and V-polarizations for the reflectance (R) for the measurements performed for the hemispherical part of the radome under artificial rain. a) and b) Results for the differential reflectance for the A- and B-side of the radome.

reflectivity for this experiment is not realistic. However, these results still provide an idea of how the reflectance measured in both polarizations can be different, especially because the rain was produced with a sprinkler, which rain rate was constant beside the presence of the wind that could alter the amount of water falling on the radome. Fig. 6.17a shows in the area where Rain-X was applied a remarkable difference because the presence of rivulets. The differential reflectance in that area changes abruptly from -10 dB to +2 dB. In Fig. 6.17b, the film formation does not seem to be uniform along the two polarizations. This is probably due to the fact that a heavy rain was generated, and then the film formation was "wavy" (Fig. 6.15f). The film pattern generates a differential reflectivity which ranges from -2.5 dB to +2.5 dB.

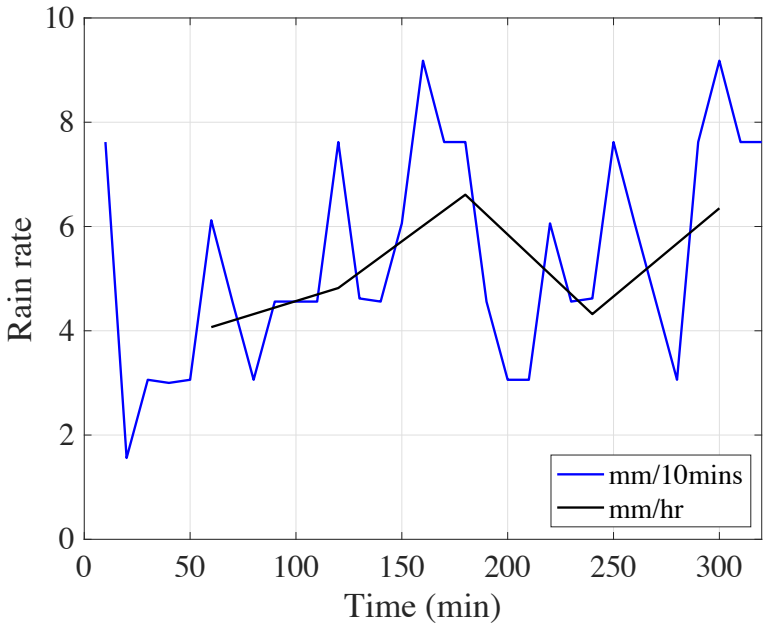

Figure 6.18: The average rain rate as function of time, during the storm occurring on April 17, 2016. The x-axis represents the relative time with respect to the beginning of the measurement. H-polarization was measured first and it started at minute 0. V-polarization was taken immediately after the end of the previous test (minute 150 circa). The average is calculated every 10 and 60 minutes. The rain rate information is provided through rain gauge from Mesonet (http://www.mesonet.org), the weather station is located within 200 m of the experiment location.

6.1.4.4 Case 4: Semi-Spherical Radome under Natural Rain

This test was performed on April 17^{th}, 2016, in Norman, Oklahoma. The measurements started at 19.10 local time. The rain rate was not uniform across the time span when the measurements were executed. The radome was first characterized with the probe horizontally polarized and then with the probe vertically polarized. During the time lapse, which lasted from the beginning of the test for the first polarization, to the end of the second polarization experiment, different rain rates could have occurred. Fig. 6.18 shows the rain rate averaged every 10 minutes. The minute 0 in Fig. 6.18, corresponds to the beginning of the experiment (7.10 PM).

Results of the natural rain test are presented in Fig. 6.19 for the reflectance. Although the Rain-X was not reapplied for this experiment, its effects were still present from the application in February (Fig. 6.19a and 6.19b). In contrast to the test results from the artificial rain, natural rain results were similar for both polarizations for the B_2-side. This is probably because the rain flow was more uniform, and the rain rate was lower than in the case of the artificial rain. The Rain-X presence is more accentuated in this scenario as demonstrated in Fig. 6.19a and 6.19b. This is in contrast to the results from the other side of the radome (Fig. 6.19c and 6.19d). Also, it is noticeable at $\theta \cong 80°$, that the reflectance is higher than at lower elevations. This occurs without distinction among the sectors' subdivisions. In fact, at such elevations, the component of the gravity force is smaller than at lower elevations, causing the water to stay more agglomerated and in bigger drops, as discussed in Salazar et al. (2014). A pattern of horizontal rings is detected on the A-side of the radome (Fig. 6.19), where water distributed as a continuous film. It occurs at various intensities at different polarizations. The rain intensity could have changed during the experiment, however, the pattern of horizontal rings looks consistent and constant in azimuth, therefore it should not be associated with rain rate changes.

The transmittance calculated by using Eq. 4.21 is shown in Fig. 6.20. The purpose of presenting these results without correcting for absorption is to show how large is the absorption effect introduced by water. This also shows how large errors can be introduced if absorption is neglected.

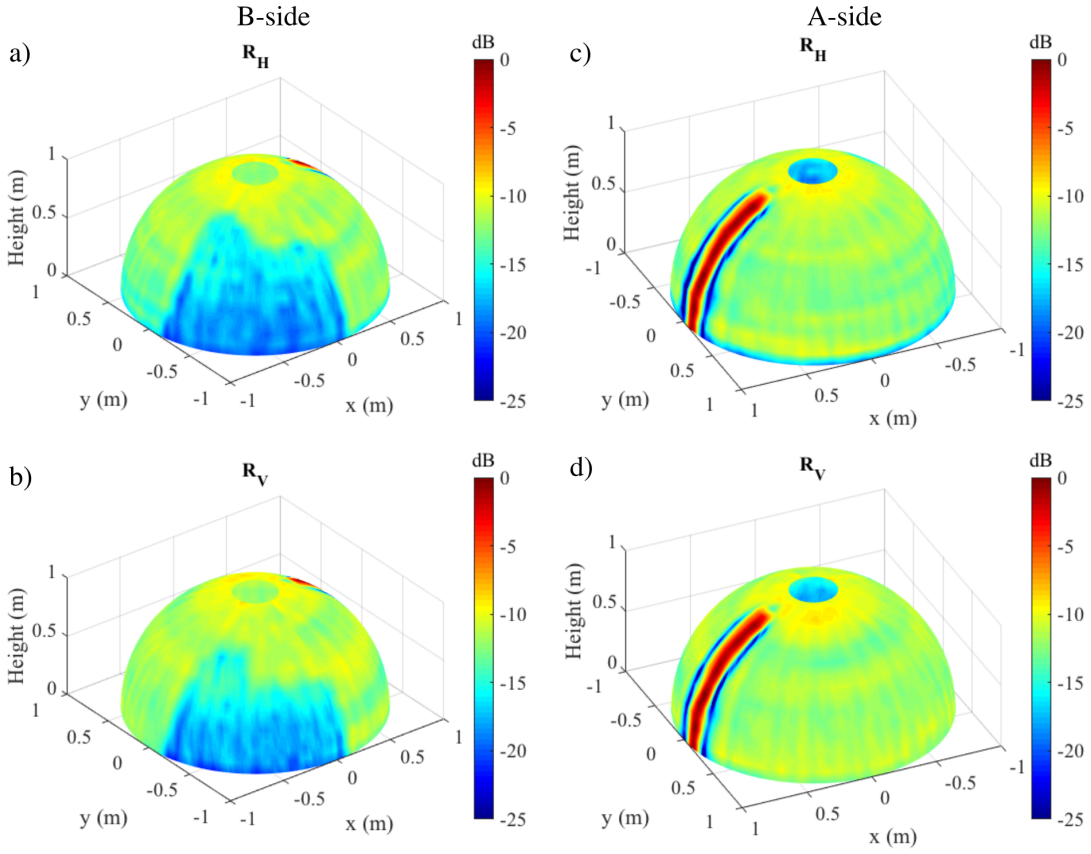

Figure 6.19: Shown is the reflectance (R) measurement for the spherical part of the radome in wet conditions during natural rain. The top row shows the H-polarization and the bottom row presents the V-polarization. Shown in a) and b) are results for the B-side of the radome. Shown in c) and d) are results for the A-side (opposite side). The line marked in red represents the reflection coming from the metal strip.

The estimated transmittance is shown in Fig. 6.21. Since the rain rates were available every 10 minutes, as reported in Fig. 6.18, and the azimuth scan lasted approximately 9 minutes, it was hard to make a precise correspondence between the azimuth scan and the related rain rate. Therefore, the transmittance was estimated based on the hourly rain rate (Fig. 6.18). It follows that for the H-polarization test, from 0° - 25° elevation, the rain rate of 4 mm h^{-1} was used for the correction. From 30° - 60°, 5 mm h^{-1} was used to make the correction. 6.6 mm h^{-1} rain rate was used to estimate the absorption from 65° - 80°. For the experiment performed

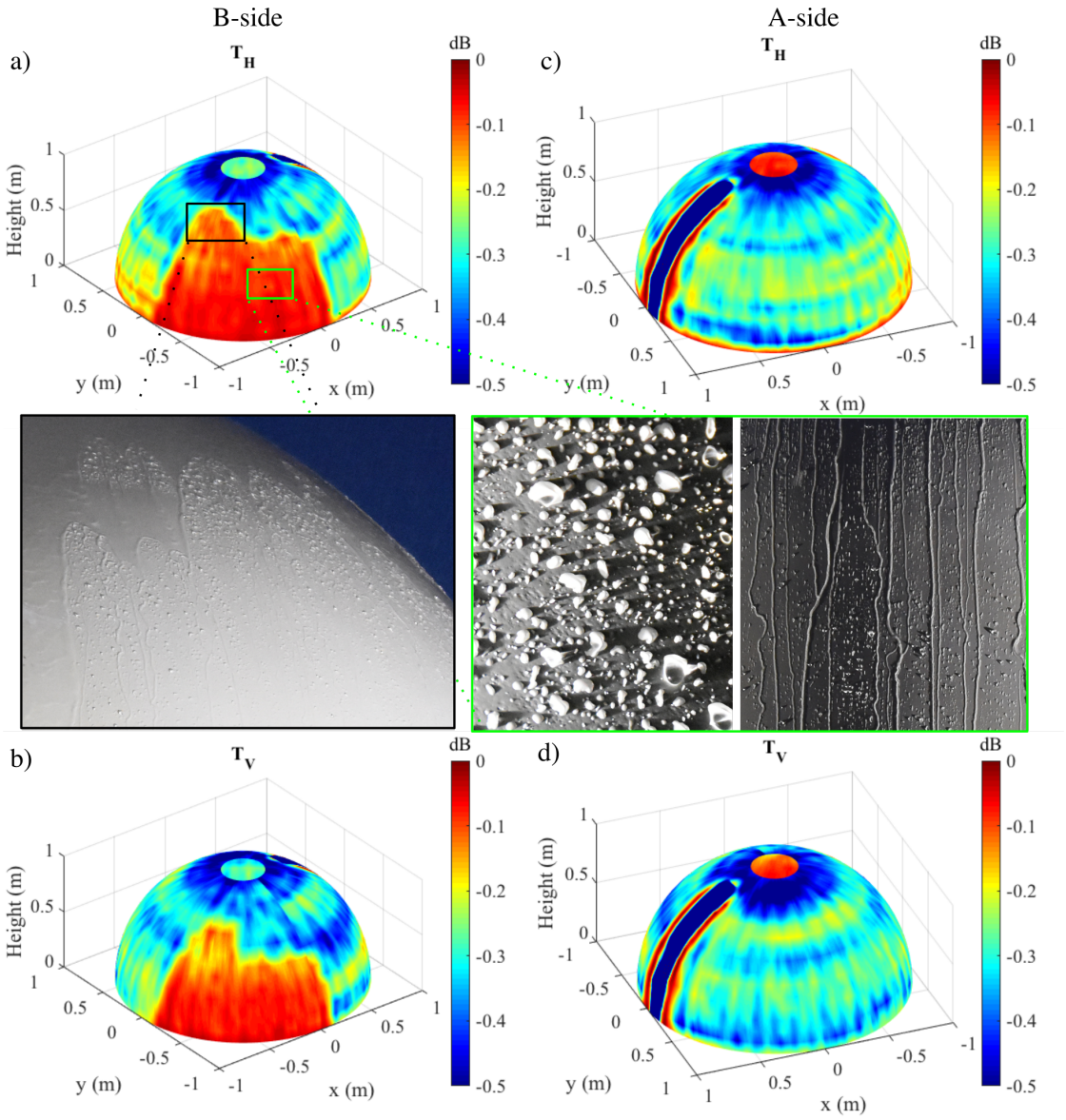

Figure 6.20: Shown is the transmittance (T) without applying the correction algorithm, for the hemispherical part of the radome in wet conditions during natural rain. The top row shows the H-polarization and the bottom row presents the V-polarization. Shown in a) and b) are results for the B-side of the radome. Shown in c) and d) are results for the A-side (opposite side). Photographs of the positions identified by the red frame insets shown in figures a) and b) highlight the rivulets and droplets.

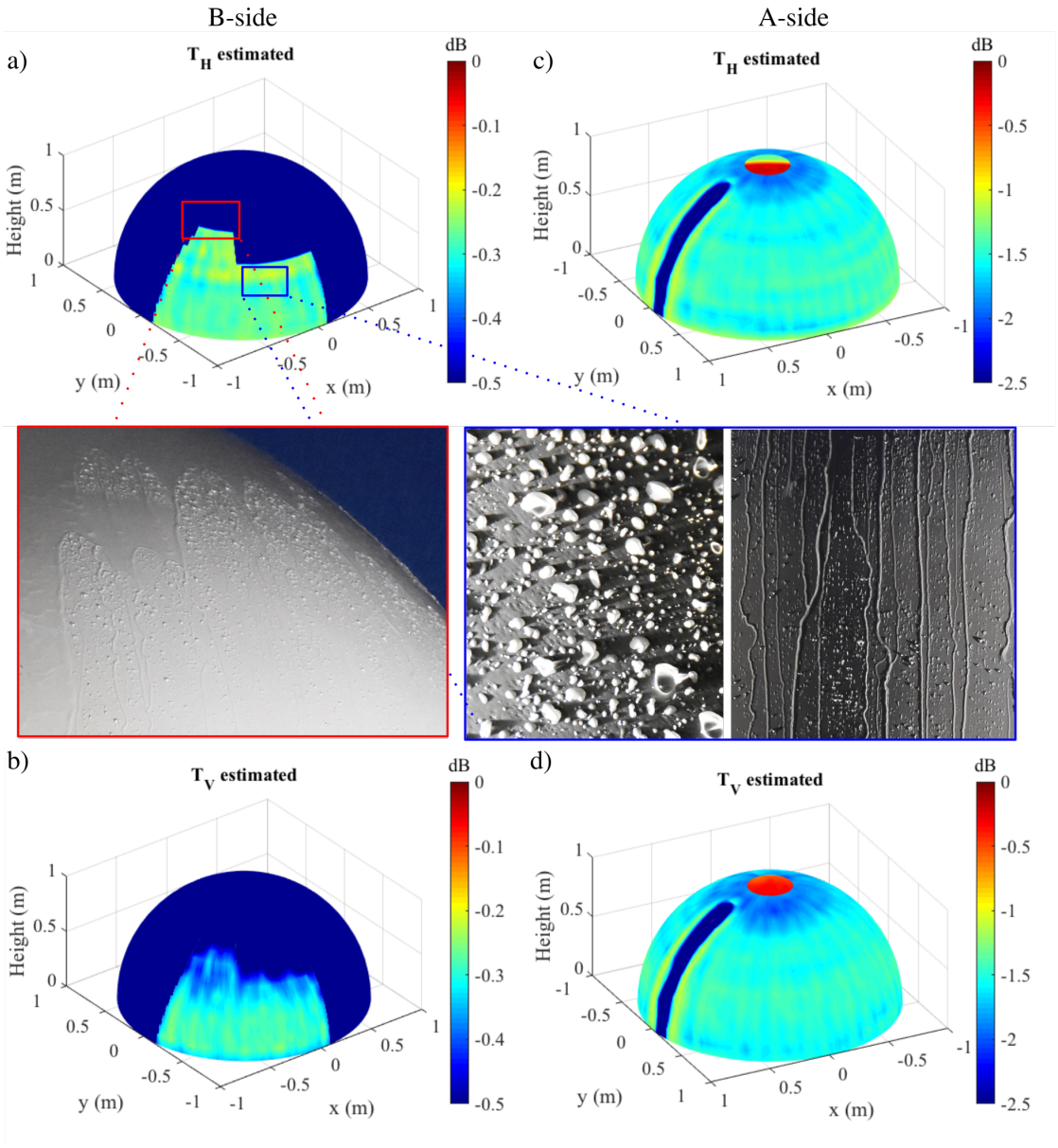

Figure 6.21: Shown is the estimated transmittance (T), for the hemispherical part of the radome in wet conditions during natural rain. The top row shows the H-polarization and the bottom row presents the V-polarization. Shown in a) and b) are results for the B-side of the radome. Shown in c) and d) are results for the A-side (opposite side). Photographs of the positions identified by the red frame insets shown in figures a) and b) highlight the rivulets and droplets.

with the probe vertically polarized, which began immediately after the previous experiment (minute 150 in Fig. 6.18), the rain rate of 6.6 mm h^{-1} was used to make the correction in the range 0° - 15°. 4 mm h^{-1} was employed to make the correction in the range 20° - 45°. A rain rate of 6.6 mm h^{-1} was used to make the correction in the 50° - 80° elevation range. In the radome portion shown in Fig. 6.21a and 6.21b, the formation of the droplets was considered in estimating the transmittance, while the continuous film formation was used to make the estimation of the transmittance in the remainder of the radome. Procedures to estimate the transmittance of the the two different water distributions were discussed in (Mancini, Salazar, Lebrón and Cheong 2018*b*; Mancini et al. 2017). Two different scales were necessary to represent the transmittance in the two sides of the radome, because the level of absorption was different. Specifically, levels of absorption were higher where water was distributed as a film than where it was distributed as droplets. The B-side of the radome, for both polarizations where droplets and rivulets occurred, is presented in Fig. 6.21a and 6.21b. Two photographs, representing the close-ups highlighted on the B-side, show the radome condition. 1) Shows the transition between the Rain-X portion and the part where the hydrophobic substance was not applied. 2) Shows droplets and rivulets distributed on the B_2-side. Fig. 6.21c and 6.21d present the A-side, where water was distributed as a continuous film. Because the level of absorption was higher on the A-side than on the B_2-sector, the level of transmittance was lower and a different scale had to be used. Regarding the A-side (Fig. 6.21c), the order of magnitude of transmittance is very close to the one estimated through simulation in Fig. 5.6, for 5.3 mm h^{-1} rain rate, where -2 dB transmittance was obtained.

The difference of estimated transmittance between Fig. 5.6 and Fig. 6.21c, is probably due to the fact that in the real case, the water formation was affected by wind presence and dirtiness conditions of the radome. These factors were not taken into account in the simulation. Furthermore, the vertical lines introduced in Figs. 6.11 and 6.12 are still present under natural rain (Figs. 6.19 and 6.21). Those lines, which nature is unknown to the author, were not taken into account in the simulation. The above mentioned vertical lines, are also present in the artificial rain results (Fig. 6.16), but they are less visible (almost hidden) probably because the thicker film of water occurred in that scenario.

The results for the differential reflectance and transmittance are shown in Fig. 6.22. As for the case analyzed under artificial rain, showing results for differential reflectance and transmittance is not a fair comparison because the time lag occurred between the two measurements, although the rain rate did not show any large change during the experiments (Fig. 6.18). It is still interesting to take a look to the differential reflectance and transmittance despite the reasons discussed. The figure shows that the change in differential reflectance for the the portion of the radome where Rain-X was applied (Fig. 6.22a), is not as large for the case of artificial rain. In fact, for this scenario the differential reflectance present peak values of +3 dB and minimum of - 8 dB. For the reminder of the radome containing film formation (Fig. 6.22b), the differential reflectivity is more uniform. It changes from +3 dB to -3 dB.

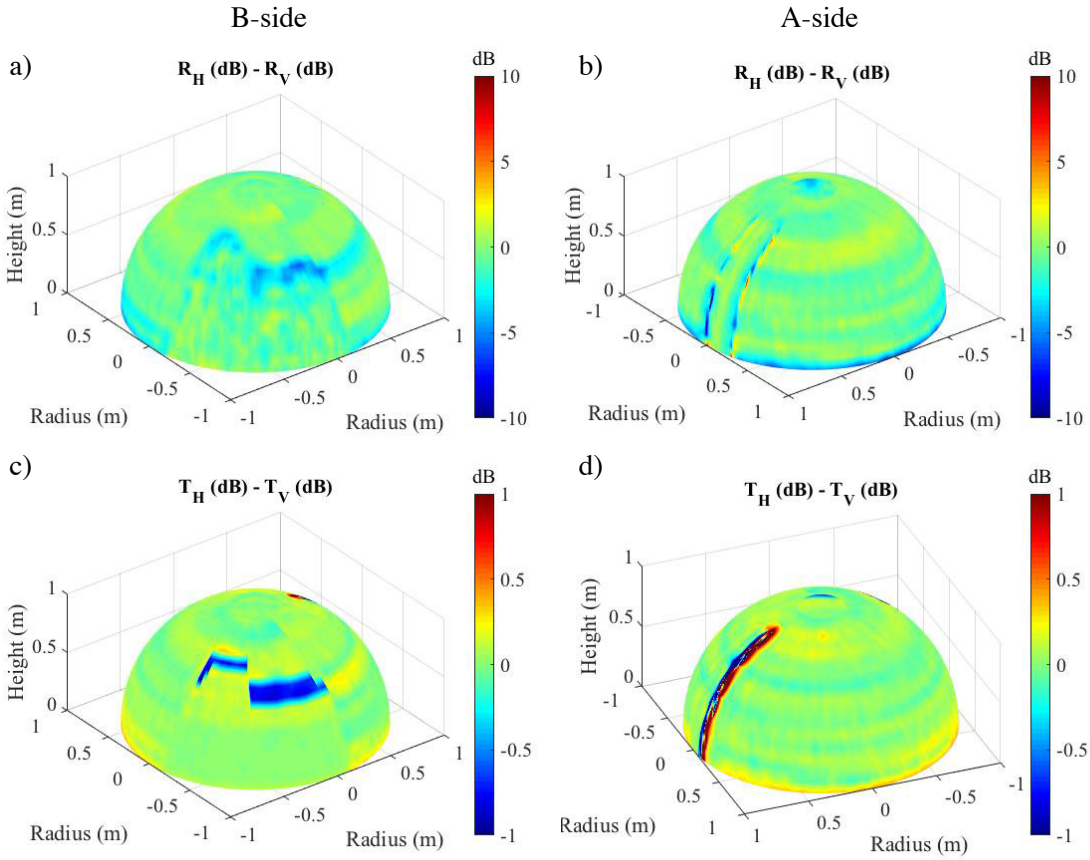

Figure 6.22: Shown is the difference between the H- and V-polarizations for the reflectance (R) and transmittance (T) for the measurements performed for the hemispherical part of the radome under natural rain. a) and b) Results for the differential reflectance for the A- and B-side of the radome. c) and d) Results for the differential transmittance for the A- and B-side of the radome.

The results for the differential transmittance are shown in Figs. 6.22c and 6.22d. The location that shows the largest change in differential transmittance is the transition between the radome portion where Rain-X was applied, and the top part. Here, a value of -0.8 dB was measured. In the reminder of the radome the differential transmittance changed from -2.5 dB to +2.5 dB. There results show that in case of low rain, the reflectance and transmittance show moderately low variations in the two polarizations.

6.2 Near-Field Radome Characterization

Although radome characterization is commonly performed in far-field, in practical situations, water is located on the outer surface of the radome, which is in the near-field region of the radar antenna. Therefore, to more realistically evaluate the antenna performance with water accumulated on the radome, a different approach was chosen. The method consists of measuring the radiation pattern of a 8 x 2 LRU antenna array in a near-field anechoic chamber. With this method, it was possible to characterize the impact of water located in the near-field region of the antenna, on the far-field radiation pattern. The antenna array employed for this experiment was a prototype of a dual-polarized 8 x 8 S-band radar antenna array (Díaz et al. 2016), with only the 8 x 2 subarray being fed. A photograph of the near-field setup, including the active array, is shown in Fig. 6.23.

Tests were performed both in dry and wet conditions, for H- and V-polarizations, at the steering angles of -30°, 0°, and 30°. For the wet cases, different scenarios were considered. These scenarios included droplets randomly distributed, vertically aligned droplets, rivulets, and a partial film. To keep water in a steady position during the whole near-field measurement, an ordinary bubble plastic packing material was used. This solution allowed placing water in the various areas of the active subarray without having the measurements affected by the plastic support. To prove that the wrapping plastic (without water), does not introduce any bias in the near-field tests, a comparison of the radiation patterns measured with and without the plastic is presented in Fig. 6.24. The figure shows that the plastic does not

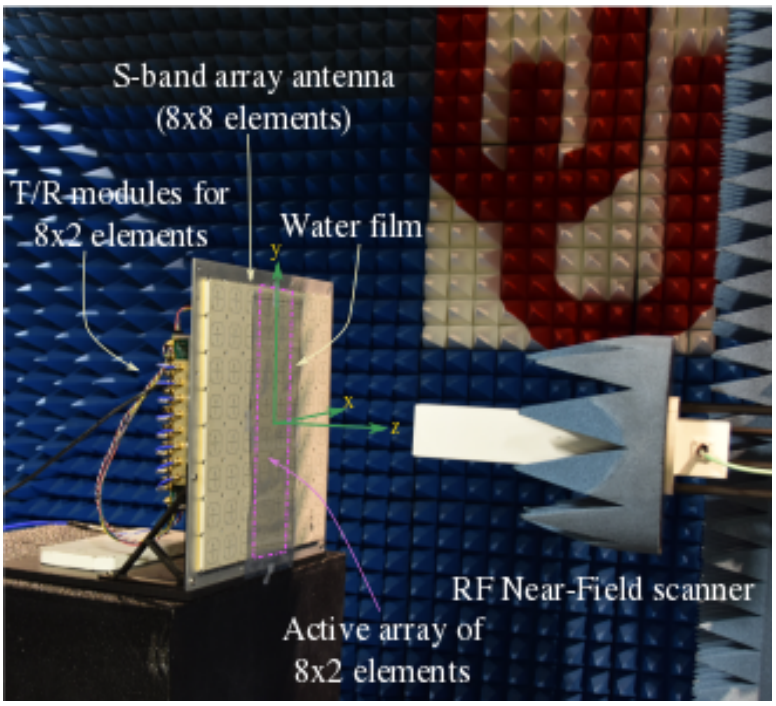

Figure 6.23: A photograph of the 8 x 8 LRU antenna array employed for the near-field measurements with the water film placed on the radome. In the figure, it is also highlighted the active array composed of 8 x 2 elements.

introduce any effect on the far-field radiation patterns of co- and cross-polarization. Therefore, all the changes in the radiation pattern performance in the experiments presented later in this dissertation must be attributed to the presence of water.

The first experiment measured the near-field radiation pattern of the active array antenna in dry conditions. The subsequent experiments included the presence of water. To record the exact location of water, photographs of the setup were taken with an infrared camera. These are shown in Fig. 6.25. The reason for employing an infrared camera is not to determine the temperature of water, which is irrelevant for this experiment, but to highlight the areas of the 8 x 2 array that were covered with water. Otherwise, the water was not visible because it is transparent. The slight difference in temperature (2° - 3° C) between the environment and fresh water

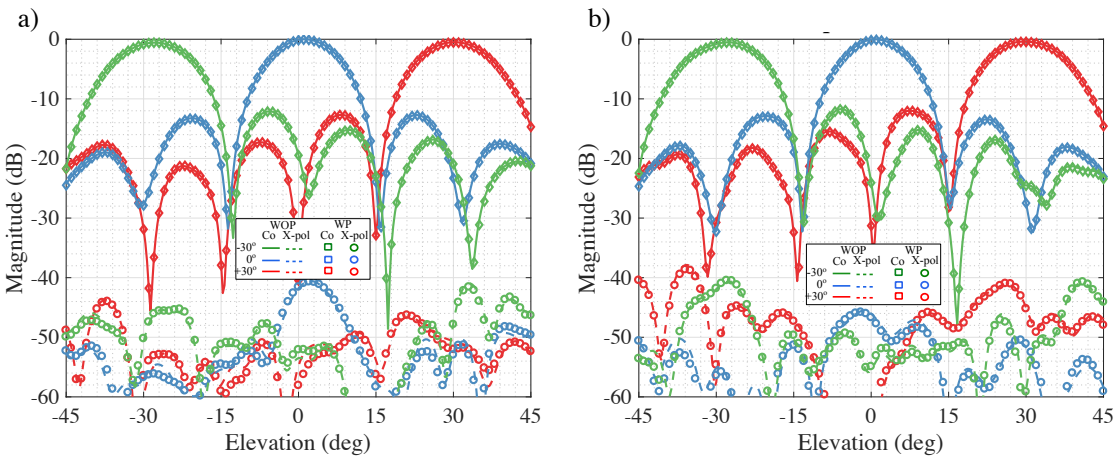

Figure 6.24: A comparison of the measured radiation patterns of the 8 x 2 array, at the steering angles of -30°, 0°, and 30°, without plastic (WOP) and with plastic (WP). a) H-polarization. b) V-polarization.

highlighted the locations occupied by water. In the second test, water was sprayed on a plastic sheet overlapped with the 8 x 2 array. The reason wrapping plastic was not used for this test was because droplets with an unrealistic diameter would have been produced. By spraying water with a thin nozzle, smaller droplets with various diameters were created. This procedure allowed replication of droplets with diameters similar to what would occur in a real situation. The water distribution obtained for this scenario is shown in Fig. 6.25a and 6.25e. By using a numerical code for imaging recognition, from a photograph of the water distribution it was possible to estimate the droplets' diameters by post-processing. Then, by knowing the diameters, the droplet residual (n_R) was computed by using Eq. 4.15. Finally, by choosing $T = 30$ s and $\Delta D = 0.2$ mm, a rain rate of 8.9 mm h^{-1} was calculated. To remain consistent with the physical meaning of θ_i (angle of projection of the radome in the direction of the rain), water was sprayed keeping the nozzle directly pointed at the front of the array. Therefore, the angle was set equal to 0° in Eq. 4.29. The third

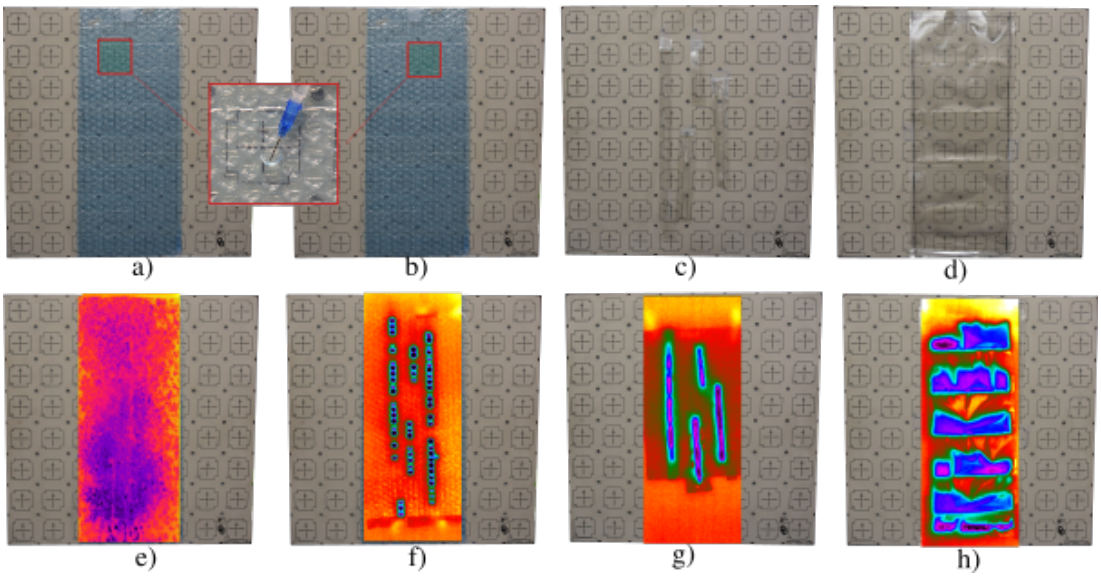

Figure 6.25: Photographs of the water placement on the 8 x 2 array antenna. a)-d) Photographs taken with an ordinary camera. e) - h) Corresponding photographs taken with the infrared camera. a) and e) Droplets. b) and f) Vertically aligned droplets. c) and g) Rivulets. d) and h) Partial water film. Shown in a close-up, the procedure of filling the bubble with water. The temperature range in the photos is 18°-24° C, with water being approximately at 19° C.

experiment considered droplets vertically aligned to reproduce rivulets, as shown in Fig. 6.25b and 6.25f. Because the packing plastic presents bubbles with spaces between them, while rivulets have a continuous geometry, the rivulets were created in a different way in the fourth experiment. To have continuous rivulets, two sheets of plastic were laminated together by using a heat gun. Then, by cutting the sheet in strips, rivulets were obtained. The strips were filled with water. Rivulets of different lengths were made, as shown in Fig. 6.25c and 6.25g. The widths and thicknesses of the continuous rivulets were about 6 mm and 1.07 mm. Unfortunately, there is no formula that allows relating the rivulet dimensions to an estimation of the rain rate. However, this test still has particular importance because it allows evaluation of the different effects vertically distributed water has in the H- and V-polarizations.

The fifth case examined was film formation. Since a film is hard to replicate, an approximate and practical solution was obtained by layering two sheets of plastic to obtain a rectangular pocket of area equal to the area of the 8 x 2 array. To assure uniform water distribution across the whole 8 x 2 array, cells were created inside the pocket. These cells allowed distribution of water all over the area equivalent to the sub-array, leaving only a few portions uncovered. Photographs taken of the water film are shown in Fig. 6.25d and 6.25h. Physical limitations of the setup employed to produce the film formation caused a lack of uniformity in the film thickness, and also did not completely fill the area of the 8 x 2 array (Fig. 6.25h). The thickness of the film ranged between 0.4 mm and 1.2 mm. The rain rate corresponding to the 0.4 mm film thickness, at 90° inclination, was 80 mm h^{-1} (Fig. 4.5). There was no real rain rate that could be associated with the film thickness of 1.2 mm. However, these results are still useful, since they can provide an idea of the effect that the water film has on the radiation pattern.

The magnitudes of the measured radiation patterns in each of the scenarios described above are compared in Fig. 6.26 and summarized in Table 6.1. The attenuation is shown in term of peak amplitude difference between each of the cases examined. The plots presenting the H-polarization (Fig. 6.26a - c) show that the co-polarization component is not affected by droplet and rivulet formation. Also, the SLL does not show an appreciable change from the dry case. A strong attenuation is noticeable instead for the water film formation, where the main beam is decreased by 10 dB, the SLL is raised, and the nulls of the radiation pattern disappeared. The biggest change in the cross-polarization component was obtained

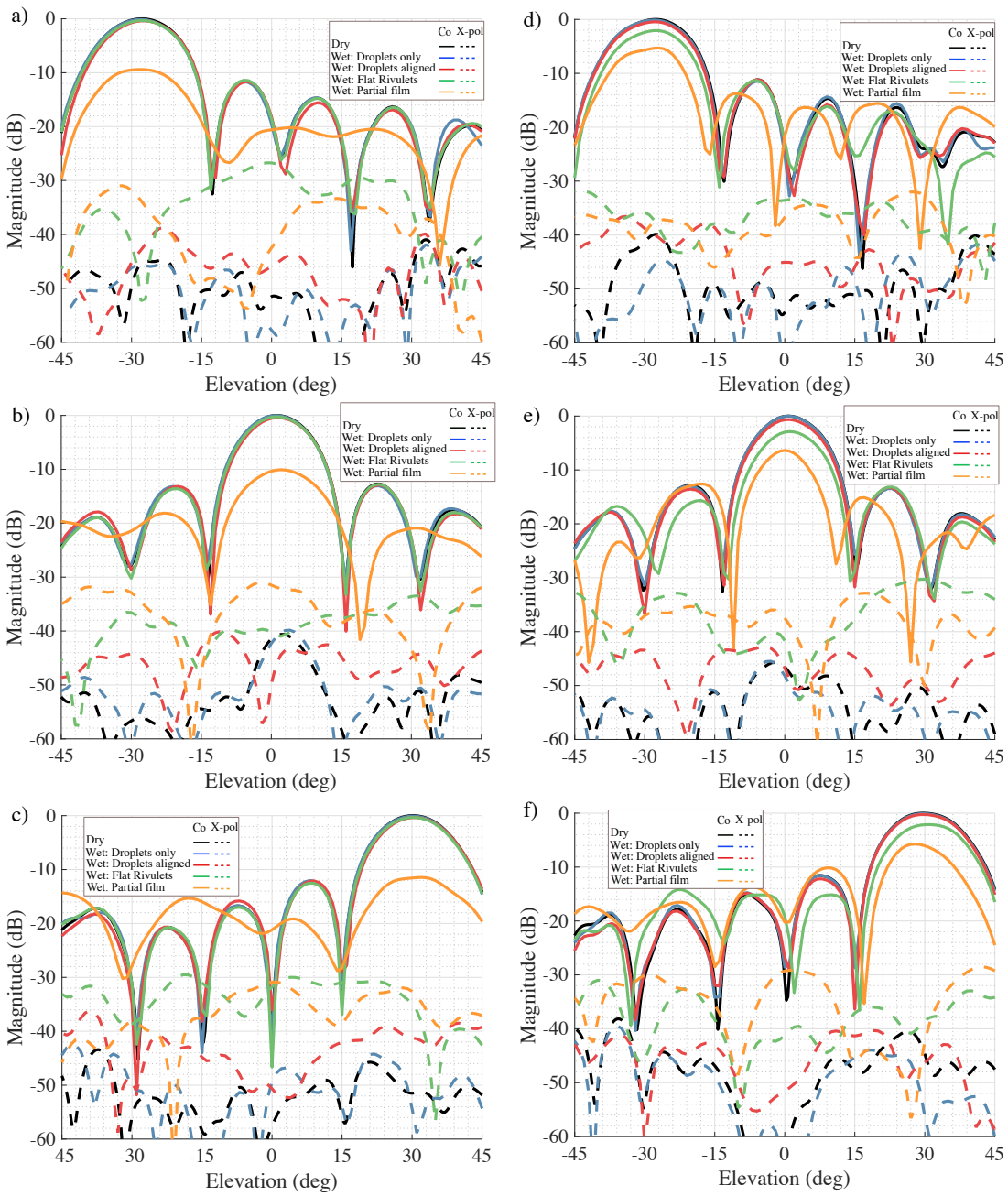

Figure 6.26: The effect of water on the magnitude of the 8 x 2 active array antenna LRU far-field radiation pattern. Results were based on near-field measurements under various conditions of the radome. a) - c) H-polarization. d) - f) V-polarization. a) and d) Beam steered at -30°. b) and e) Beam at the broadside. c) and f) Beam steered at 30°.

for the flat rivulet (green curve) case, when the beam was steered (Fig. 6.26a and c). The partial film formation generated the highest level of cross-polarization when the beam was at broadside. The sparse droplet (Fig. 6.25e) and the vertically aligned droplet (Fig. 6.25f) cases, presented similar magnitudes of cross-polarization levels, regardless of the steering angle. When the signal was vertically polarized , the four cases representing a wet radome presented different responses. Although the water film formation again produced the highest transmission loss of the co-polarization component, only an attenuation of 5 dB was noticed. However, for the V-polarization, the nulls of the radiation pattern were still visible and the SLL was less increased with respect to the H-polarization. As expected, the flat rivulet (Fig. 6.25g) introduced a higher level of attenuation (2 dB) than the H-polarization. This occurred because of their vertical geometry. The flat rivulets generated a 3-dB attenuation when the beam was at broadside. Vertically aligned droplets (red curve) generated higher attenuation when the signal was vertically polarized than in the H-polarization, although the difference between the two was not large. The level of cross-polarization for the vertically aligned droplet and sparse droplet scenarios was comparable. The flat rivulet and film cases generated almost the same level of cross-polarization.

Results for the phase are shown in Fig. 6.27. The largest phase shift with respect to the dry scenario, occurred for the water film case. For laminar flow, the phase shift was pretty constant at each steering angle considered. It ranged from a minimum of 20.16° for the H-polarization with the beam at the broadside, to a maximum of 23.14° for the V-polarization at a 30°-steering angle.

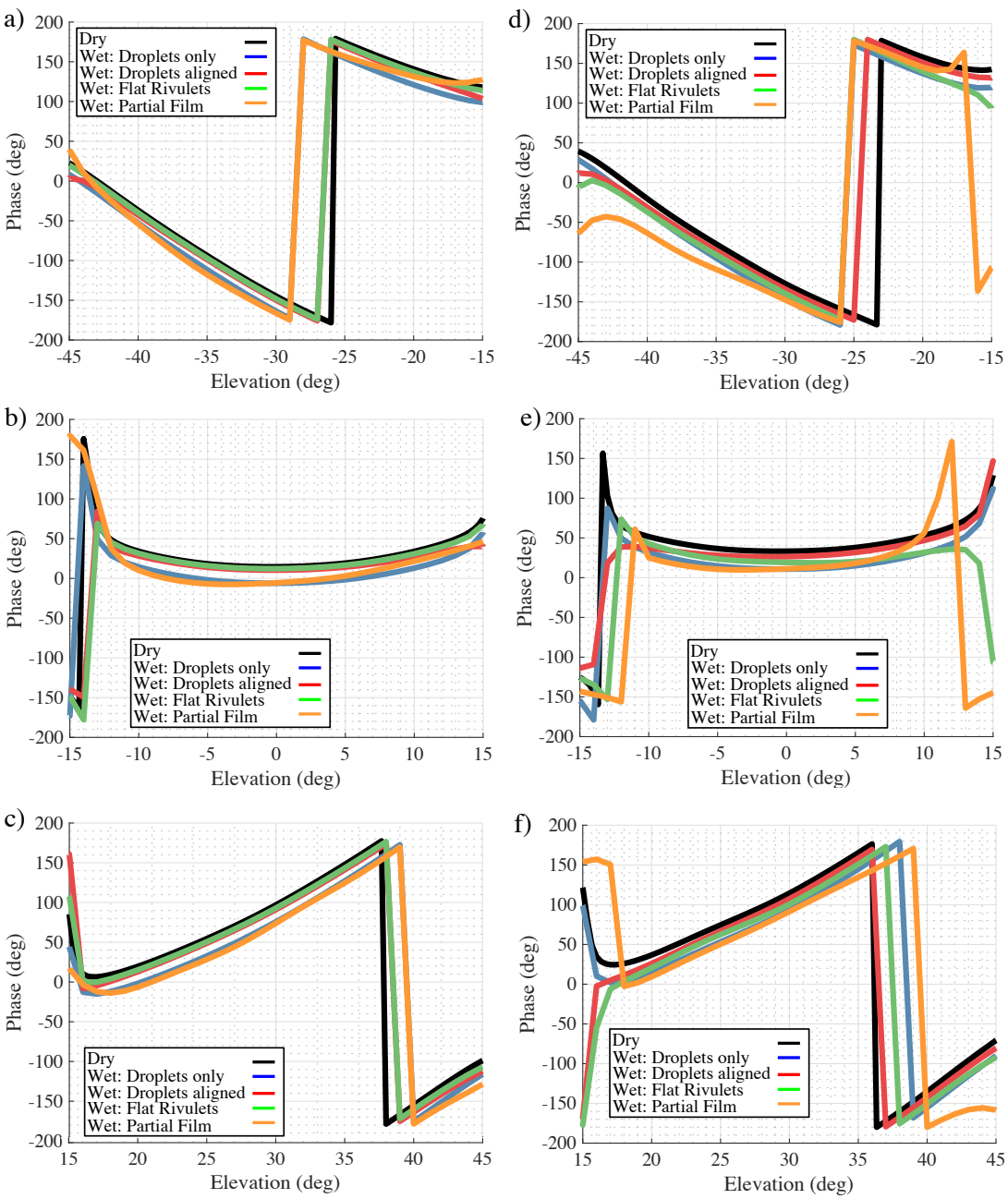

Figure 6.27: The effect of water on the phase of the 8 x 2 active array antenna LRU far-field radiation pattern. Results were based on near-field measurements under various conditions of the radome. a) - c) H-polarization. d) - f) V-polarization. a) and d) Beam steered at -30°. b) and e) Beam at the broadside. c) and f) Beam steered at 30°.

Table 6.1: The attenuation (dB) produced by various water formations located in the near-field region of the antenna. Results based on near-field measurements of the 8 x 2 active array antenna.

Water	θ_s = **-30°**		θ_s = **0°**		θ_s = **30°**	
	H pol.	**V pol.**	**H pol.**	**V pol.**	**H pol.**	**V pol.**
Droplets	0.1	0.1	0.01	0.01	0.09	0.09
Aligned droplets	0.4	0.45	0.41	0.65	0.36	0.25
Rivulets	0.32	2.1	0.23	2.8	0.33	2.1
Partial film	10	5.2	10	6.3	11.5	6

A summary of the results obtained in this research, and a comparison with the available literature is presented in Table 6.2. Performing numerical simulations for film formation at rain rates of 10 - 100 mm h^{-1}, attenuations between 1.47 dB and 3.74 dB were obtained. A similar value of transmission loss (3 dB) was achieved when the radome was characterized in far-field using a single probe. Experiments performed by Effenberg et al. (1986) and Joy and Wilson (1986) found that for film formation on the radome, a transmission loss between 1.5 dB and 3 dB occurred for rain rates in the range of 10 - 50 mm h^{-1}. The attenuation found in the current study agreed with that obtained empirically by Merceret and Ward (2002). Merceret and Ward (2002) measured attenuations from 0.03 dB to 5.6 dB for rain rates ranging from 1 mm h^{-1} to 200 mm h^{-1}. When droplet formation was considered, Merceret and Ward (2002) found transmission losses from a minimum of 0.01 dB to a maximum of 1.95 dB, for rain rates ranging from 1 mm h^{-1} and 200 mm h^{-1}. In this dissertation, attenuation of 0.04 dB was calculated at the rain rate of 10 mm h^{-1} over 5 min of observation time. This result for droplet formation was confirmed by a subsequent experiment in near-field. In conclusion, for droplet formation, a proper comparison between different studies is hard to perform, because

Table 6.2: A comparison between the transmission losses (TL) obtained in this research with the ones found in the literature. In the "Approach" field, for experimental scenarios: FF = far-field, NF = near-field. Data for NF experiments are reported for $\theta_s = 0°$ for the polarization that exhibits the highest attenuation.

Reference	**Approach**	**R (mm h^{-1})**	**Water formation**	θ_i (°)	**TL (dB)**
Wilson (1978)	Exp.	≤ 90	N/A	N/A	≤ 1
Effenberg (1986)	Exp.	15	droplets	60	0.5
		10 - 50	film	60	1.5 - 3
Merceret (2002)	Emp.	1 - 200	droplets	N/A	0.005 - 0.98
			film	N/A	0.015 - 2.8
Present study	Numerical	10 - 100	film	90	0.11 - 0.17
				75	0.2 - 0.37
				60	0.23 - 0.5
		10 (9 min)	droplets	75	0.065
		100 (9 min)		75	0.067
	Exp.l (FF)	102	film	90	3
	Exp. (NF)	8.9	droplets	0	0.05
		N/A	rivulets	90	2.8
		> 80	film	90	11.5

the observation time can be a critical factor at the moment of the attenuation measurement. In addition, when the surface of the radome is hydrophobic, droplets and rivulets present simultaneously (Fig. 4.1). Therefore, it is hard to distinguish the contribution of rivulets from that of the droplets.

6.3 Summary

This chapter presented experiments performed using the novel single-probe technique introduced in Chapter 4. This method was applied to an S-band radome panel of the WSR-88D radar, and to the X-band bullet shape radome of the PX-1000. Results performed for the S-band radome, show that the estimated transmittance agree well with the one calculated numerically, which validates the algorithm presented.

It was shown that the transmittance increases of 2.85 dB from the dry radome to the wet case. Experiments performed using the single-probe method were performed at X-band on the PX-1000 radome. Test in dry conditions show that the reflectance for both the cylindrical and hemispherical part of the radome is about -20 dB. However, locations where radome flaws or non-homogeneities of the honeycomb occur, the reflectance increase to -16 dB. The attenuation of the dry radome is about 0.1 dB as the manufacturer specifications confirm, but locations where air gaps are present show a rise of attenuation to 0.2 dB. The study of the X-band radome was repeated under rain conditions, first considering artificial rain, then using natural rain. In cases of heavy rain (artificial rain), the reflectance increases to -8 dB in locations where film formation occurs, and it stays to lower levels, $<$ -12 dB, in the radome location where droplets and rivulets are present. The computation of differential reflectivity for the artificial rain scenario, shows that different level of reflections (from -10 dB to 3 dB) occur in the H- and V-polarizations. The test performed under natural rain confirms that different water formation contributes to a various level of reflectance and transmittance in the two polarizations. However, because the rain rate was lower than the artificial rain scenario, the level of reflectance and attenuation, as well as their corresponding differential quantities is lower than for the artificial rain case.

Studies on the differential reflectance and transmittance, suggest that dual-polarized weather radar products are affected in cases of wet radome, because the effect of both droplet and film formation is not the same in both polarizations.

Measurements of the radiation pattern of the 8 x 2 array of the phase array antenna performed in the near-field anechoic chamber, show how various water formation contribute to different effect on the radiation pattern, not only in term of attenuation, but also evaluating the rise of the cross-polarization and SLL. Result show that partial film formation produces the worst effects on the radiation pattern compared to the others water formations analyzed. Attenuation of 10 dB was measured in the horizontal plane versus 6 dB measured in the vertical. Results also show that the SLL and cross-polarization increase considerably. The droplet formation case generates only 0.1 dB of attenuation, while aligned droplet can produce a transmission loss up to 0.6 dB. The effect of rivulets was remarked in the vertical polarization, where almost 3 dB of attenuation was measured, while it is only 0.3 dB for the horizontal polarization.

Chapter 7

Epilogue

7.1 Summary

This dissertation provides a detailed overview of radomes, including a method to completely characterize the water distribution and the related effect on the radar signal.

When designing a radome, the core selection is one of the most important aspects to consider. Honeycomb is lower cost than foam, and it allows bending to realized sharp shapes. However, its anisotropic behavior is not suitable for dual-polarized radars, because the different level of reflectance and attenuation introduced on the H- and V-polarizations. Another important aspect to consider is the distance between the radome and the antenna. It was shown that placing the wet radome at a distance of $\lambda/2$ or λ from the antenna, 2.8 dB-attenuation is generated and a higher increase of SLL is obtained with respect to a distance of $\lambda/4$. Therefore, the study suggests that there is an optimum distance to select between the antenna and the radome in wet conditions.

To evaluate the RF performance of a dry multi-layer radome, an analytical model (transmission line) was used and validated with numerical simulations. This study

was performed on radomes operating at S-, C-, and X-bands. Results show acceptable agreement between the two methods demonstrating the validity of the theoretical approach. While good agreement was found in S- and X-bands for the reflectances computed with the analytical and numerical models, a 4-dB difference was noted at C-band between the two techniques. For all the frequency bands analyzed, there is a mismatch between the transmittances computed with the two models. In particular this difference increases with the frequency band analyzed: 0.03 dB at S-band, 0.06 at C-band, and 0.08 dB at X-band. This is attributed to the limitation of the transmission line model.

To evaluate the performance of a wet radome, an analytical method was developed to estimate the amount of water accumulated under various raincoat conditions, temperature of the environment, and frequency of operation. The reflectance, transmittance, and absorption of the water based on the type of water formations considered (film or droplets) was developed. In S-band, an increase of the reflectance of 25 dB from the dry case to the scenario considering a water thickness of 423.4 μm, was measured. This corresponds to an increase of attenuation of 4 dB when a 423.4 μm-film thickness was present. The same analysis was repeated in X-band. Results show that the attenuation can reach 10.5 dB when water is present on the radome. In cases where droplets occur, results show that the reflectance and attenuation is lower than film formation. It was shown that in S-band, for a 10 mm h^{-1}-rain rate, the reflectance increase from -33 dB for the dry case, to -29 dB for droplets accumulated during an observation time of 9 minutes. The transmittance does not show appreciable difference because absorption and reflectance are small

for the droplet formation scenario. At X-band, for a rain rate of 10 mm h^{-1}, the reflectance increases from -29 dB for the observation time of 1 minute, to -25 dB for the same rain rate and 5 minutes of observation time.

To account for real-time measurements of the radome, the single-probe technique was introduced. This solution can be employed in operative radars that employ a reflector dish. Performing experiments in S-band, attenuation of 2.85 dB was measured under heavy rain conditions. At X-band, test in dry conditions show that the reflectance for both the cylindrical and hemispherical part of the radome is about -20 dB. However, locations where radome flaws or non-homogeneities of the honeycomb occur, the reflectance increase to -16 dB. The attenuation of the dry radome is about 0.1 dB as the manufacturer specifications confirm, but locations where air gaps are present show a rise of attenuation to 0.2 dB. The study of the X-band radome was repeated under rain conditions, first considering artificial rain, then using natural rain. In cases of heavy rain (artificial rain), the reflectance increases to -8 dB in locations where film formation occurs, and it stays to lower levels, $<$ -12 dB, in the radome location where droplets and rivulets are present. The computation of differential reflectivity for the artificial rain scenario, shows that different level of reflections (from -10 dB to 3 dB) occur in the H- and V-polarizations.

Measurements of the radiation pattern of the 8 x 2 array of the phase array antenna performed in the near-field anechoic chamber, show how various water formation contribute to different effect on the radiation pattern, not only in term of attenuation, but also evaluating the rise of the cross-polarization and SLL. Result

show that partial film formation produces the worst effects on the radiation pattern compared to the others water formations analyzed. Attenuation of 10 dB was measured for the horizontal polarization versus 6 dB measured for the vertical. Results also show that the SLL and cross-polarization increase considerably. The droplet formation case generates only 0.1 dB of attenuation, while aligned droplet can produce a transmission loss up to 0.6 dB. The effect of rivulets was remarked in the vertical polarization, where almost 3 dB of attenuation was measured, while it is only 0.3 dB in the horizontal polarization.

7.2 Conclusions

By analyzing the results obtained both theoretically and experimentally, important conclusions can be made:

- Radome are fundamental components to protect the radar hardware from the hydrometeors, and therefore they cannot be excluded from a radar system.
- Dual-polarized weather radar performance, which depends on the co- and cross-polarization components is extremely sensitive to the radome presence.
- Dry radomes do not strongly impact dual-polarized weather radar performance, and their effect can be characterized and calibrated.
- When it rains at the radar location, water accumulated on the radome surface can significantly affect the radar signal. The presence of water can occurs in

various forms: film, droplets and rivulets. Each type of formation affects the dual-polarized weather radar in a different way.

- To mitigate the effect of the presence of water on the radome, a raincoat with hydrophobic properties can be used. However, this property does not last for long and it requires continue maintenance.

- When a weather radar operates under rain conditions, there is no mechanism that allows to determine how dual-polarized radar products are affected by the presence of water.

- In this dissertation a novel method to characterize the water formation in real-time during radar operation was presented. This method was implemented and validated by performing experiments both on S- and X-band radomes.

- Results showed that the effect of droplet formation has a stronger impact on the V-polarization than on the H-polarized component. Film formation presents similar effect on both polarizations, however, the attenuation produced is higher than droplets.

- Experiments on a phase array antenna were performed in near-field to evaluate the impact of various water formations on the far-field radiation pattern of the array. Results confirmed what found with the single-probe method, which is that film formation is critical for the antenna performance, while rivulets produce different effect on the two polarizations.

7.3 Future Works

This dissertation provided a completed method to characterize water as a function of the frequency and temperature, taking into account the various water formation. However, these are not all the phenomenas that occur in practical cases. An analytical model to characterize the thicknesses of ice and snow accumulated on the radome is not available yet and it is left for future works. Wind presence, which influences the water accumulated on the surface of the radome, should be accounted for in the model. In addition, to account for scattering generated by droplet particles is also necessary. This is necessary for the case of hydrophobic raincoats. Rivulets were not taken into account in the analytical model, because more experiments should be perform to better understand their conditions of formation and dynamics.

A different aspect which is not considered in the present dissertation, but it is fundamental for weather radars, is to relate the values of reflectance measured with the single-probe method to dual-polarized radar products. This would help to better evaluate the impact of various water formations on the radar measurements. In the present work a single-polarized antenna was used. However, a dual-polarized probe was designed and discussed in the appendix. Such a probe allows to measure both polarization at the same time.

Appendix A

Time Domain Considerations

A.1 Time Domain Gating Analysis

In this appendix it is shown the implementation of the Time Domain Gating (TDG) function employed for the experiment performed with the setup discussed in Chapter 6 (Fig. 6.1).

In the proposed study, TDG is necessary to more accurately measure the reflections produced from the radome without contamination from the reflections generated by the surrounding environment. The dielectric antenna mounted on the rotary motor and oriented at $\theta = 0°$ is schematically shown in Fig. 6.1a. The reflection coefficient measured by the probe in the mentioned position is plotted in Fig. A.1 in the frequency (a) and time (c) domains. The frequency plot shows the antenna bandwidth affected by the reflections coming from the radome panel immediately above it, parts of the setup, and the surrounding external environment. Clearly, it is not possible to separate and establish which reflections are due to the radome panel (useful part) and which ones are due to the rest of the environment (undesired reflections). The time domain plot shows the reflections (peaks) versus the "distance" between the VNA and the target in time. The electromagnetic distance, expressed in time, takes into account the guided propagation of the signal inside the RF cable,

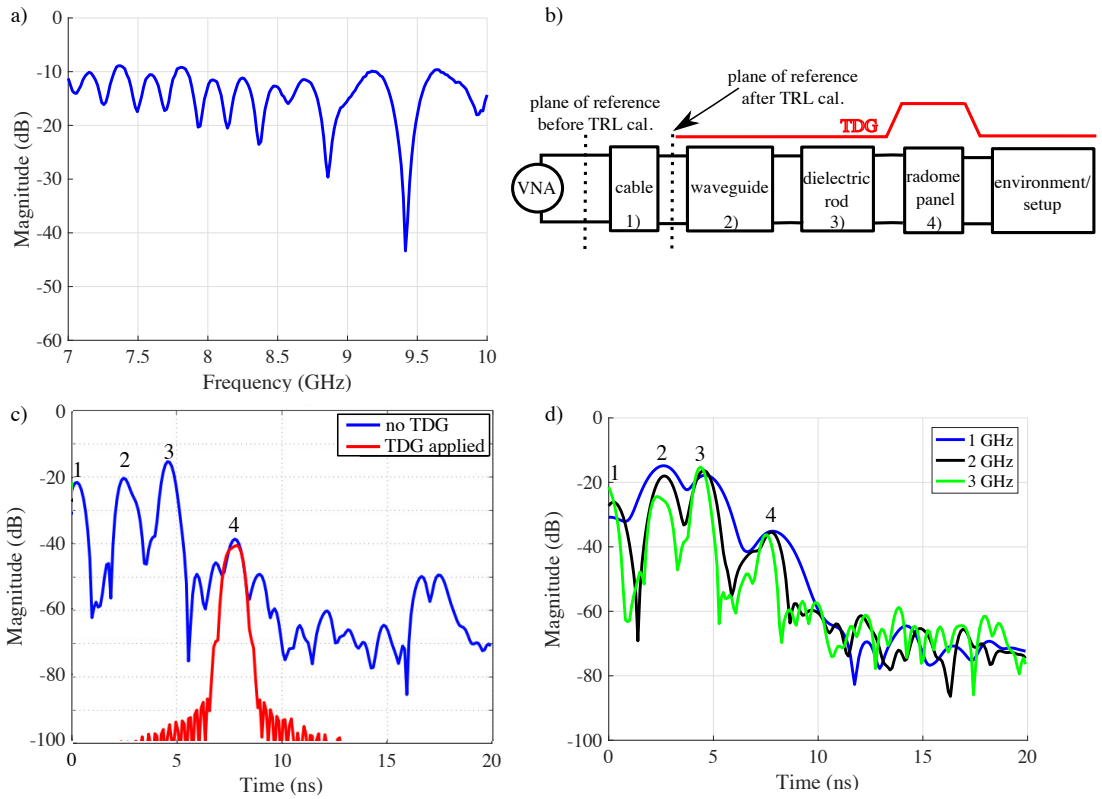

Figure A.1: An example of reflection responses generated by the laboratory setup in the frequency (a) and time (c) domains, obtained with the antenna pointing at $\theta = 0°$. b) A block diagram of the elements causing the reflections (peaks 1 to 4). d) The resolution comparison in the time domain for different widths of frequency bands. In the time domain plots, peaks (1, 2, and 3) are noticeable due to the cable, waveguide, and dielectric rod impedance mismatches.

the waveguide and dielectric rod of the antenna, and the free space propagation. A block diagram of the elements causing the reflections is shown in Fig. A.1b.

Analyzing the time domain response without applying the TDG, represented in Fig. A.1c, it is possible to distinguish the reflections and their related sources, since they are expressed versus the distance in time. The three dominant peaks (1, 2, and 3), located approximately at 0.3 ns, 2.5 ns, and 4.6 ns, are generated by impedance mismatches. The reference plane, which corresponds to 0 ns, is located at the port of the reflectometer, as shown in Fig. A.1b. An open, short, and load

calibration is necessary to remove the reflection (peak) due to the cable. Peak 1 is created by the cable impedance mismatch (no calibration applied). Peak 2 is due to the impedance mismatch introduced by the waveguide. Peak 3 is produced by the waveguide-dielectric rod junction. Peak 4, located at circa 7.8 ns, represents the reflections generated from the radome placed at 12.5 cm above the antenna. Other minor peaks are visible at time >7.8 ns, and are the result of multiple contributions from the environment that are received together. The plot in the time domain was obtained using a frequency span of 3 GHz, since in the frequency plot (Fig. A.1a), a 3 GHz-range (7 - 10 GHz) was used to display the curve. Defining the start and final cut-off times of the filter, equal to 7.5 ns and 8 ns respectively (t_{d1} and t_{d2}), the result is shown in Fig. A.1c. By eliminating all the undesired peaks, a more pure reflection coefficient in the frequency domain (no fluctuations) was obtained. Fig. A.1d presents a comparison of resolutions in the time domain for different frequency spans in the laboratory setup scenario.

A.2 Calibration Analysis

The TDG is an important technique to remove undesired reflections. Such reflections are generated by impedance mismatches and it is fundamental to understand what is the cause of them. Impedance mismatches create loss of the energy of the incident signal because part of it is reflected. Furthermore, impedance discontinuities can obscure the response of the subsequent mismatches, because the energy reflected from the first impedance mismatch never reach the following ones. Such an effect is

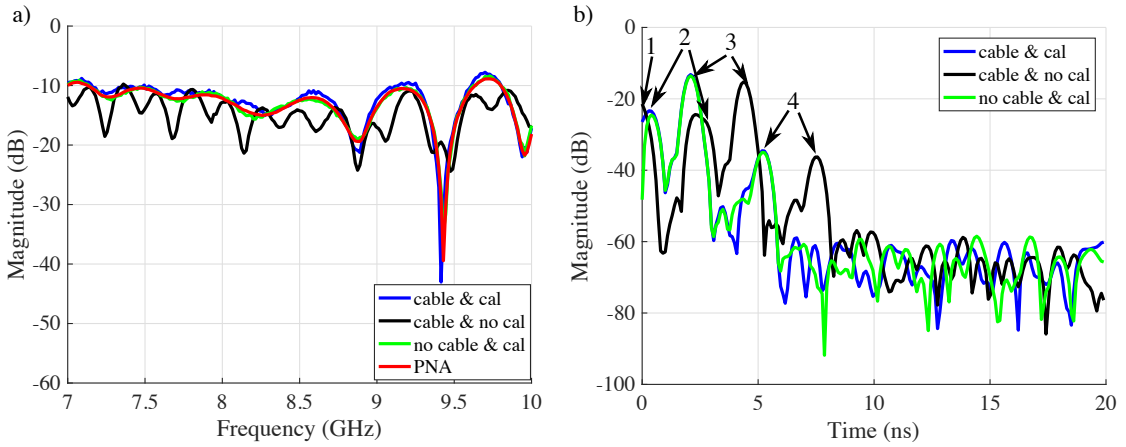

Figure A.2: The open, short, and load calibration effects using a 3 GHz bandwidth in the frequency (a) and time domains (b). Peak 1 corresponds to the cable mismatch, only present in the circle-line curve. Once that the calibration is applied, peak 1 moves to the negative axis of the time. As a consequence of the calibration, peaks 2, 3, and 4 in the circle-line curve are shifted on the left-side of the plot.

called masking (Agilent 2012). The factors that contribute to generate discontinuities in the proposed research is the presence of cable, waveguide, and dielectric rod (previously described). Their effects are presented in Fig. A.2. In the figure, three cases are considered: one using an ordinary RF cable for the antenna-reflectometer connection with the open, short, and load calibration applied (point line); the second using the cable but without applying the open, short, and load calibration (solid line); and the last case without using the cable, but connecting the VNA directly to the antenna and applying the open, short, and load calibration (asterisk line). These three cases are presented in both frequency and in time domain. In the frequency plot the cases were compared with the reflection coefficient of the antenna measured with a Keysight performance network analyzer (PNA-N5225A) for the purpose of reference. A PNA is a very accurate device to perform measurements of linear characteristic of RF components and devices. The oscillations produced by

the RF cable (solid line) are clearly noticeable. When applying the open, short, and load calibration, the plane of reference is shifted to the output of the cable, and then the cable reflection (peak 1) is moved to the negative axis of the time. By removing peak 1, the curve that was obtained by using the cable with open, short, and load calibration applied (point line), matches with the asterisk line, where no cable was used, and it also matches with the reflection coefficient, in frequency domain, of the antenna measured with a Keysight PNA.

The effects due to the impedance mismatches generated from the cable, waveguide, and dielectric rod were discussed and shown in the frequency and time domains. Benefits due to the open, short, and load calibration have also been mentioned.

The TDG width is defined by the start and stop times. For the following experiments they were set to 7.5 ns and 8 ns respectively. Considering that the distance between the probe and the panel was slightly different because of fabrication imperfections of the setup, the TDG width was set in order to capture only the reflections from each single panel, making sure that all radome panels fell inside the TDG width. This was done by performing initial tests with larger time spans for the gating. These experiments produced consistent results so have not been reported here for the sake of brevity.

Appendix B

Software

A LabVIEW interface was created to have a fully automated system during the various experiments discussed in this dissertation. In this appendix a brief explanation about the software used and the related program is given.

The measurement criteria is identical for both of the setups employed. First, the rotary motor rotated the RF probe to an angle with increments (or resolution) dictated by the user (1° for this study). Then a sample was taken. This was repeated until the final designed angle (i.e. 80°) was reached. During the tests, the probe did not move while the sample was taken. The measurements were repeated three times for each scenario and compared with the average.

Appendix C

Two-Layer Dielectric Rod Antenna

An S-band dual-polarized two-layer dielectric rod antenna is presented in this appendix. This probe was developed at the Advanced Radar Research Center to characterize the performance of wet radomes. The antenna consists of two concentric dielectric cylinders and it is fed by paired coaxial probes to achieve dual polarization. The radiation pattern presents narrow beamwidth and relatively high gain. The novelty of this dielectric rod design is that it does not require a launch section, which makes the antenna lighter and more compact than other dielectric rods available in the literature. The key aspects of the proposed antenna are the low cost and ease of fabrication. A prototype of the antenna was fabricated and tested. Measured and simulated performance shows good agreement. It follows a detailed description about the antenna design, fabrication process, and measured performance.

C.1 Antenna Design

This antenna is composed of two concentric dielectric cylinders with different dielectric constants (ϵ_r). The inner solid cylinder, referred to as the core, must exhibit a dielectric constant higher than the material employed for the outer layer. The outer cylinder, referred to as the cladding, is hollow and encloses the core. The inner and

outer diameters of the dielectrics are computed using equations in Chung and Chen (2008). The choice of the materials is not critical; however, if the antenna is required to operate at high temperatures, then it is necessary to select materials that do not have large thermal expansions. This 2-LDR was designed to operate at room temperature. Since the core has a higher ϵ_r than the cladding, most of the energy is confined within it, and only a little bit of the energy is stored in the cladding. The outer layer hosts evanescent modes. This is one of the mechanisms that allows achieving high gain. The second factor that contributes to high gain is the length of the rod. Because dielectric rods are surface wave antennas, they can be represented as end-fire arrays (Zucker and Croswell 2007). The 2-LDR terminates with a taper (peak) to improve the transition between the guided and free-space propagations. The antenna is fed by two pairs of coaxial probes with differential phase to achieve alternate dual-polarization. A circular ground plane with the same diameter as the cladding is located at the bottom of the antenna. In Fig. C.1a, a cross-section of the antenna is shown illustrating the feed section, neck, and radiating peak. In Fig. C.1b, the electric field distribution is shown.

The choice of the dielectric constant determines the dimensions of the inner and outer diameters. By increasing the dielectric constants of the core and cladding, the dimensions of the antenna can be reduced at the expense of the bandwidth (Volakis et al. 2010). It is also desired to use materials with low tangent loss to decrease the dielectric losses. The values of the parameters used to design the proposed 2-LDR (Fig. C.1a and C.1c) are: $D_{out} = 34$ mm, $D_{in} = 26.46$ mm, $H_{probe} = 13.4$ mm, offset $= 9$ mm, $H_{neck} = 265$ mm, and $H_{peak} = 14$ mm.

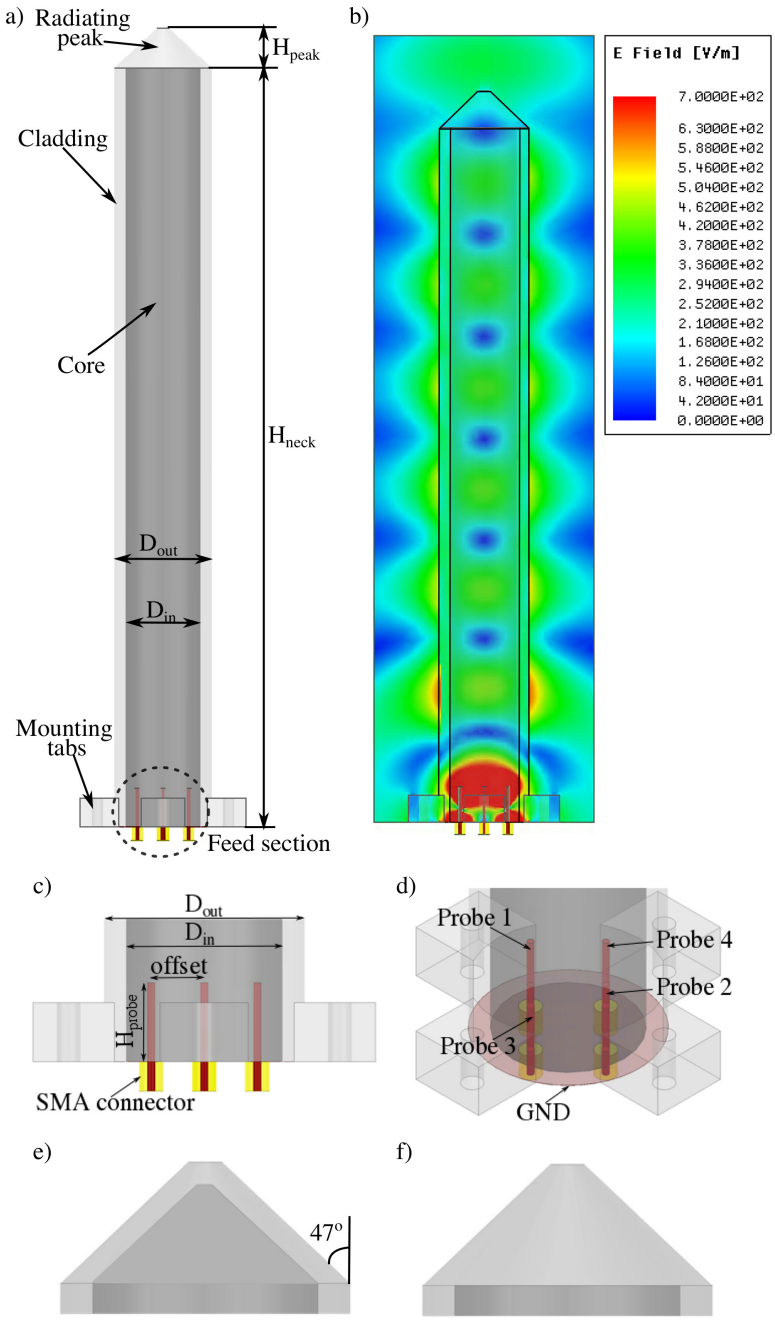

Figure C.1: a) A schematic representation of the 2-LDR antenna. In the figure are shown the feed section, mounting tabs, neck, and radiating peak. Indicated are also the inner and outer diameters of the concentric cylinder. b)The electric field distribution inside the antenna at 3.4 GHz. c) The side view of the feed section showing the coaxial probes to provide dual-polarization. d) As in c), but in an isometric view. It is also shown the ground plane located at the base of the antenna. e) The radiating peaks realized in both core and cladding. f) The radiating peak made only in the cladding

C.1.1 Feed Section

The feed section is composed of two coaxial probes and a ground plane (GND). The GND diameter is equal to the diameter of the cladding. The probes are located inside the core. Dual-polarization is achieved by applying differential phase to the two ports. For example, when port 1 and port 2 are fed, the phase of port 1 is 0° and port 2 is 180°. This allows for linear polarization to be achieved in one plane. To polarize the antenna in the opposite plane, the same procedure is applied to port 3 and port 4. In Figs. C.1c and C.1d, two close-images of the feeding section are provided. Four mounting tabs provide mechanical support of the antenna for practical operation.

C.1.2 Neck

The neck portion is shown in Fig. C.1a and its length is measured from the GND to the base of the radiating peak. The length of the neck impacts the gain and beamwidth, while it has a minor effect on the bandwidth. The principle operation of the neck can be thought as of an end-fire array (Zucker and Croswell 2007). In an end-fire array, by increasing the number of elements the directivity improves. Similarly, if the neck is longer, the gain increases and the beamwidth narrows. The neck should be long enough in order to allow the surface wave inside the core to be completely formed (Zucker and Croswell 2007). However, if its extension is too long, the benefit of having a narrow beamwidth is compensated by having a long

antenna, which can result in unpractical lengths. Therefore, a trade off is necessary between the antenna beamwidth and its length.

C.1.3 Radiating Peak

The radiating peak has the shape of a cone as shown in Fig. C.1a. It extends from the top of the neck, with height optimized by the user. In Zucker and Croswell (2007), it is suggested that the length of the radiating peak should be approximately $0.5\lambda_g$. It improves the matching at the transition dielectric-free space. It is possible to have two matching peaks, one in the inner dielectric and the second one in the outer dielectric, as shown in Fig. C.1e. Alternatively, the radiating peak can be designed only in the outer later and terminating the core without tapering. Tapering both materials slightly improves the matching. The radiating peak is not a critical part of the design and is chosen without the core as shown in Fig. C.1f.

C.1.4 Simulated Performance

Numerical simulations in Ansys HFSS 2017 were performed to design a dual-polarized 2-LDR to operate at 3.4 GHz. A tolerance analysis of the height and offset of the probes are presented. In the following plots, the radiation patterns are shown by using Ludwig 3 definition. Analysis performed for the height and offset of the probe are presented in Fig. C.2 for the return loss. Notice that the resonant frequency slightly shifts as a function of the probe height, while by changing the offset of the probes, the peaks of the resonance changes in magnitude and no shift of the bandwidth is observed. Tolerance analysis for the radiation patterns are presented

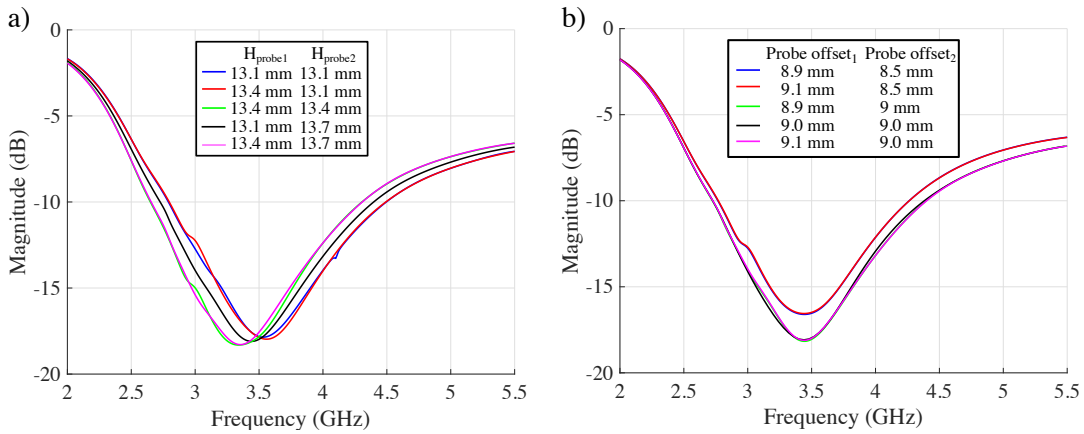

Figure C.2: The tolerance analysis performed on the return loss for variations on the probe height and offset with respect to the center of the cylinder. a) Results for the probe height (H_{probbe}). b) Results for the probe offset.

in Fig. C.3. The plots in Figs. C.3a and C.3b show that the probe height does not impact the co-polarization component, but does affect the cross polarization. Simulations performed on the coaxial probes offset (Fig. C.1c) are shown in Figs. C.3d and C.3e. The probe offset affects the peak of the resonant frequency and the cross polarization, while the co-polarization component is unaltered.

C.2 Fabrication

The main goal during the prototyping of the 2-LDR antenna is to keep the costs of fabrication at minimum. Therefore, 3D-printing is the most promising economic solution. Instead of fabricating the two single parts separately, and then assembling them, an Ultimaker 3 Extended 3D-printer capable of printing two materials simultaneously was used. Each extruder was loaded with a different type of material. In this way, the inner and outer layers of the antenna were simultaneously printed. The materials used are nylon ($\epsilon_r = 3.12$) for the core, and acrylonitrile butadiene

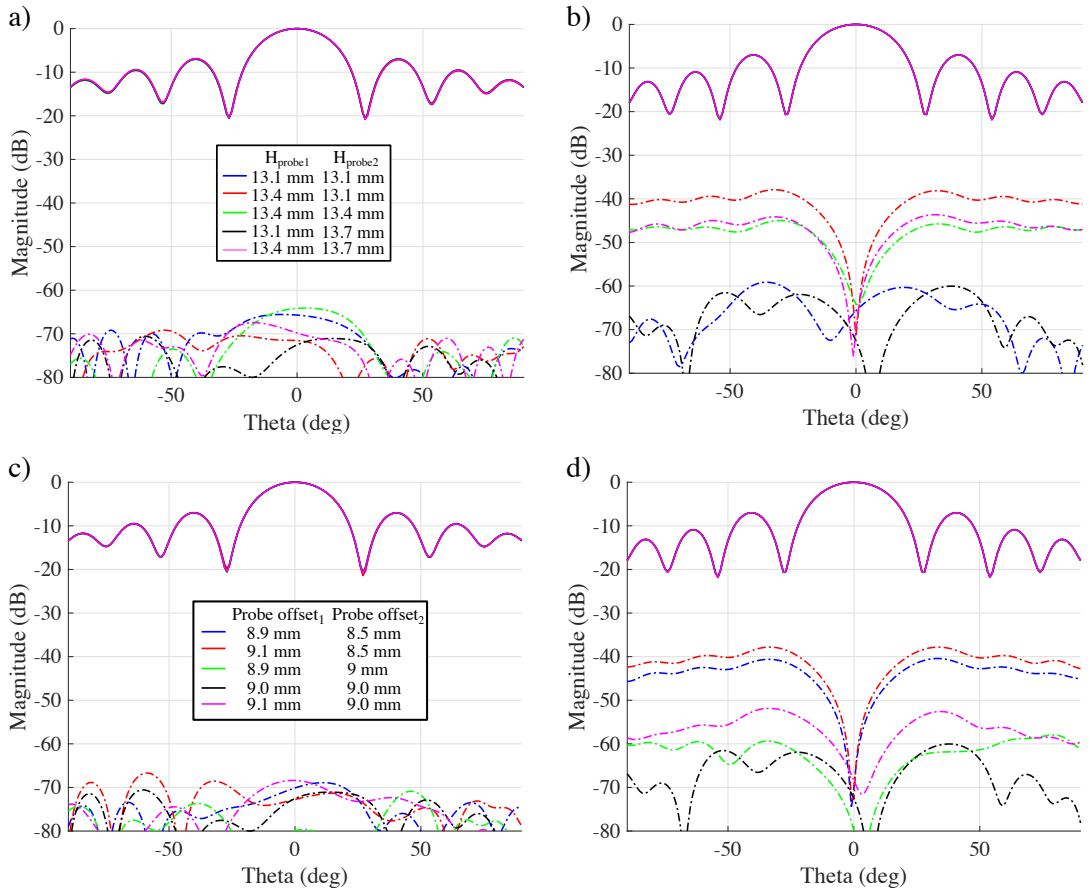

Figure C.3: The tolerance analysis performed on the radiation pattern at 3.4 GHz for variations on the probe height and offset with respect to the center of the cylinder. a) and b) Results for the probe height (H_{probe}) for the $\phi = 0°$ plane and $\phi = 90°$ plane, respectively. c) and d) Results for the probe offset for the $\phi = 0°$ plane and $\phi = 90°$ plane, respectively.

styrene (ABS, $\epsilon_r = 2.78$) for the cladding. These values of the dielectric constants were measured with an infill of 100 %. The estimated cost of the antenna is roughly $ 40 and the total weight is 300 gr. Fig. C.4a is a photo of the proposed 2-LDR antenna.

A copper ground plane was adhered to the dielectric by using double-sided adhesive tape. The coaxial probes employed are standard SMA probes with teflon removed in order to be inserted inside the core. The probes are shown in Fig. C.4b

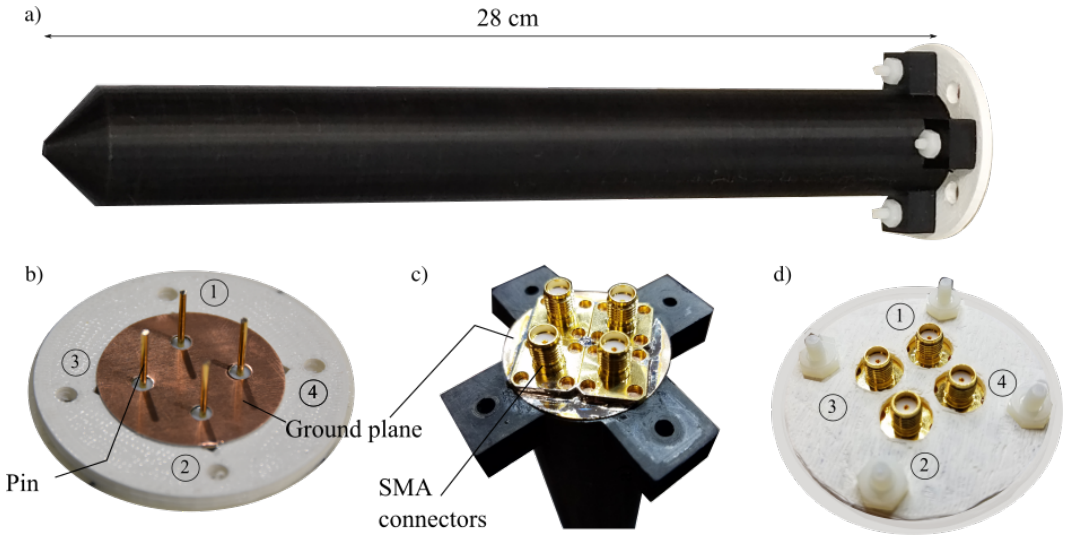

Figure C.4: Photograph of the 3D-printed 2-LDR. a) Side view. b) Top view of the feed section (before assembling it in the antenna) including the ground plane, the probes, and the 3D-printed mechanical fixture. c) Bottom view of the feeding section that was assembled in the dielectric. d) Bottom view of the mechanical support affixed to the rest of the antenna.

before being inserted in the dielectric, and in Fig. C.4c after being assembled to the rest of the antenna. The drilling and height adjustment of the probes was performed manually, so some imprecision occurred during the fabrication. To assure mechanical strength of the connectors to the external RF cable, a support was designed and 3D-printed as shown in Fig. C.4d.

C.3 Measured Performance

The reflection coefficient of the 2-LDR measured at each port and compared with numerical simulations is presented in Fig. C.5. The reflection coefficient at each port agrees well with the numerical simulation and only a small shift in the bandwidth is noticed.

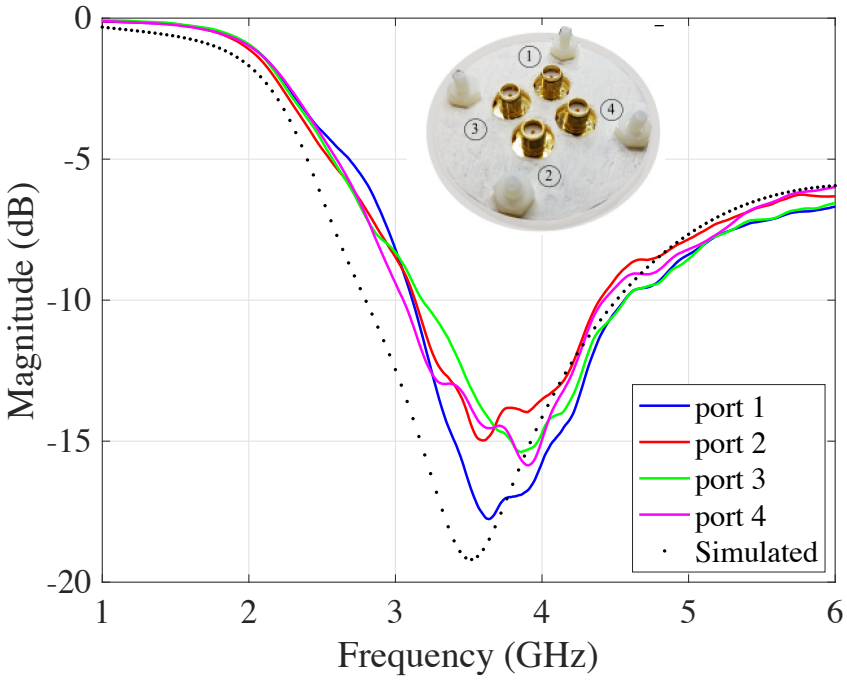

Figure C.5: The reflection coefficient of the 2-LDR antenna measured at each port and compared with numerical results.

A comparison between the simulated and measured radiation pattern, using the Ludwig 3 definition, are shown in Fig. C.6a ($\phi = 0°$) and C.6b ($\phi = 90°$), where port 1 and port 2 are fed, and in Fig. C.6c ($\phi = 0°$) and C.6d ($\phi = 90°$) where port 3 and port 4 are fed. Simulated and measured curves shows good agreement. The higher level of cross polarization is due to limitations during the far-field measurement. The probe used to perform the measurement only has -35 dB-cross-polarization. Also, perfect alignment between the measurement probe and AUT is hard to achieve during far-field measurements. These factors limit the capability of detecting low values of cross polarization. The measured antenna beamwidth is 29°, the sidelobe level is 8 dB and 9 dB in the $\phi = 0°$ and $\phi = 90°$ planes, and the gain is 10 dB at 3.4 GHz.

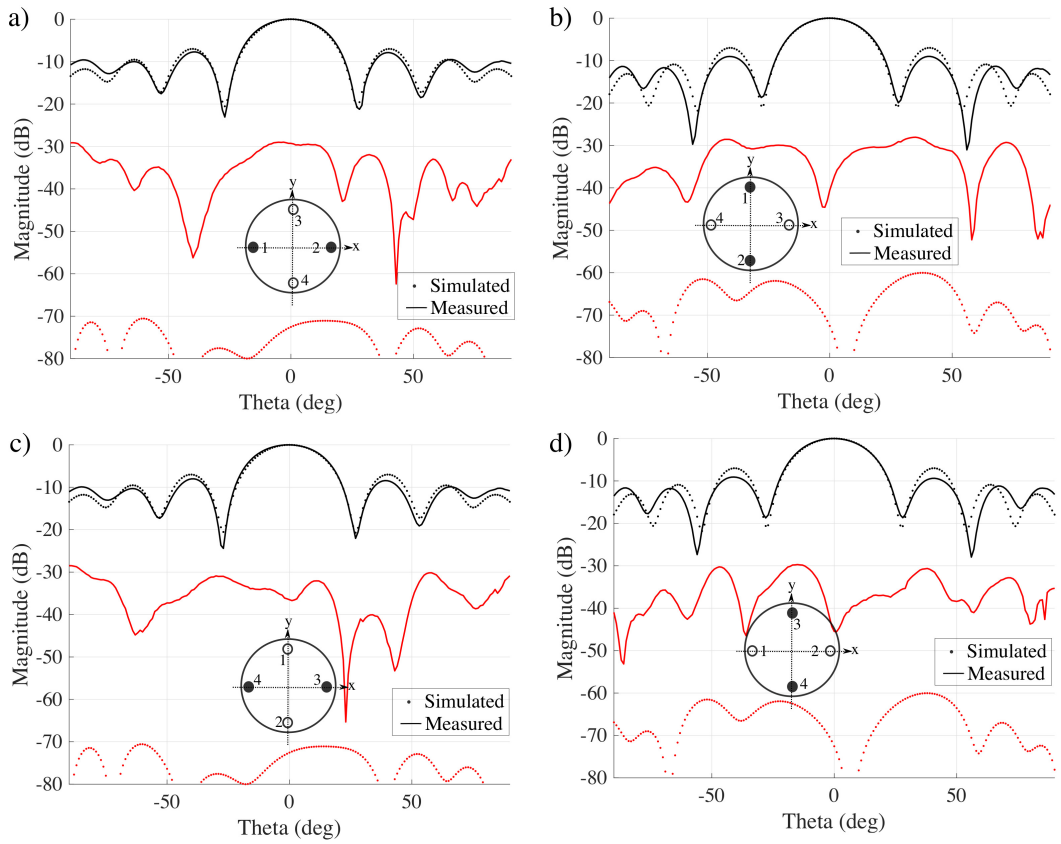

Figure C.6: The radiation pattern was measured in a far-field chamber and is shown at 3.4 GHz. In dashed lines is also indicated the simulated performance for purpose of comparison. a) and b) The radiation pattern obtained by exciting with differential phase ports 1 and 2 on the $\phi = 0°$ and $\phi = 90°$ planes. c) and d) The radiation pattern obtained by exciting with differential phase ports 3 and 4 on the $\phi = 0°$ and $\phi = 90°$ planes.

Bibliography

Achammer, T. and Denoth, A. (1994), 'Snow dielectric properties: from DC to microwave X-band', **19**, 92–96.

Agilent (2012), Time domain analysis using a network analyzer, Application note, Agilent Technologies.

Anderson, I. (1975), 'Measurements of 20 GHz transmission through a radome in rain', *IEEE Trans. Antennas Propag.* **23**, 619–622.

Antonets, I. V., Kotov, L. N., Shavrov, V. G. and Shcheglov, V. I. (2008), 'Reflection, transmission, and absorption coefficients calculated for the oblique incidence of an electromagnetic wave on a plate', *Journal of Communications Technology and Electronics* **53**, 363–376.

Archambeault, B., Connor, S. and Diepenbrock, J. C. (2006), Time domain gating of frequency domain S-parameter data to remove connector end effects for PCB and cable applications, *in* '2006 IEEE International Symposium on Electromagnetic Compatibility', pp. 199–202.

Atlas, D. and Ulbrich, C. W. (1977), 'Path- and area-integrated rainfall measurement by microwave attenuation in the 1–3 cm band', *Journal of Applied Meteorology* **16**(12), 1322–1331.

Balanis, C. A. (2012), *Advanced Engineering Electromagnetics*, Wiley.

Bechini, R., Chandrasekar, V., Cremonini, R. and Lim, S. (2010), Radome attenuation at X-band radar operations, *in* 'Proc. Sixth European Conf. on Radar in Meteorology and Hydrology', ERAD 2010, p. 15.1.

Blevis, B. (1965), 'Losses due to rain on radomes and antenna reflecting surfaces', *IEEE Trans. Antennas Propag.* **13**, 175–176.

Bohren, C. F. and Huffman, D. R. (1983), *Absorption and Scattering of Light by Small Particles*, J. Wiley and Sons, Inc.

Burks, D. G. (2007), *Antenna Engineering Handbook*, McGraw-Hill, chapter 53.

Burrell, G. A. and Jamieson, A. R. (1973), 'Antenna radiation pattern measurement using time domain-to-frequency transformation (TFT) techniques', *IEEE Transactions on Antennas and Propagation* **21**, 702–704.

Chang, K.-C. (1985), 'System performance in rain in a radome-enclosed environment', *1985 IEEE Military Communications Conference: MILCOM '85* **1**, 293–299.

Cheong, B. L., Kelley, R., Palmer, R. D., Zhang, Y., Yeary, M. and Yu, T. (2013), 'PX-1000: A solid-state polarimetric X-band weather radar and time–frequency multiplexed waveform for blind range mitigation', *IEEE Transactions on Instrumentation and Measurement* **62**(11), 3064–3072.

Chung, J. and Chen, C. (2008), 'Two-layer dielectric rod antenna', *IEEE Transactions on Antennas and Propagation* **56**(6), 1541–1547.

Cohen, A. and Smolski, A. (1966), 'The effect of rain on satellite coomunications earth terminal rigid radomes', *Microwave J.* .

Cole, K. S. and Cole, R. H. (1941), 'Dispersion and absorption in dielectrics I. Alternating current characteristics', *The Journal of Chemical Physics.* **9**, 341–351.

Crane, R. K. (2002), 'Analysis of the effects of water on the ACTS propagation terminal antenna', *IEEE Transactions on Antennas and Propagation* **50**, 954–965.

Díaz, J. D., Salazar, J. L., Ortiz, J. A., Fulton, C., Aboserwal, N., Kelley, R. and Palmer, R. (2016), A dual-polarized cross-stacked patch antenna with wide-angle and low cross-polarization for fully digital multifunction phased array radars, *in* '2016 IEEE International Symposium on Phased Array Systems and Technology (PAST)', pp. 1–4.

Díaz, J., Salazar, J. L., Mancini, A. and Colom, J. G. (2014), Radome design and experimental characterization of scattering and propagation properties for atmospheric radar applications, Amer. Meteor. Soc., pp. 819–823.

Dunsmore, J. (2008), Gating effects in time domain transforms, *in* 'Microwave Measurement Symposium, 2008 72nd ARFTG', IEEE, pp. 1–8.

Effenberg, J. A., Strickland, R. R. and Joy, E. B. (1986), 'The effects of rain on a radome's performance', *Microwave Jorunal* .

Fenn, A. J. (1997), Measurements of wet radome transmission loss and depolarization effects in simulated rain at 20 GHz, *in* '10th International Conference on Antennas and Propagation', IEEE.

Fordham, J. (2010), Use of time domain gating in spherical near-field measurements, *in* '2010 14th International Symposium on Antenna Technology and Applied Electromagnetics and the American Electromagnetics Conference (ANTEM-AMEREM)', IEEE, pp. 1–4.

Frasier, S. J., Kabeche, F., Ventura, J. F. I., Al-Sakka, H., Tabary, P., Beck, J. and Bousquet, O. (2013), 'In-place estimation of wet radome attenuation at X band', *J. Atmos. Oceanic Technol.* **30**, 917–928.

Frech, M. (2009), The effect of a wet radome on dualpol data quality, *in* '34th Conf. on Radar Meteorology'.

Frech, M., Lange, B., Mammen, T., Seltmann, J., Morehead, C. and Rowan, J. (2013), 'Influence of a radome on antenna performance', *Atmos. Oceanic Technol.* **30**, 313–32.

Fulton, C., Salazar, J. L., Zhang, Y., Zhang, G., Kelly, R., Meier, J., McCord, M., Schmidt, D., Byrd, A. D., Bhowmik, L. M., Karimkashi, S., Zrnic, D. S., Doviak, R. J., Zahrai, A., Yeary, M. and Palmer, R. D. (2017), 'Cylindrical polarimetric phased array radar: Beamforming and calibration for weather applications', *IEEE Transactions on Geoscience and Remote Sensing* **55**(5), 2827–2841.

Fulton, C., Salazar, J., Zrnic, D., Mirkovic, D., Ivic, I. and Doviak, D. (2018), Polarimetrie phased array calibration for large-scale multi-mission radar applications, *in* '2018 IEEE Radar Conference (RadarConf18)', pp. 1272–1277.

Ghodgaonkar, D. K., Varadan, V. V. and Varadan, V. K. (1989), 'A free-space method for measurement of dielectric constants and loss tangents at microwave frequencies', *IEEE Transactions on Instruments and Measurements* **38**, 789–793.

Gibble, D. (1964), Effect of rain on transmission performance of a satellite communication system, *in* 'IEEE International Convention Record, Part VI', IEEE, p. 52.

Golbon-Haghighi, M.-H., Saeidi-Manesh, H., Zhang, G. and Xhang, Y. (2018), 'Pattern synthesis for the cylindrical polarimetric phased array radar (CPPAR)', *Progress In Electromagnetics Research M* **66**, 87–98.

Golbon-Haghighi, M.-H., Zhang, G., Li, Y. and Doviak, R. J. (2016), 'Detection of ground clutter from weather radar using a dual-polarization and dual-scan method', *Atmosphere* **7**(6).

Golbon-Haghighi, M., Zhang, G. and Doviak, R. J. (2018), 'Ground clutter detection for weather radar using phase fluctuation index', *IEEE Transactions on Geoscience and Remote Sensing* pp. 1–7.

Gorgucci, E., Bechini, R., Baldini, L., Cremonini, R. and Chandrasekar, V. (2012), 'The influence of antenna radome on weather radar calibration and its real-time assessment', *J. Atmos. Oceanic Technol.* **30**, 676–689.

Hendrix, C. E., McNally, J. E. and Monzingo, R. A. (1989), 'Depolarization and attenuation effects of radomes at 20 GHz', *IEEE Trans. Antennas Propag.* **37**, 320–328.

Irazoqui, R. and Fulton, C. (2018), Spatial interference mitigation nulling the embedded element pattern, *in* '2018 IEEE/MTT-S International Microwave Symposium - IMS', pp. 620–623.

Joy, E. B. and Wilson, R. E. (1986), 'The electromagnetic effects of water on the surface of a radome', *Proceedings of the 18th symposium on electromagnetic windows* .

Kobayashi, S., Mittra, R. and Lampe, R. (1982), 'Dielectric tapered rod antennas for millimeter-wave applications', *IEEE Trans. Antennas Propag.* **30**, 54–58.

Kurri, M. and Huuskonen, A. (2008), 'Measurements of transmission loss of a radome at different rain intensities', *J. Atmos. Oceanic Technol.* **25**, 1590–1599.

Mancini, A., Lebrón, R. M. and Salazar, J. L. (2018), 'The impact of a wet S-band radome on dual-polarized phased-array radar system performance', *IEEE Transactions on Antennas and Propagation* pp. 1–1.

Mancini, A., Salazar, J. L., Lebrón, R. M. and Cheong, B. L. (2017), A novel technique to characterize the effect of rain over a radome for radar applications, *in* 'Radar Conference', IEEE.

Mancini, A., Salazar, J. L., Lebrón, R. M. and Cheong, B. L. (2018*a*), 'A novel instrument for real-time measurement of attenuation of weather radar radome including its outer surface. Part I: The concept', *Journal of Atmospheric and Oceanic Technology* **35**, 953–973.

Mancini, A., Salazar, J. L., Lebrón, R. M. and Cheong, B. L. (2018*b*), 'A novel instrument for real-time measurement of attenuation of weather radar radome including its outer surface. Part II: Applications', *Journal of Atmospheric and Oceanic Technology* **35**, 975–991.

Manz, A., Handwerker, L., Löffler-Mang, M., Hannesen, R. and Gysi, H. (1999), Radome influence on weather radar systems principles and calibration issues, *in* '29th Int. Conf. on Radar Meteorology', Amer. Meteor. Soc, pp. 918–921.

Matsuoka, T., Fujita, S. and Mae, S. (1996), 'Effect of temperature on dielectric properties of ice in the range 5-39 GHz', *Journal of Applied Physics* **80**(10), 5884–5890.

Merceret, F. J. and Ward, J. G. (2002), Attenuation of weather radar signals due to wetting of the radome by rainwater or inclomplete filling of the beam volume, Technical report, NASA.

Mirkovic, D. and Zrnic, D. S. (2018*a*), Polarimetrie calibration using the computational electromagnetics approach, *in* '2018 IEEE Radar Conference (RadarConf18)', pp. 1348–1352.

Mirkovic, D. and Zrnic, D. S. (2018*b*), Polarimetrie weather radar calibration by computational electromagnetics, *in* '2018 International Applied Computational Electromagnetics Society Symposium (ACES)', pp. 1–2.

Mirmozafari, M., Saeedi, S., Saeidi-Manesh, H., Zhang, G. and Sigmarsson, H. H. (2018), 'Direct 3-D printing of non-planar linear dipole phased array antennas', *IEEE Antennas and Wireless Propagation Letters* pp. 1–1.

Mirmozafari, M., Saeidi-Manesh, H. and Zhang, G. (2018), 'Highly isolated crossed dipole antenna with matched copolar beams', *Electronics letters* **54**(8), 470–472.

Mueller, G. E. and Tyrrell, W. A. (1947), 'Polyrod antennas', *Alcatel-Lucent Journal* **26**, 837–851.

Nilsson, M. A. and Rothstein, J. P. (2012), 'Using sharp transitions in contact angle hysteresis to move, deflect, and sort droplets on a superhydrophobic surface', *Physics of Fluids* **24**(6), 062001.

Pazmany, A. L., Mead, J. B., Bluestein, H. B., Snyder, J. C. and Houser, J. B. (2013), 'A mobile rapid-scanning X-band polarimetric (RaXPol) doppler radar system', *Journal of Atmospheric and Oceanic Technology* **30**(7), 1398–1413.

Perry, R. H. (1997), *Perry's Chemical Engineers' Handbook*, McGraw-Hill.

Pozar, D. M. (2012), *Microwave Engineering*, J. Wiley and Sons, Inc.

Ruze, J. (1965), 'More on wet radomes', *IEEE Trans. Antennas Propag.* **13**, 823–824.

Saeidi-Manesh, H., Mirmozafari, M. and Zhang, G. (2017), 'Low cross-polarisation high-isolation frequency scanning aperture coupled microstrip patch antenna array with matched dual-polarisation radiation patterns', *Electronics Letters* **53**(14), 901–902.

Saeidi-Manesh, H., Saeedi, S., Mirmozafari, M., Zhang, G. and Sigmarsson, H. H. (2018), 'Design and fabrication of orthogonal mode transducer using 3D printing technology', *IEEE Antennas and Wireless Propagation Letters* pp. 1–1.

Saeidi-Manesh, H. and Zhang, G. (2018), 'High-isolation, low cross-polarization, dual- polarization, hybrid feed microstrip patch array antenna for MPAR application', *IEEE Transactions on Antennas and Propagation* **66**(5), 2326–2332.

Salazar, J. L., Chandrasekar, V., J. M. Trabal, P. S., Medina, R., Knapp, E. and McLaughlin, D. J. (2014), 'A drop size distribution (DSD)-based model for evaluating the performance of wet radome for dual-polarized radars', *J. Atmos. Oceanic Technol.* **31**, 2409–2430.

Schneebeli, M., Sakuragi, J., Biscaro, T., Angelis, C. F., da Costa, I. C., Morales, C., Baldini, L. and Machado, L. A. T. (2012), 'Polarimetric X-band weather radar measurements in the tropics: radome and rain attenuation correction', *Atmos. Meas. Tech.* **5**, 2183–2199.

Sihvola, A. (2000), 'Mixing rules with complex dielectric coefficients', *Subsurface Sensing Technologies and Applications* **1**(4), 393–415.

Steiner, M. and Smith, J. A. (2000), 'Reflectivity, rain rate, and kinetic energy flux relationships based on raindrop spectra', *Journal of Applied Meteorology* **39**(11), 1923–1940.

Stroobandt, S. Y. (1997), An X-band high-gain dielectric rod antenna, Technical report, Katholieke Universiteit Leuven.

Studd, A. C. (1991), Towards a better dielectric rod antenna, *in* '7th International Conference on Antennas and Propagation, 1991', IET, pp. 117–120.

Thompson, R. and Illingworth, A. (2012), Correcting attenuation in operational radars from both heavy rain and the radome using the observed microwave emission, *in* '7th European Conference on Radar in Meteorology and Hydrology', ERAD.

USGS (2018), 'Water science school'.
URL: *https://water.usgs.gov/edu/watercyclesublimation.html*

Vitale, J. A. (1985), *Microwave Scanning Antennas*, Vol. I, Peninsula Publishing, chapter 5.

Volakis, J. L., Chen, C. C. and Fujimoto, K. (2010), *Small antennas: miniaturization techniques & applications*, McGraw-Hill.

Wallace, J. M. and Hobbs, P. V. (1977), *Atmospheric Science an Introductory Survey*, Academic Press.

Walton (1970), *Radome Engineering Handbook: Design and Principles*, Marcel Dekker, Inc.

Wang, Y. and Chandrasekar, V. (2006), 'Polarization isolation requirements for linear dual-polarization weather radar in simultaneous transmission mode of operation', *IEEE Transactions on Geoscience and Remote Sensing* **44**, 2019–2028.

Watson, R. B. and Horton, C. W. (1948), 'The radiation pattern of dielectric rods–experiment and theory', *Journal of Applied Physics* **19**, 661–670.

Wayapattanakorn, C. and Parini, C. G. (1993), Theoretical and experimental investigations of using time domain gating in antenna pattern measurements, *in* '8th International Conference on Antennas and Propagation', IEEE, pp. 327–330.

Wilson, J. W. (1978), Observations of radome transmission losses at 5 cm wavelength, *in* '18th Conference on Radar Meteorology of the American Meteorological Society'.

Zaho, M., Shea, J. D., Hagness, S. C. and van der Weide, D. W. (2006), 'Calibrated free-space microwave measurements with an ultrawideband reflectometer-antenna system', *IEEE Microwave and Wireless Components Letters* **16**, 675–677.

Zhang, G. (2017), *Weather Radar Polarimetry*, Taylor and Francis Group, LLC.

Zhang, G., Vivekanandan, J. and Brandes, E. (2001), 'A method for estimating rain rate and drop size distribution from polarimetric radar measurements', *IEEE Transactions on Geoscience and Remote Sensing* **39**(4), 830–841.

Zrnic, D. S. and Doviak, R. J. (2005), System requirements for phased array weather radar, Technical report, NOAA/NSSL.

Zucker, F. J. and Croswell, W. F. (2007), Surface-wave antennas, *in* J. L. Volakis, ed., 'Antenna Engineering Handbook', McGraw-Hill.